ELECTRODEPOSITION OF THIN FILM SHAPE MEMORY ALLOYS

DAVID GORDON PAGE

DOCTOR OF PHILOSOPHY DEGREE

Department of Chemical & Process Engineering
University of Newcastle Upon Tyne

JUNE 2001

Abstract

There is considerable potential for the use of thin film shape memory alloys in the field of microtechnology due to their high power to volume ratio. The main obstacles for fabrication arise mainly due to the narrow regime over which shape memory behaviour is observed and the paucity of process techniques. Shape memory transition in brass only occurs in the alloy composition range 38.5 - 41.6 wt % % zinc.

This study used a pyrophosphate electrolyte containing $Cu_2P_2O_7$, $Zn_2P_2O_7$ salts and an excess of $K_4P_2O_7$ and KNO_3, for brass deposition as a replacement for cyanide electrolytes because it is non-toxic and non-corrosive. A rotating disc electrode was employed to systematically examine polarisation data and a rotating cylinder electrode was employed to produce thin brass films and deduce the current efficiencies of copper, zinc and brass deposition with respect to deposition potential. Thin films were plated between 5 - 30μm, they all displayed a smooth, uniform homogenous deposit with no precipitates or oxide inclusions. The current efficiencies were found to be < 45% for copper, < 15% for zinc and between 10 - 30% for brass.

The microstructural characterisation of the Cu-Zn thin alloys was undertaken by X-ray diffraction (XRD), scanning electron microscopy (SEM) and energy dispersive X-ray fluorescence (EDAX), transmission electron microscopy (TEM) and differential scanning calorimetry (DSC). XRD showed all the electrodeposited Cu-Zn alloys to have same phase composition as those predicted by the equilibrium phase diagram for Cu-Zn. This confirmed the existence of the parent β-phase within the shape memory composition range, which undergoes the martensitic transformation. TEM showed these foils to be composed of a matrix of α, β and martensite nano sized grains (< 40nm) co-existing with a sparse distribution of larger grains (200-300nm). The larger grains were always martensite in nature, recognisable by their twinning

planes. Differential scanning calorimetry analysis shows evidence of a martensitic transformation change for the thin brass films.

Acknowledgements

Over the duration of my PhD, I have met many people who have helped me mostly by way of guidance, others with wit. I have this opportunity to thank some of them.

Firstly I am indebted to my supervisor, Sudipta Roy, for her constant enthusiasm, knowledge, support, always making herself available and finally her great patience. Extra thanks is also due for organising trips to the EPFL Federal Institute in Lausanne Switzerland, to use their valuable equipment we do not possess at Newcastle.

I am also much the wiser having spent a lot of my time in the company of Todd Green with his calm, no fuss approach to problems.

My time at Newcastle has also been made more enjoyable working with Rob & Paul who always offered a joke and a drop whatever there're doing attitude to give me and others a hand.

Thank you, and thanks to everyone else I've missed, sorry but you know who you are.

"There must be a beginning of any great matter, but the continuing unto the end until it be thoroughly finished yields the true glory"

Sir Francis Drake (1540 -96)

Contents

Chapter 1 - Background

1.0 Background 2
1.1 Shape memory alloys 3
1.2 Phases and phase transformation 3
Martensite 3
Austenite 4
Martensitic transformation 5
1.3 Transformation mechanism 6
(a) Bain strain 6
(b) Lattice-invariant shear 7
1.4 Transition temperature range 10
1.6 CuZn shape memory alloy 12
1.7 The CuZn equilibrium phase diagram 13
1.8 Shape memory region in brass 17
1.9 Ternary alloys 20

References 21

Chapter 2 - Processing Methods

2.0 Processing methods 23
2.1 Physical vapour deposition 24
2.2 Electrodeposition 27
Electrode potentials 28
Electrode reactions during electrodeposition 29
Electron processes 30
Mass transport 34
Steady state I-E curves 35
Hydrogen evolution & influence on metal deposition 36
Deposition process 38
Co-deposition of metals 39
Current investigations 41

References 42

Chapter 3 - Plating Bath

3.0 Brass plating baths 44
3.1 The pyrophosphate bath 45

References 48

Chapter 4 - Experimental

4.0 Electrolyte 51
4.1 Electrodeposition 52
4.1.1 Apparatus 52
4.1.2 Procedure 52
4.2 Electrochemical studies 54
4.2.1 Polarisation measurements 54
4.2.2 Monitoring pH change at the electrode surface 55
4.2.3 Current efficiency measurements 56
4.2.4 Nitrate reduction 57
4.2.5 Modelling of pyrophosphate speciation 58
4.3 Material characterisation 58
4.3.1 X-ray diffraction 58
4.3.2 Scanning electron microscopy & EDAX 59
4.3.3 Transmission electron microscopy 60
4.3.4 Differential scanning calorimetry 62
4.3.5 Heat treatments 62

References 64

Chapter 5 - Polarisation Data

5.0 Polarisation measurements 66
5.1 Background current 68
5.2 Current efficiency 69
Determination of current efficiencies 69
Omission of nitrate 70
Nitrate loss from a pyrophosphate plating solution 71
5.3 Partial currents 74
Copper & zinc deposition 74
Brass deposition 75
5.4 Rotation Speed effects 76
Polarisation data 76

$CuZn_5$ 77
pH change at electrode surface 78
Modelling of pyrophosphate speciation 80

Chapter 6 - Material Characterisation

6.0 X-ray diffraction..... 84
6.1 Scanning electron microscopy & EDAX..... 97
6.2 Transmission electron microscopy 99
6.3 Differential scanning calorimetry 102

Chapter 7 - Discussion

7.0 Polarisation measurements 105
7.1 Current efficiency 106
7.2 Partial currents 107
7.3 $CuZn_5$ 109
7.4 X-ray diffraction 111
7.5 SEM, EDAX & TEM 114
7.6 DSC 114

References 116

Chapter 8 - Conclusions 117

Appendix A 120

Appendix B 123

Figures

Chapter 1 - Background

Figure 1.1	"The Bain strain"	6
Figure 1.2	"Lattice-invariant shear"	7
Figure 1.3	"Twin boundary"	8
Figure 1.4	"Detwinning"	9
Figure 1.5	"Martensitic transformation cycle"	10
Figure 1.6	"The Cu-Zn equilibrium phase diagram"	13
Figure 1.7	"Calculation of phase ratio"	16
Figure 1.8	"Parent phase structure"	18
Figure 1.9	"Martensite stacking planes"	18
Figure 1.10	"β' martensite - M9R"	19

Chapter 2 - Processing Methods

Figure 2.1	"A simple parallel plate sputtering system"	25
Figure 2.2	"The three electrode cell"	27
Figure 2.3	"A typical I-E profile for an electron transfer reaction"	35
Figure 2.4	"Deposition mechanisms"	39

Chapter 4 - Experimental

Figure 4.1	"Rotating cylinder electrode"	53
Figure 4.2	"Rotating gold disc electrode"	54
Figure 4.3	"Electrode surface pH measurement"	55

Chapter 5 - Polarisation Data

Figure 5.1	"Polarisation profiles for Cu & Zn reduction"	66
Figure 5.2	"Polarisation profile for brass reduction"	67
Figure 5.3	"Hydrogen evolution current"	68
Figure 5.4	"Current efficiency"	70
Figure 5.5	"The influence of nitrate ions"	71
Figure 5.6	"Cu-Zn pyrophosphate solution 1 hour old"	72
Figure 5.7	"Cu-Zn pyrophosphate solution 2 hours old"	73
Figure 5.8	Applied and partial currents of Cu & Zn"	74
Figure 5.9	"Partial current densities during brass deposition	76
Figure 5.10	"RDE rotation speed"	77

Figure 5.11	*"Current density fluctuation"*	*78*
Figure 5.12	*"pH at RCE surface: Rotation speed 1000rpm"*	*79*
Figure 5.13	*"pH at RCE surface: Rotation speed 500rpm"*	*80*
Figure 5.14	*"Copper pyrophosphate species"*	*81*
Figure 5.15	*"Zinc pyrophosphate species"*	*82*

Chapter 6 - Material Characterisation

Figure 6.1	*"XRD pattern of a 15.89 wt % zinc brass foil"*	*85*
Figure 6.2	*"XRD pattern of a 22.12 wt % zinc brass foil"*	*87*
Figure 6.3	*"XRD pattern of a 38.75 wt % zinc brass foil"*	*89*
Figure 6.4	*"XRD pattern of a 44.53 wt % zinc brass foil"*	*91*
Figure 6.5	*"XRD pattern of a 55.16 wt % zinc brass foil"*	*93*
Figure 6.6	*"XRD pattern of $CuZn_5$"*	*95*
Figure 6.7	*"Phase diagram of electroplated brass versus plating potential"*	*96*
Figure 6.8	*"Electroplated brass (39.09 wt % Zn)"*	*97*
Figure 6.9	*"Surface profile of electrodeposited brass with the absence of KNO_3 from the plating bath"*	*98*
Figure 6.10	*"Brass deposited at a low rotation speed"*	*98*
Figure 6.11	*"Scanned EDAX image of a brass foil"*	*99*
Figure 6.12	*"Predominantly a sea of nano sized grains"*	*100*
Figure 6.13	*"A large island of martensite"*	*101*
Figure 6.14	*"A small grain of martensite"*	*101*
Figure 6.15	*"Re-heating stage of brass foil (39.73 wt % zn)"*	*102*
Figure 6.16	*"Cooling stage of brass foil (39.73 wt % zn)"*	*103*
Figure 6.17	*"Re-heating stage of brass foil (41.19 wt % zn)"*	*103*
Figure 6.18	*"Annealed brass foil (41.19 wt % zn)"*	*103*

Tables

Chapter 6 - Material Characterisation

Table 6.1	*"Diffraction angles for a 15.89 wt % brass foil"*	*84*
Table 6.2	*"Diffraction angles for a 22.12 wt % brass foil"*	*86*
Table 6.3	*"Diffraction angles for a 38.75 wt % brass foil"*	*88*
Table 6.4	*"Diffraction angles for a 44.53 wt % brass foil"*	*90*
Table 6.5	*"Diffraction angles for a 55.16 wt % brass foil"*	*92*
Table 6.6	*"Diffraction angles for $CuZn_5$"*	*94*

Appendix A

Table A1	*"Copper-zinc pyrophosphate electrolyte used for the deposition of all brass foils"*	*121*
Table A2	*"Copper pyrophosphate electrolyte"*	*121*
Table A3	*"Zinc pyrophosphate electrolyte"*	*122*
Table A4	*"Pyrophosphate electrolyte with no metal ions"*	*122*

Appendix B

Table B1	*"Electroplated copper underlayer"*	*124*
Table B2	*"Mild steel XRD sample holder"*	*124*
Table B3	*"Lattice constants of 9R martensite of Cu-Zn alloys"*	*126*
Table B4	*"Martensite reflections observed in the electrodeposited brass foil of composition 38.75 wt % zinc"*	*126*

Symbols

v_a	*rate of dissolution*
k_a	*anodic reaction rate constant*
R	*gas constant, 8.314 J/mol-deg*
v_c	*rate of discharge*
M^{n+}	*concentration of metal ions*
k_a	*cathodic reaction rate constant*
ΔG	*Gibbs function*
ΔG^*	*free energy of activation*
n	*no. of electrons*
F	*Faradays constant, 96,487 C*
ϕ	*electrostatic potential, V*
T	*temperature*
E	*potential, V*
E_{eq}	*equilibrium potential, V*
α	*transfer coefficient*
η	*overpotential, V*
i_c	*cathodic current density, A/cm^2*
i_a	*anodic current density, A/cm^2*
i_0	*exchange current density, A/cm^2*
i	*current density, A/cm^2*
J_i	*flux of species (mol sec^{-1} cm^{-2})*
D_i	*diffusion coefficient of species*
C_i	*concentration of ionic species, mol/cm^3*
∂	*electrostatic potential, V*
(x)	*distance from electrode surface*
z_i	*valency*
v	*fluid velocity vector*

CHAPTER 1

- BACKGROUND -

1.0 BACKGROUND

In the scientific literature there is much confusion surrounding the date when the shape memory effect was first reported. Some believe that the first recorded observation of shape memory behavior was in 1932 by Chang *et al* [1]. They witnessed this transformation in a AuCd alloy by metallographic observations and resistivity changes.

Others believe this transformational behavior was first referenced when it was seen in brass (CuZn) in 1938 [2], but it was not until 1962 when shape memory effect was officially reported by Buchler *et al* [3] when they discovered the property in equiatomic nickel-titanium alloy (NiTi). It was this discovery that sparked research in this field. In the following 10 years a number of commercial shape memory alloy products were available on the market, mostly for use as biomaterials which include dental arch wires, vena cava filters and orthopedic bone implants for use in hospitals all around the world. Shape memory alloy (SMA) research has continued at an increasing pace since then.

The development of new materials will be of central importance in the future technological advance. We have not set our sights on producing a new material, but to exploit shape memory alloys and their numerous unique properties to enable the construction of devices and machines that are more compact and that possess previously unthinkable capabilities. Shape memory behavior of certain metallic alloys, for example NiTi and CuZnAl, have important applications in defense and biomedical technologies [4,5]. At present, these alloys are manufactured by metallurgical means in bulk quantities. Although this field is still nascent, preliminary studies have shown that thin films of shape memory alloys have high power to volume ratio [6], which makes them attractive candidates for miniaturisation technology. The technological problem to overcome is related to manufacturing and fabrication difficulties associated with creating such thin films. This thesis will show if

electrodeposition, a simple and relatively cheap method, can be used to construct shape memory thin films.

1.1 SHAPE MEMORY ALLOYS

The term 'shape memory alloy' refers to a group of metallic materials in which some fixed shape has been memorized, is plastically deformed at low temperatures and then subsequently heated above the transformation temperature, it reverts to the original shape. If the specimen is cooled again, and does not return to the shape it had when deformed at low temperatures - then this material is referred to as having a 'one-way shape memory'. Materials that undergo a change in shape upon cooling are referred as materials as having a 'two-way shape memory'. This metamorphosis occurs by a 'martensitic solid state transformation'. That is to say a martensite phase is formed upon cooling from a higher temperature phase called the parent phase or austenite phase by a lattice transformation wholly without atomic diffusion. There are little more than ten binary alloys which exhibit the shape memory effect, but more than a hundred with the addition of a subsequent alloying element.

1.2 PHASES AND PHASE TRANSFORMATION

Martensite

Martensite normally appears as platelets, resting on complex crystallographic planes called habit planes. In many shape memory alloys, the martensite plates are large and easily viewed through an optical microscope. When viewed with transmission electron microscopy (TEM), the plates are seen to possess a herringbone structure. Each martensite plate is a single crystal whose lattice orientation is strictly determined by the lattice orientation of the parent phase. The physical plane of the martensite plane also has a definite

orientation (parallel) with respect to the crystallographic plane (habit plane) of the parent phase. It is along this habit plane in the parent phase that the principal shear displacement occurs in the martensite reaction; hence the individual martensite plates grow by the movement of the habit plane through the parent phase. It is these habit planes, that separate the parent and product phases. When the plates stop growing, they usually have a lenticular shape, the major radius being limited by impingement with a grain boundary of the parent phase or with another plate. The plates thicken only to a limited extent and the final structure of the transformation product is always isolated plates embedded in untransformed parent phase.

A precise definition of martensite has never been agreed upon. The term 'martensite' was originally adopted by metallurgists to define a plate-like or acicular phase structure in quenched steel, although some argue the point. The term martensite is now widely accepted as a more generalized definition, referring to the type of transformation product that results from a certain kind of solid-state transformation, irrespective of the composition, structure or properties of the product.

During a martensitic transformation, the martensite takes on the same ordering of the austenite. This is called inherited ordering. The martensite crystal structure is made up of a lattice of 'zig-zagged' atoms (superimposed overview), which allows the metal to be soft and ductile. The austenite phase is susceptible to long range ordering. From a structural standpoint the martensitic products have little in common. The lattices range from simple to complex and display the many variations found in the products of other solid-state transformations. All martensites are solid solutions (more than one metal dissolved in each other).

Austenite

The term austenite, like martensite was originally intended to refer to a specific phase in steel; the parent phase in steel from which the martensite

phase is formed. In comparison to the zig-zagged structure of martensite, the austenite crystal structure on the other hand, consists of an ordered row-column matrix of atoms, which means the metal is hard and rigid. However, the chemistry of both solid solutions, remains identical.

The austenite phase of shape memory alloys are generally based on a body centred cubic (BCC) symmetry, some with the BCC symmetry, but more often with the B2 structure, and some with an even more complex ordering called DO3 still based upon a BCC symmetry. In some shape memory alloys possessing the BCC structure, atoms are disordered meaning that different elements are randomly distributed on the lattice sites. In others the atoms are ordered, meaning that the atoms are found on very specific sites. Martensite may form out of a disordered or ordered parent phase.

Martensitic Transformation

In contrast to diffusional transformations, where a new phase can only be formed by atoms moving over relatively long distances to create a different chemical composition than the matrix from which it is formed, martensitic transformations almost always occur by displacive transformation, where atoms do not move more than interatomic distances. In displacive transformations therefore, the atoms are cooperatively rearranged into a new, more stable crystal structure, but without changing the chemical nature of the matrix. The total displacement of any given atom relative to its nearest neighbors is less than the dimensions of the unit cell. Because no atomic migration is necessary, these displacive transformations generally progress in a time-dependent fashion, with the motion of the interface between the two phases being limited only by the speed of sound. They are referred to as athermal (without a change in heat content, as temperature changes) transformations, since the amount of the new phase present is usually dependent only on temperature.

1.3 TRANSFORMATION MECHANISM

The unique interaction between the martensite and austenite crystal structures, involves principally two processes, a lattice transformation involving shearing deformation, and a following cooperative atomic movement.

(a) Bain strain

The bain strain (lattice deformation), consists of all the atomic movements needed to produce the new structure from the old, Fig 1.1. The austenite structure is schematically illustrated in Fig 1.1(a), and the progression to a fully martensitic structure is schematically illustrated by Fig 1.1(b) to (d). The succession of the diagrams shows that as the interface progresses one atomic layer, each atom is required to move by only a very small amount Fig 1.1(c).

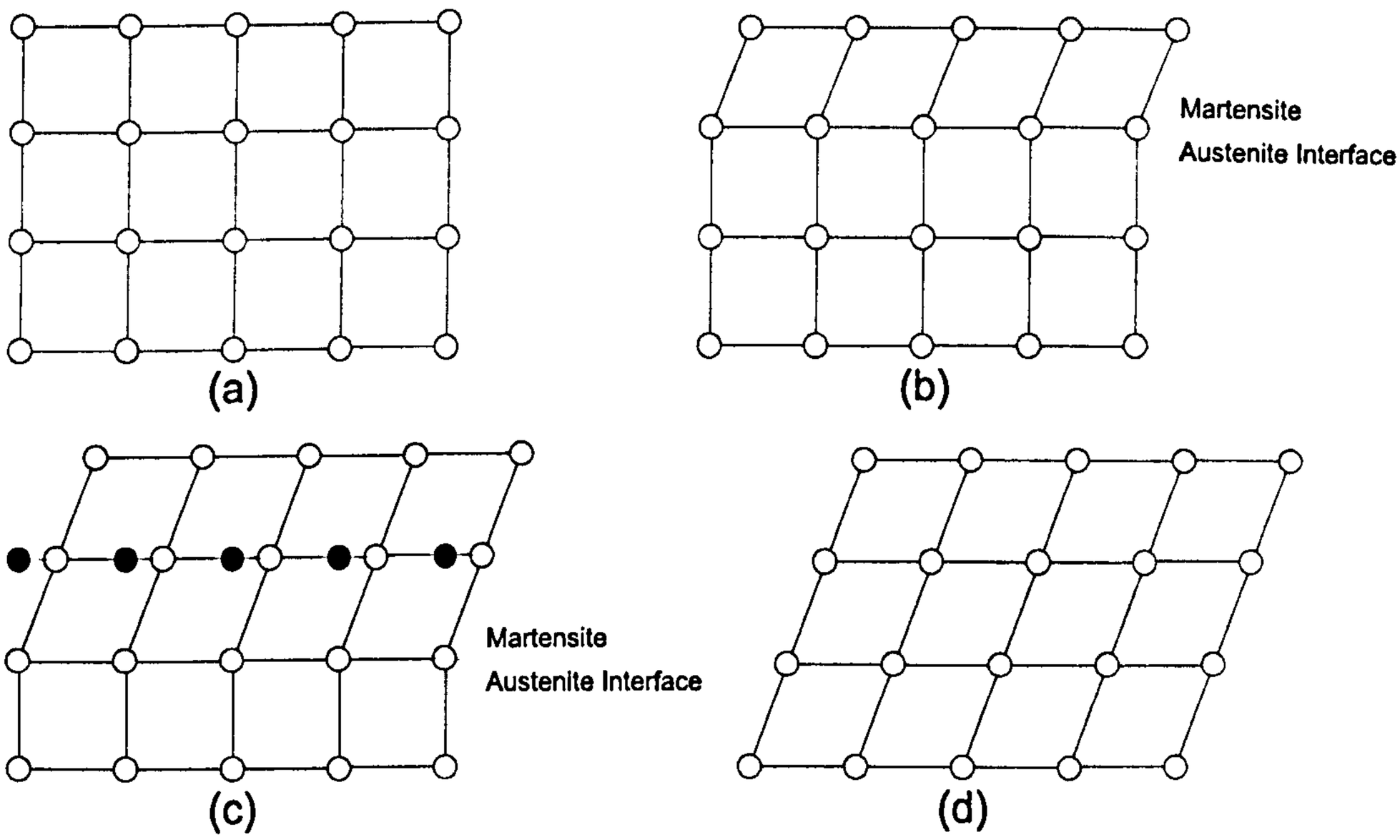

Figure 1.1 "The Bain Strain"

(a) austenite structure; (d) martensite structure; (b) & (c) transformation steps

The end results of all these small coordinated movements is the new martensitic structure, and the movements needed to produce the new structure are called the Bain strain. In reality, the Bain strain generally consists of several small atomic shuffles in addition to the type of movement illustrated in Fig 1.1.

(b) Lattice-invariant shear

The second part of the martensitic transformation, the lattice invariant shear, is an accommodation step. The martensitic structure produced by the Bain strain is of a different shape, and often volume, than the austenite phase surrounding it (compare Fig 1.1(a) and (d)). Martensite in steel involves both a volume and a shape change, whereas shape memory alloys such as Ni-Ti undergo basically only a shape change. Therefore, either the overall shape of the new phase, or the surrounding austenite must be altered to accommodate the new structure. To compare by analogy, one cannot change the shape of a single brick in the centre of a brick wall - either the surrounding bricks must deform, or the new brick must accommodate its form to the space available. There are two general mechanisms by which this can happen (i) slip, Fig 1.2(a) and (ii) twinning Fig 1.2(b).

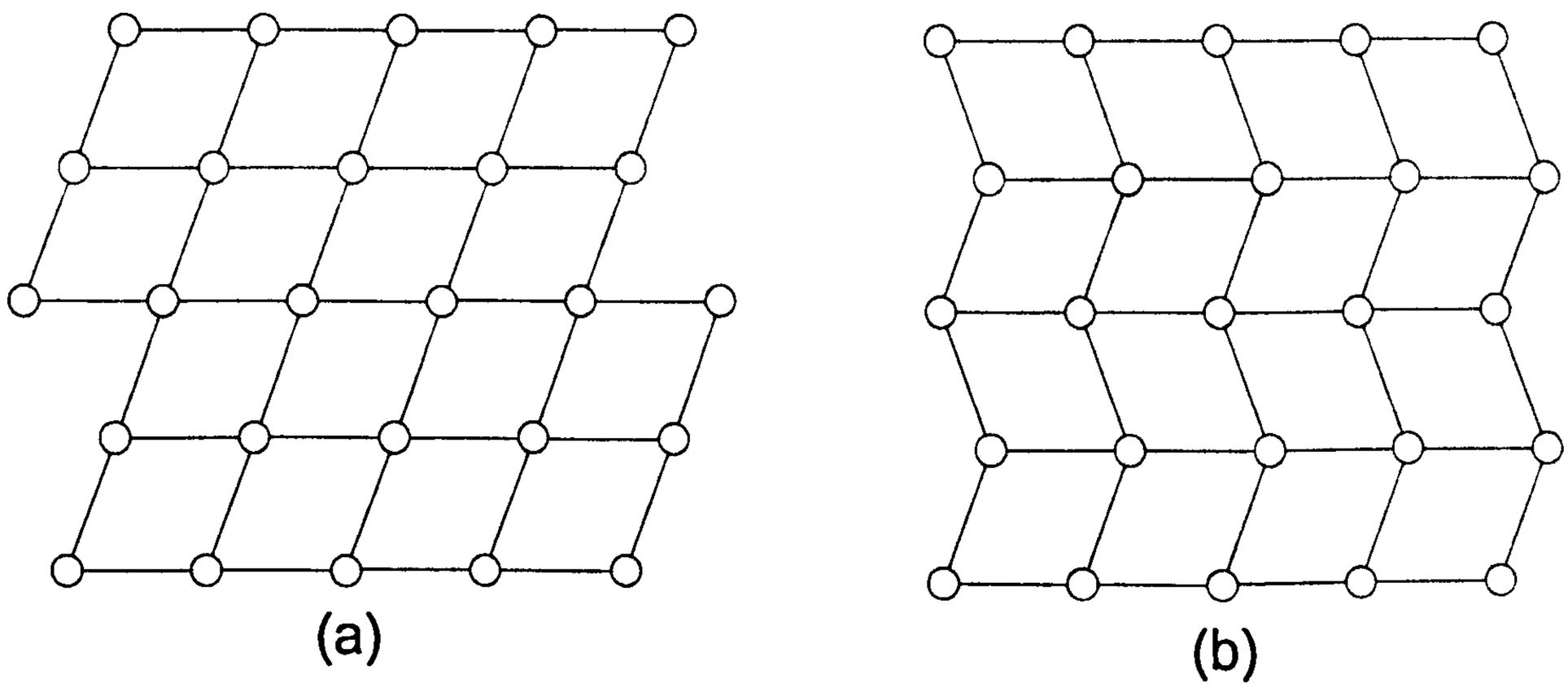

Figure 1.2 "Lattice-invariant shear"

Accommodation step by (a) slip and (b) twinning

In both cases, each individual cell, has the new martensitic structure, but the overall shape is that of the original austenite. Slip is a permanent process and is a common accommodation mechanism in many martensites. Twinning however, is unable to accommodate volume changes should that be necessary, but can accommodate shape changes in a reversible way. For shape memory to occur to a significant extent, we require that the accommodation be fully reversible, therefore it is imperative, that twinning be the dominant accommodation process.

The twinning process of accommodation therefore, plays a major role in the shape memory effect. As illustrated in Fig 1.3, the twin boundary is in mirror plane, in this position on the boundary the view in one direction is a mirror of the other. Atoms situated on that boundary see the same number and types of bond lengths in both directions. Some key properties of twin boundaries are that they are of a very low energy and that they are very mobile, thus the relative stability of a martensitic phase is not strongly affected by the number or location of these boundaries.

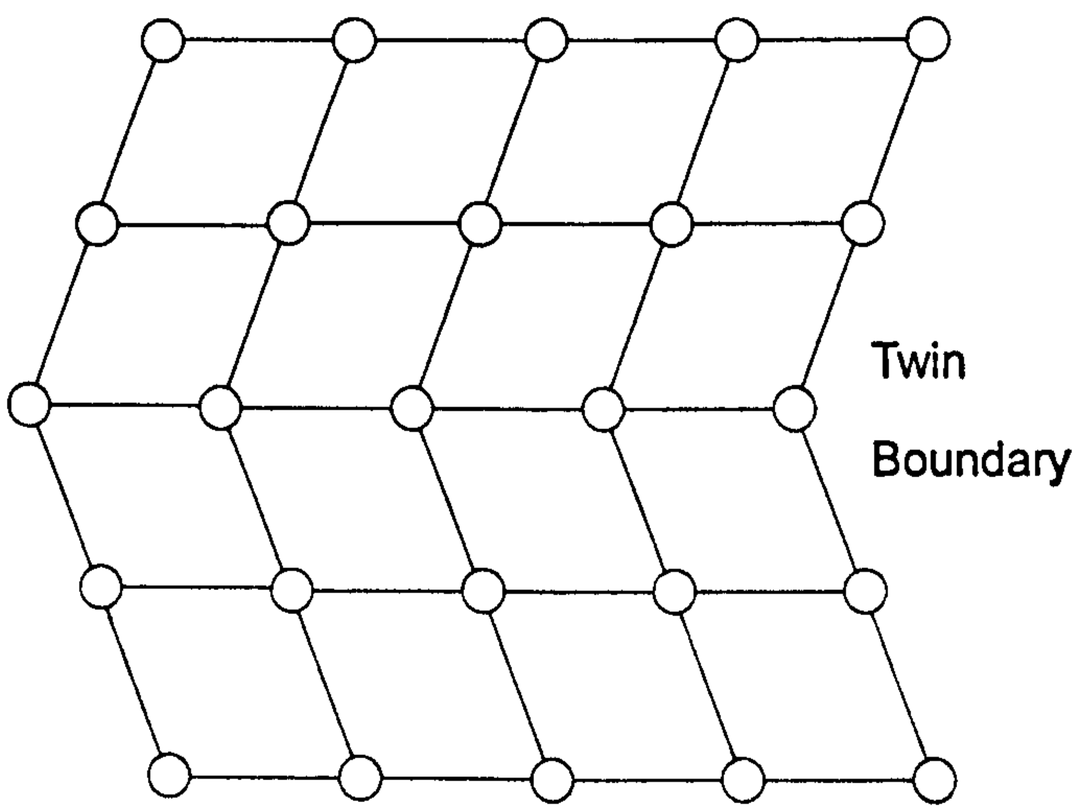

Figure 1.3 "Twin Boundary"

By comparing the edges of the structures shown in Figs 1.2 (a) and (b), one can see that slip accommodation requires that the atomic bonds be broken, while all bonds remain intact in the twinned structure. If a stress is applied to the structure shown in Fig 1.2 (b), the twin boundaries will easily move,

producing a shape which better accommodates the applied stress. An example is shown in Fig 1.4. The result of moving a twin boundary is thus to convert one orientation or twin variant into another. That variant will be chosen which is most favorably orientated to the applied stress. The ideal mechanism would be where, a single variant of martensite can be produced by straining a sufficient amount. This process (the condensation of many twin variants into a single favoured variant) is called detwinning.

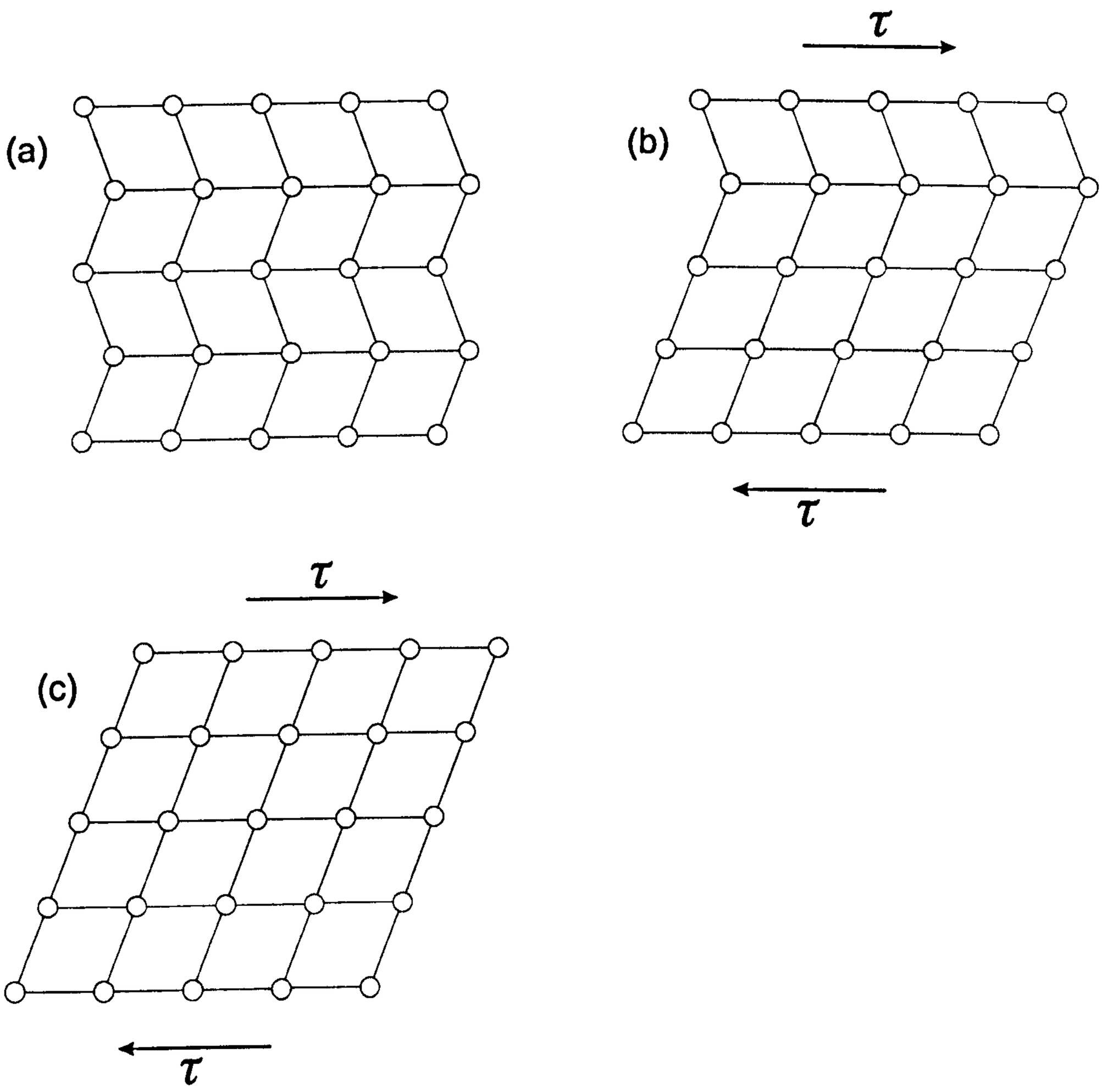

Figure 1.4 "Detwinning"

Twins not only act within individual martensite plates, the boundaries between martensite plates also behave as twin boundaries, i.e the individual plates of martensite themselves are twins with respect to adjoining plates. Thus the

term twin boundaries, generally refers to the boundaries between martensite plates as well as the boundaries within plates.

1.4 TRANSITION TEMPERATURE RANGE

Nearly all the physical properties of austenite and martensite are different, and thus as one passes through the transformation point, a variety of significant property changes occur. Thereby any of these properties (electrical resistance, length change, volume change etc...), can be used to monitor the progress of the transformation; this is best explained with the aid of the diagram illustrated in Fig 1.5.

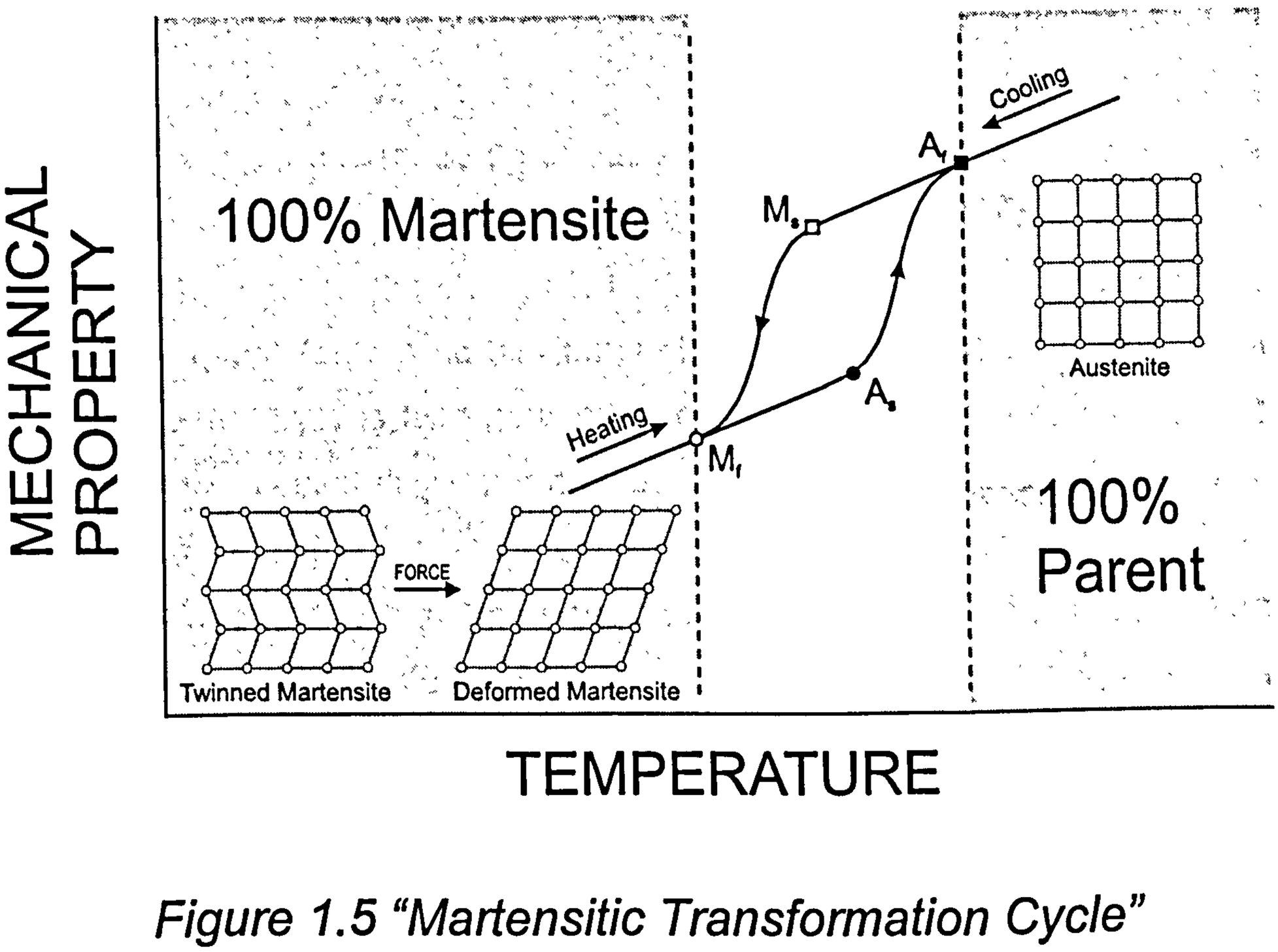

Figure 1.5 "Martensitic Transformation Cycle"

Starting (M_s) and finishing (M_f) temperatures of transformation to martensite; Starting (A_s) and finishing (A_f) temperatures of transformation to austenite.

First a memorized shape is imprinted into the SMA by holding the SMA in the desired shape at high temperature (the desired shape must also be held during the cooling process). On cooling the alloy passes through what is

called the *transition temperature range* (TTR). Below this range the alloy can be released from its constraints and appears pliable.

The temperatures, M_s, M_f, A_s and A_f, are indicated in the graph and refer to the temperatures at which the transformation to martensite starts and finishes, and the temperatures at which the reversion to austenite starts and finishes. On cooling from the setting temperature, temperature M_s is reached, at this point the crystal structure starts to change from, what has up to now been completely austenite, to a martensite structure. This martensite transformation is completed by the temperature M_f where all the metal now consists of martensite phase.

On re-heating, a temperature of A_s has to be reached, (note $A_s > M_f$), before the metal's crystal structure starts to revert back to the austenite phase. The transition temperature range is the temperature range between A_f, where all the crystal structure is made up of austenite structure, and M_f. Below M_f, the alloy may be mechanically deformed with no loss to the shape memory properties, so long as the change is kept below the 8 percent surface, plastic deformation limit (only a certain amount of martensitic deformation can be accommodated by this twin movement process and once this is exceeded, the material will eventually deform by the irreversible processes of dislocation movement). After the metallic form has received some form of deformation and is reheated beyond A_f, the crystal structure will reform the metallic form that was "memorized" into the austenite phase of the metal during the period the metal was trained.

Martensite transformations are first order transformations, meaning that heat is liberated when martensite is formed. It is visible from Fig 1.5, that there is a hysteresis associated with the transformation, showing the transformation temperatures to differ upon heating and cooling (this is the temperature range over which austenite and martensite co-exist). The magnitude of the hysteresis depends upon the alloy, but values of 20-40°C are typical for shape memory alloy systems. The start of the hysteresis temperature range

also varies with varying alloy composition. Microscopically, hysteresis can be thought of as the friction associated with the movement of twin-related martensite boundaries.

The shape memory effect occurs due to the fact that, as the temperature is raised above A_s, a stress forms in the crystal structure and the atoms return to their austenite phase to relieve this stress. The shape that the crystal structure forms is the one that was 'memorized' into the austenite phase of the metal during the imprintation process. This transition to austenite from the martensite crystal structure is completed at A_f.

1.5 CuZn SHAPE MEMORY ALLOY

Among the large number of SMA's which have been discovered, apart from TiNi, most are copper based and are virtually the only ones which can be used practically. Among these alloys, two groups are currently being developed for practical usage, CuAl-based and CuZn-based alloys. Because of the potential application of SMA's in numerous fields, economics is now also an important consideration in determining the choice of alloy, for example the copper based alloys seem an attractive choice as a replacement for TiNi, as in some circumstances the TiNi alloy can cost ten times as much.

Aluminum can only be electroplated from molten salt electrolytes, which require specialised materials and apparatus, which make CuAl-based alloys more expensive. This thesis is concerned with the development of CuZn based alloys as new functional materials. As a first step, Cu-Zn shape memory thin films have been plated and studied. This will provide a stepping stone to study if ternary Cu-Zn-based alloy thin films can useful.

To understand clearly the shape memory effect that brass displays, it is first necessary to be familiar with the Cu-Zn equilibrium phase diagram.

1.6 THE Cu-Zn EQUILIBRIUM PHASE DIAGRAM

The equilibrium diagram of the copper-zinc system is shown in Fig 1.6. The binary alloy equilibrium diagram can be modified by the addition of another element, aluminum or tin for example. The seven solid phases, plus the other main features in the copper-zinc system are described as follows.

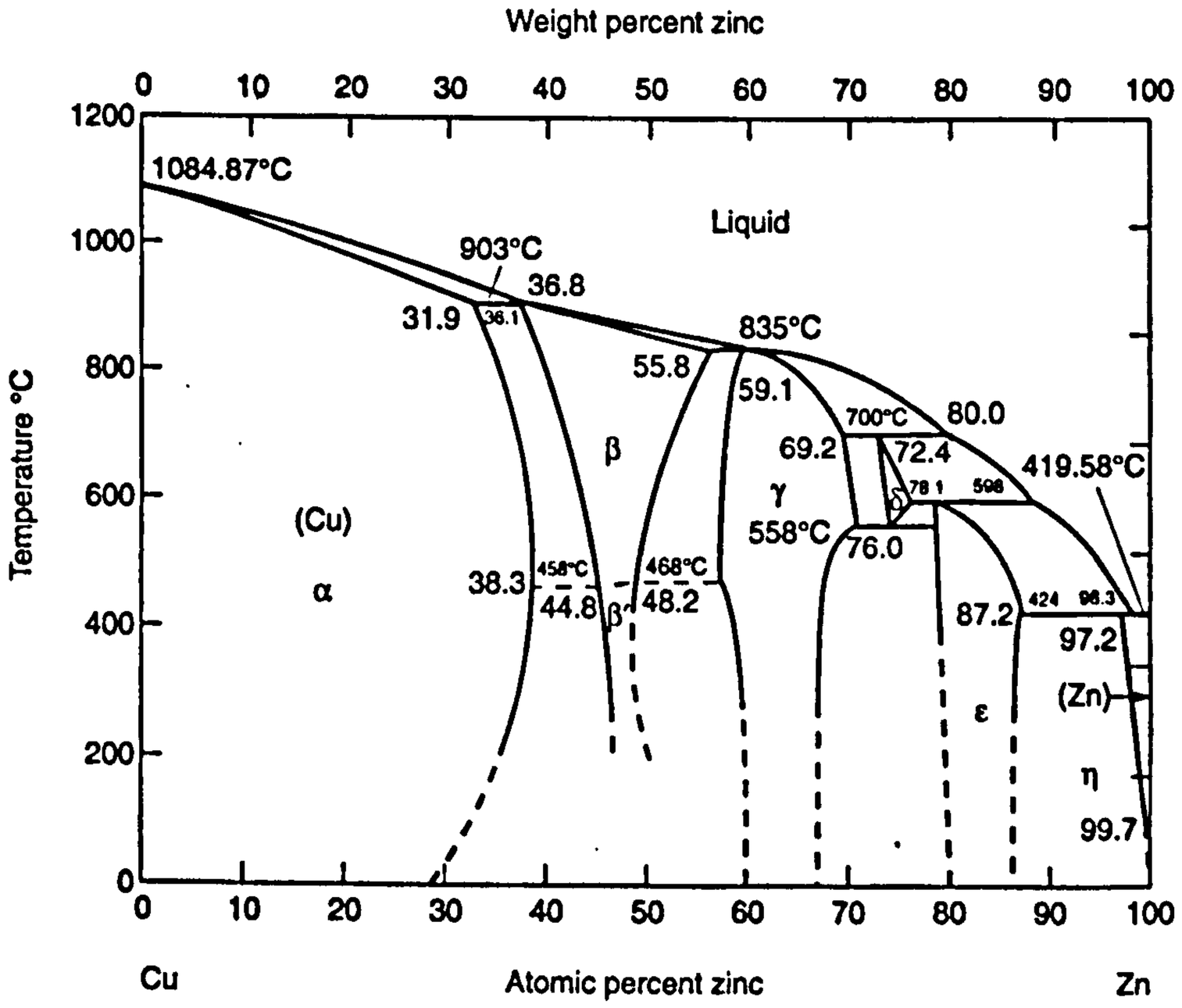

Figure 1.6 "The Cu-Zn Equilibrium Phase Diagram"

Liquid Region

Above 1100°C, both metals have exceeded their melting points and form a miscible liquid regardless of the compositional ratio of the metals.

Liquid - Solid Regions

This region is also known as the freezing point range. Here we have two narrow liquidus/solidus ranges and two peritectic horizontals.

Solid Solution Regions

When the molten alloy crystallizes it does so as a true solution, that is to say it forms homogenous crystals containing copper and zinc - a solid solution.

α-Phase

Fig.1.6 shows that copper will dissolve a maximum zinc content of 38.3% at 458°C, falling to 31.9% at the peritectic (equilibrium between two solid and one liquid phase) temperature of 903°C. With extremely slow rates of cooling which allow the alloy to reach structural equilibrium, the solubility of zinc in copper will again decrease to 32.5% at 200°C. The solid solutions so formed in this region are referred to as the α-phase. This phase has a disordered atomic arrangement and a face centred cubic (FCC) structure based on the copper lattice. These alloys are malleable and ductile, ranging in colour from red to golden yellow and paler yellow with a greenish tinge at 30% zinc.

β-Phase

If the amount of zinc is increased beyond 38.3%, another phase, the β'-phase will appear if the brass is cooled slowly. This phase has an ordered body centred cubic (BCC) structure. Near room temperature, the β'-phase region extends from approximately 48 to 50 atomic % zinc. Above 458°C this phase modifies itself and becomes a disordered phase denoted as β. This transformation is shown in the phase diagram by a single running line from 458 to 468°C. Due to experimental difficulties associated with the speed of

the transformation, there are no details on this region, but it has been suggested that the β and β' regions are separated by a normal two-phase region β + β'. The β phase is hard at temperatures below 600°C and the α + β alloys are ochre to gold in colour.

γ-Phase

The γ phase is formed with further increases in the zinc content according to the second peritectic horizontal at 835°C, between solid β-phase and the residual liquid. Its crystal structure is a complex double cubic type, based on Cu_5Zn_8 and has become the prototype of the so-called γ brass structures. This phase is hard and brittle, being found in practice only in certain brazing alloys containing less than 50% copper.

Other Phases

These include the δ-phase, a body centred cubic structure which differs from the others because it is stable over a limited temperature range from 558 to 700°C. The ε-phase has a close packed hexagonal structure and the η-phase, a close packed hexagonal structure, based on the zinc lattice.

The phase diagram (Fig. 1.7) can be used to determine what happens when β brass is manufactured by metallurgical means. A liquid mixture of Cu and Zn containing 36 wt % zinc, will, on cooling from a liquid, meet the freezing point curve AD, where upon crystals of the solid solution α will start to grow. With further cooling the α crystals will become further saturated with zinc. At the peritectic horizontal BC, the α crystals are saturated and are incapable of taking up any further zinc. Simultaneously at this point, the last of the liquid alloy solidifies to form β crystals. Once solidified, most of the alloy will be represented as the β phase, simply because at this composition and temperature the saturation composition of the α-phase is represented at point B, and the β-phase at point C. Thus the ratio of α:β can be determined from

where the point along the x-axis equivalent to 36 wt % zinc, cuts the line BC; this intersection point is denoted X. The ration of α phase to β phase is then determined by the Lever rule (1).

$$\frac{Length\ BX}{Length\ CX} \equiv \frac{Amount\ of\ \beta - phase}{Amount\ of\ \alpha - phase} \qquad (1)$$

With further cooling this ratio is seen to decrease, as with a change in temperature comes the change in saturation behaviour of the phases. Thus the amount of α-phase will increase and β-phase will decrease. This process occurs by solid state diffusion. However, solidified equilibrium is rarely fulfilled as cooling of the alloy through the solidifying range of temperature needs to be extremely slow.

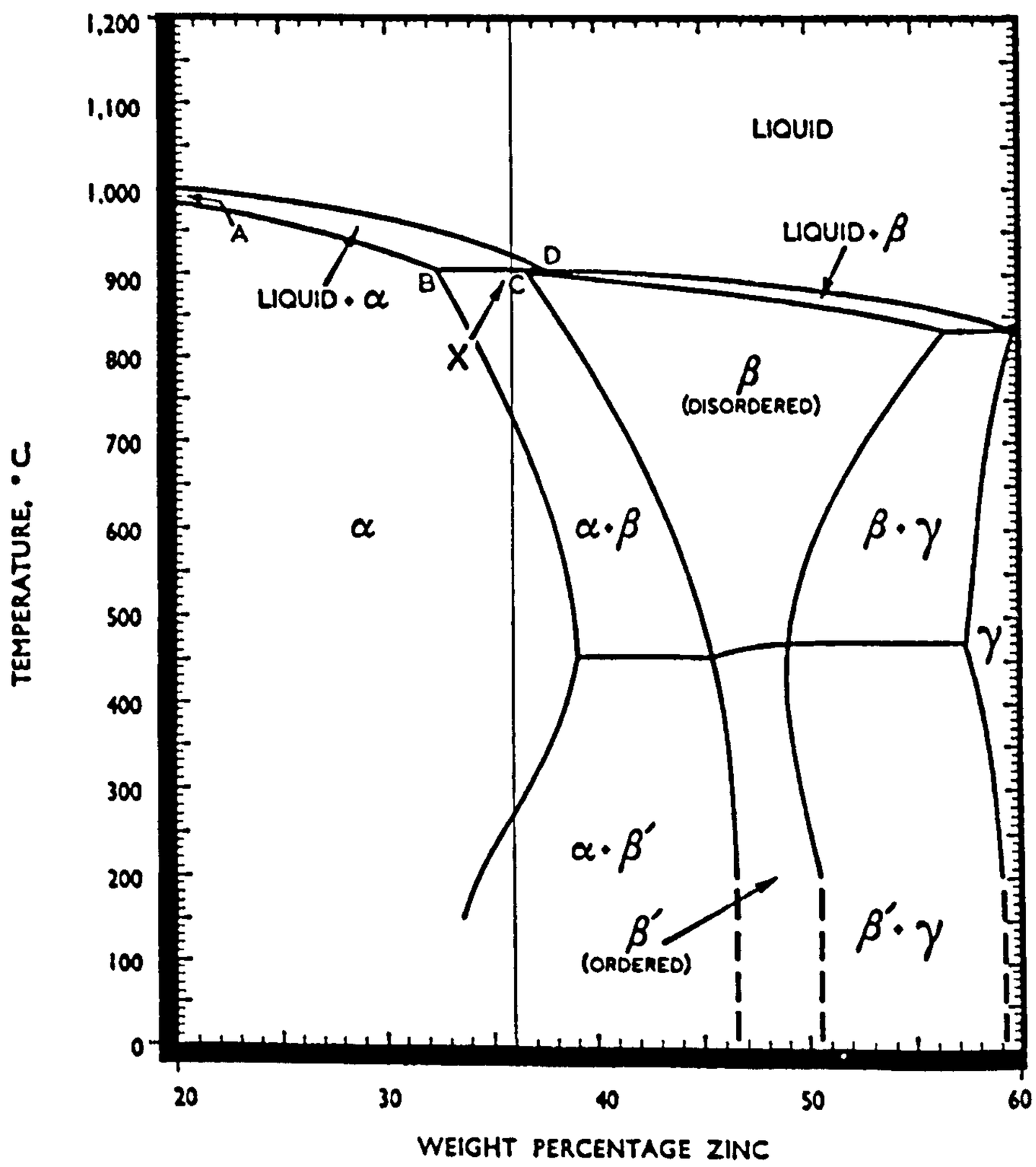

Figure 1.7 "Calculation of Phase Ratio"

1.7 SHAPE MEMORY REGION IN BRASS

Brass displays a complete shape memory effect. For metallurgically cast prepared brass samples, the transformation only occurs within a narrow composition range of 38.5 - 41.6wt % zinc [7]. The transformation, although a first order phase change (reaction proceeds as a function of time), does not occur at a single temperature but over a range of temperatures varying with the alloy composition. The Cu-based alloys tend to form the equilibrium α or γ-phases during cooling. However, in order to obtain good reliable shape memory behaviour, only the β-phase should be retained. Once at room temperature the β-phase will be present as a stable single phase. At higher temperatures the β-phase may precipitate back to the equilibrium phase, depleting the β-phase matrix; this will in effect cause a shift in M_s [16].

Parent Phase

The parent phase of Cu-Zn like most parent phases of shape memory alloys which sustain thermoelastic martensitic transformations have fundamental superlattices with body-centered cubic (BBC) structures - classified as β phase alloys. Cu-Zn alloys which display shape memory behavior have close to a 50:50 composition ratio and the β phase has an ordered crystal structure like that of CsCl and denoted as β_2. Thus the crystal structure is referred to as a B2 superlattice (β_2 parent phase). Clearly the ideal B2 superlattice can only be formed at an equiatomic composition (Fig.1.6). Nevertheless, ordering reactions leading to such types of superlattices occur in a broad range around this exact composition in the Cu-Zn system.

Fig.1.8(a) shows the unit cell structure of the parent phase in shape memory brass; (b) and (c) shows the arrangement of the atoms in the (110) plane for

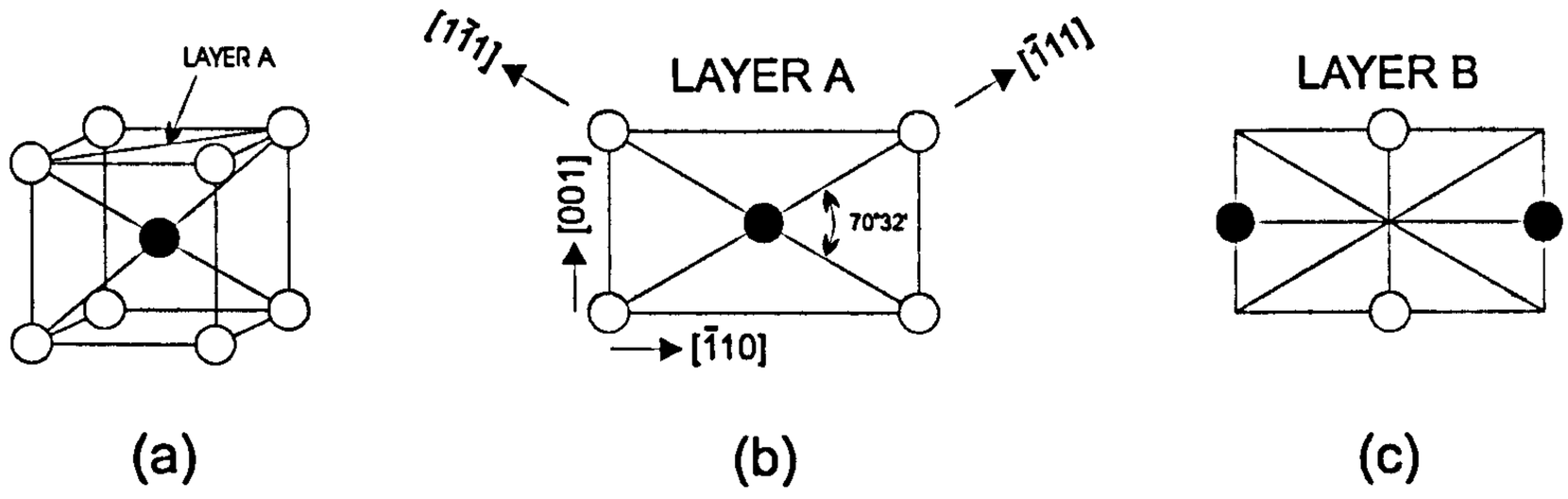

Figure 1.8 "Parent Phase Structure"

Parent phase is a body centered cubic lattice stacked ABABAB.

the stacking planes A and B respectively. The cubic structure in (a) can be viewed as the result of alternatively stacking the planes pictured in (b) and (c) to give a stacking sequence ABABABAB.

Martensite Phase

As in all copper based alloys, martensite has a close packed layer structure, with close packed planes, commonly called basal planes, derived from the (110) planes of the parent β phase. This is because when the martensite transformation occurs in this β-phase alloy, it is due to the deformation (towards a hexagon) of the (II0) planes themselves, and a shearing including some shuffling in the [$\bar{1}$00] direction along the (II0) plane. Once this transformation has taken place, the resulting martensitic crystal structures now consist of these types of close packed stacking planes (Fig 1.9).

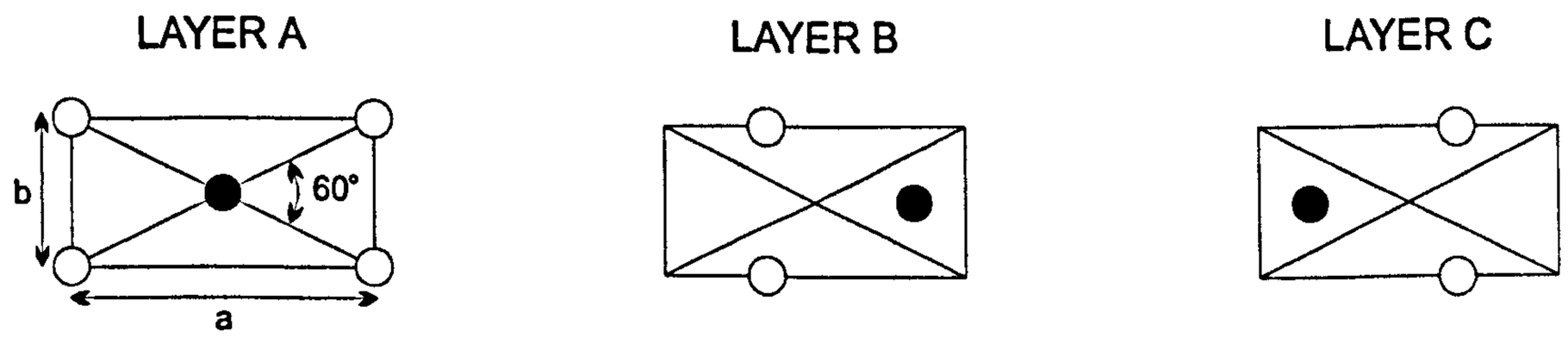

Figure 1.9 "Martensite Stacking Planes"

Martensite phase is a inclined monoclinic lattice, stacked ABCBCACAB.

There are three types of martensite phase observed to form in copper-based alloys. In shape memory Cu-Zn systems, martensite always adopts a stacking of nine close-packed layers in the sequence ABCBCACAB, that is as a face centered cubic structure with one intrinsic stacking fault on each third plane. The Ramsdell short-hand notation is usually employed in describing close-packed layer structures. However, *Delaey et al* [17] have proposed a new nomenclature, claimed to offer a number of advantages to describe long period stacking orders in martensitic β-phase alloys. The structure of β' is thus denoted as M-9R, signifying that it has a period of nine layers divided into three sub-periods (rhombohedral symmetry). Fig.1.10 is a diagram of the crystal structure of β' martensite formed from the alloy CuZn with a 9R structure. The exact stacking positions are 1/2.79 and 2/2.79. Consequently, the c-axis cannot maintain a right angle relative to the 0^{th} layer, and a slightly inclined "monoclinic lattice" results. Thus most of the martensites with long period stacking order structures which occur in β alloys are not orthorhombic, but are instead monoclinic lattices. These are distinguished by the prefix M, as in M9R.

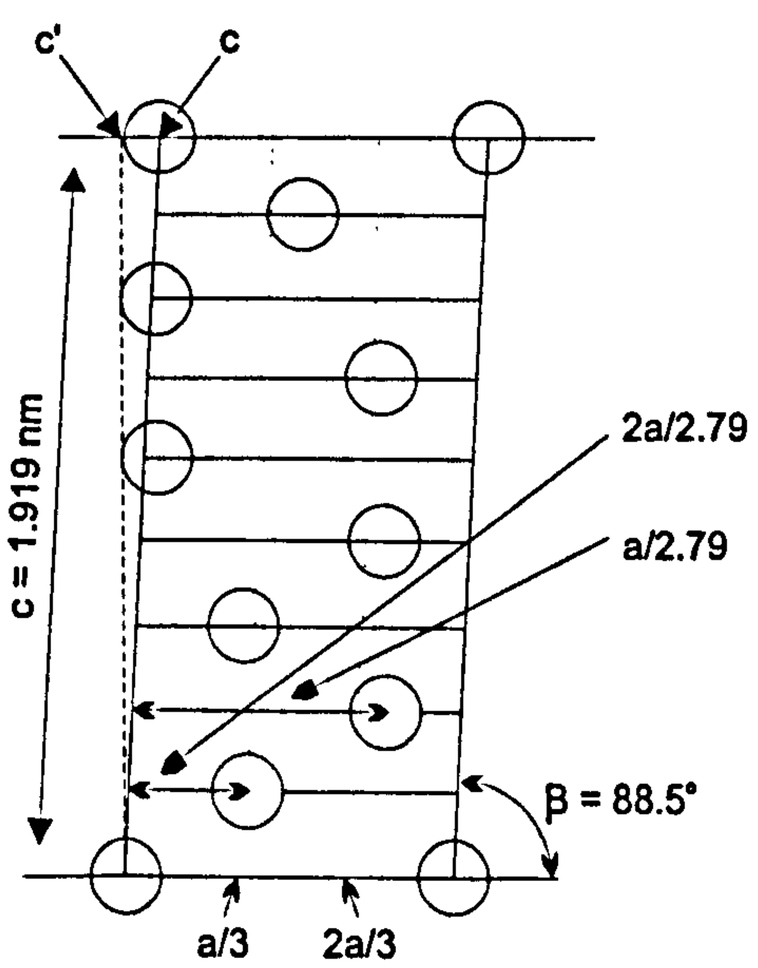

Figure 1.10 "β' martensite - M9R"

1.8 TERNARY ALLOYS

Only TiNi and Cu-based shape memory alloys are presently available for commercial shape memory applications. TiNi alloys usually exhibit better shape memory properties and corrosion resistance than do Cu-based alloys, but in economic terms Cu-based alloys are more attractive, as they cost ten times less than TiNi alloys.

Current Cu-based shape memory alloys are derived from three binary alloy systems, Cu-Zn, Cu-Al and Cu-Sn. However the martensitic transformation in Cu-Sn alloys is not ideally thermoelastic and suffers from a rapid degradation of shape memory properties. Cu-Zn-based ternary systems are highly ductile relative to other Cu-based alloys and resist fractures at grain boundaries.

Grains of alloys with a fourth element added have been test manufactured, and their properties are basically not different from the ternary alloys.

REFERENCES

1. L.C.Chang and T.A.Read, Trans. AIME, Vol 191, 1951, p.47
2. A.B. Greninger and V.G. Mooradian, Trans. Met. Soc. AIME, 1938, 128, p.337
3. W.J. Buehler, J.V. Gilfrich, and R.C. Wiley, J. Appl. Phys., Vol 34, 1963, p.1475
4. J.E.Bidaux, W.J.Yu, R.Gotthardt, J.A.E.Manson, Proc. of the 3rd European Symp. On Martensitic Transformations, Barcelona, Sept. 1994.
5. D.Reynaerts and H.Van Brussel, Proc. Int. Conf. on Shape Memory and Superelastic Technologies, Asilomar, CA, 1994.
6. J.Frimpong, C.H.Sonu, T.R.Hymer and T.J.O'Keefe, Proc. of SPIE, p.362, Washington, USA, 1993.
7. Brenner Electroplating, Wiley Press, 1963
8. C.A.Hamilton Jr., Plating & Surface Finishing, Vol 82 Prt 8, 1995, p.48
9. F.Passel, Plating, Vol 46, 1959, p 628
10. D.A.Luke, Trans. Inst. Met Finish., Vol 47, 1969, p.36
11. T.M.Tam, R.Taylor, J.Electrochemical Society, Vol 133, No 6, 1986, p.1101
12. T.M.Tam, G.A.Fung, J.Electrochemical Society, Vol 130, 1983, p.874
13. S.Miura, Y.Morita and N.Nakanishi, "Shape Memory Effects In Alloys", Ed. J.Perkins, Plenum Press, N.Y., 389 (1975).
14. A.D.Johnson and J.D.Busch, Proc. of the 1st International Conference on Shape Memory and Superelastic Technologies, Monterey, (1994).
15. M.Hanson and K.Anderko, "Consition of Binary Alloys", Metallurgy and Metallurgical Engineering Series (McGraw-Hill Book Company, NY) p.649 (1958).
16. L.Delaey, J.Van Humbeeck, R.Stalmans and M.Chandrasekaran, "On The Stability Of Shape Memory Alloys", Engineering Aspects of Shape Memory Alloys, Butterworth-Heinemann, p.96 (1990).
17. L.Delaey and M.Chandrasekaran, Scripta Metallurgia *et* Materialia, Vol 30, No 12, 1994, p.1605

CHAPTER 2

- PROCESSING METHODS -

2.0 PROCESSING METHODS

Currently, shape memory alloys are manufactured by metallurgical means into wires, rods, foils etc. This is either done by melting, casting [1,2] and shaping, followed by heat treatment cycles to obtain desired shape memory. Metallurgical methods however, cannot be easily used to fabricate shape memory thin films, mainly due to the constraints imposed by their size and the narrow regime over which the shape memory behavior is observed. In addition to this, a more serious problem associated with the preparation of brass based shape memory alloys via conventional techniques are dezincification and rapid grain growth. Addition of B, Ti and Zr grain refining elements have been employed to overcome these obstacles [3,4]. These act by either assisting nucleation or by inhibiting grain growth [5].

Powder metallurgy methods, therefore, have proved much more successful [3,6,7], for the production of Cu based shape memory alloys. Due to the presence of Al_2O_3, the growth of grains in the β phase is inhibited, leading to a much finer β phase grain size [8]. Regardless of the improved grain size, it is very hard to obtain a homogenous material using powder metallurgy. A long diffusion time is required to reach homogeneity.

In order to obtain shorter diffusion times, a mechanical alloying technique [9,10,11] is used. This process is able to produce shape memory alloys at room temperature without any melting process. Ultrafine microstructures have been produced with grain sizes in the order of nanometres, although as yet no thin films have been produced by such means [12].

2.1 PHYSICAL VAPOUR DEPOSITION

The technique employed to deposit a thin metal film, must be either physical condensation, or a chemical reaction deposition. There have been previous investigations carried out to fabricate thin films of shape memory materials by physical vapour deposition (PVD) methods.

Metal film deposition by sputtering was discovered in 1852 [13], sputtering was developed much later as a thin film deposition technique by Langmuir in 1923 [14]. A simple dc sputtering system as shown in Fig 2.1 consists of two conductive plates, one of which is a target plate, containing the material to be deposited and a substrate plate, upon which the film will be deposited. The two plates are connected to an external power supply and contained in a vacuum chamber. The plates are placed less than 10cm apart. An inert gas is then introduced in the chamber. The gas pressure in the chamber is held at about 0.1 torr. The low pressure of the gas results in a mean free path for gas molecules in the order of hundreds of microns. A plasma (partially ionized gas) is then created by initially applying a large voltage momentarily across the gap between the plates containing the low pressure gas to start the plasma. A high voltage arc will flash between the two electrodes, creating a large number of ions and free electrons from the gas.

Because of the electric field that exists between the two plates, the negatively charged electrons will be attracted to and accelerated towards the positively charged anode and the ions will be accelerated towards the negatively charged cathode. Due to their small mass the electrons will be accelerated more rapidly than the slow moving ions. The ions travel across the chamber and eventually strike the cathode. When they do so they release a cloud of secondary electrons from the target material in the cathode. These electrons in turn are accelerated toward the back toward the anode. When these high energy electrons collide inelastically with a neutral atom they create more ions. This process of secondary electron release and ion creation sustains the

plasma. Once the plasma is formed, ions in the plasma are accelerated toward the negatively charged cathode, where the object to be plated is placed. When they strike the surface, they release secondary electrons, which are accelerated away from the cathode. In effect they may collide with neutral plasma species while crossing from cathode to anode. If the energy transfer is high enough, however, the atom will ionize and be accelerated toward the cathode. It is this bombardment of the cathode in this ion stream gives rise to the process of sputtering.

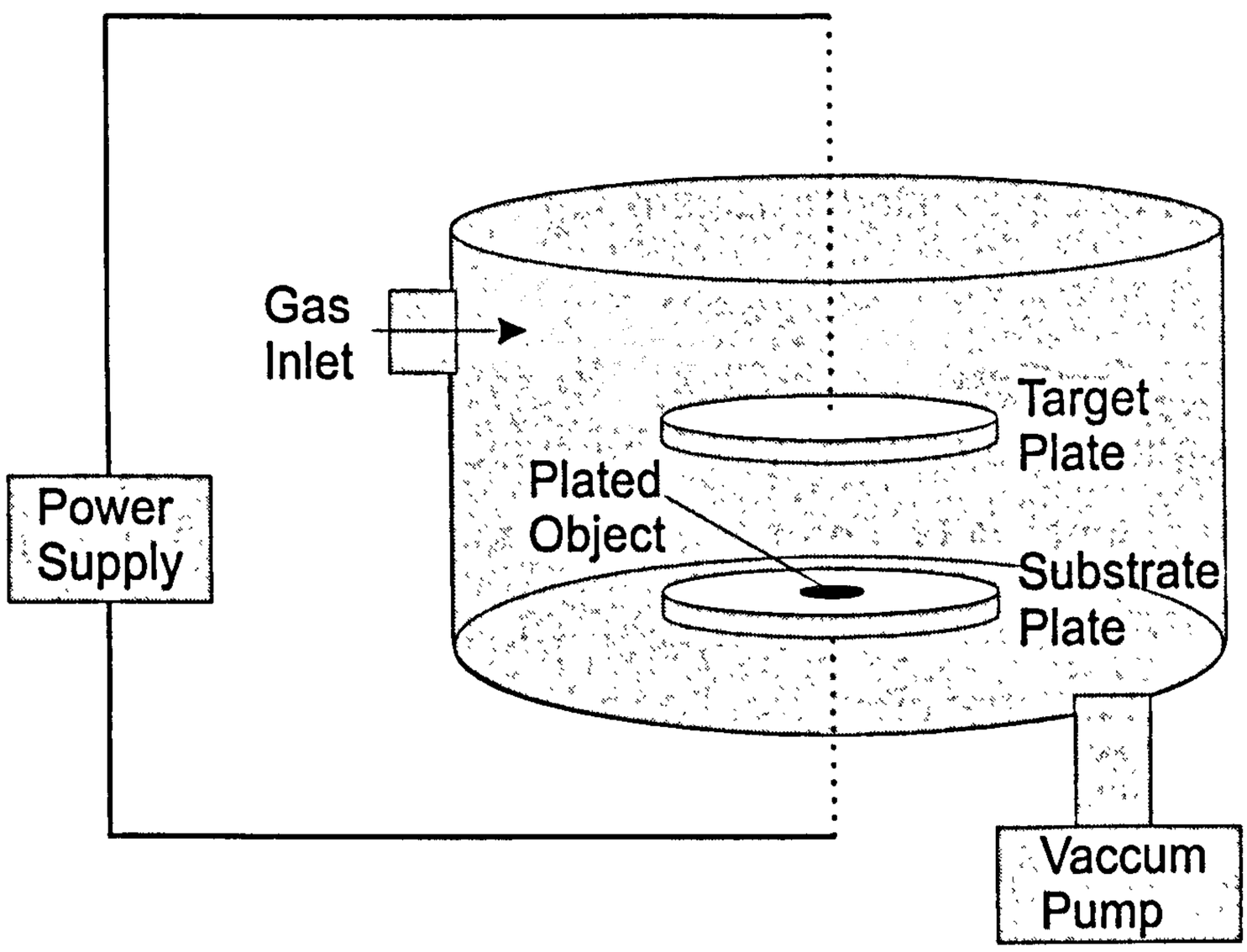

Figure 2.1 "A simple parallel plate sputtering system"

When an energetic atom strikes the surface of a material it will bounce off the surface if it has a low energy, or it will adsorb to the surface. At very high energies the ion is likely to penetrate into the material up to several atomic spacings, depositing most of its energies deep into the substrate, where it changes the physical structure. Once on the surface of the substrate the atoms will diffuse along the surface (especially those with high energies as they will possess additional surface mobility), until they form nuclei of critical size. Once stable nuclei are formed, they capture more atoms, forming

islands. Eventually the islands merge while still very thin, forming a smooth, continuous film.

Sputtering is very attractive due to the physical nature of the process, since it can be used to deposit not only lone elements but a wide range of materials and even insulating materials such as SiO_2. It is useful for the production of thin films, due to the apparent ease in extending the results obtained on a small research size scale, upgradable to a reliable production process. Other advantages for using sputtering include excellent film uniformity (particularly over large areas), surface smoothness, thickness control, good adhesion, very versatile, high rates of deposition and films with nearly bulk like properties. In the case of elemental metals simple dc puttering is usually favored.

However the disadvantages of sputtering are related to the morphology of the film, which is critically dependent on temperature and incident ion energy. At low temperatures and ion energy, the film will be amorphous and highly porous, with a low mass density. With an increase in temperature, a film of a small grain size is deposited. The size of grains keep increasing in size with further increases in temperature until large columnar grains with rough surfaces predominate.

It is difficult to use this technique for depositing alloys; the film composition is not the same as the target material and the composition of the film will vary with thickness. Since the deposit composition has to be controlled by transport properties of the constituents in the plasma, it is difficult to control the stoichiometry of the film. A further problem is related to stresses in the film. The film may have tensile or compressive stress, which is dependent on deposition temperature, deposition rate and film thickness. Finally, employing such a technique as sputtering, will incorporate high costs.

2.2 ELECTRODEPOSITION

Electroplating technology is essentially the electrodeposition of metals from an aqueous solution containing chemical compounds of the metals to be deposited. An electrochemical cell (Fig 2.2) must contain both a anode and a cathode and the charge transfer must be balanced between anode and cathode.

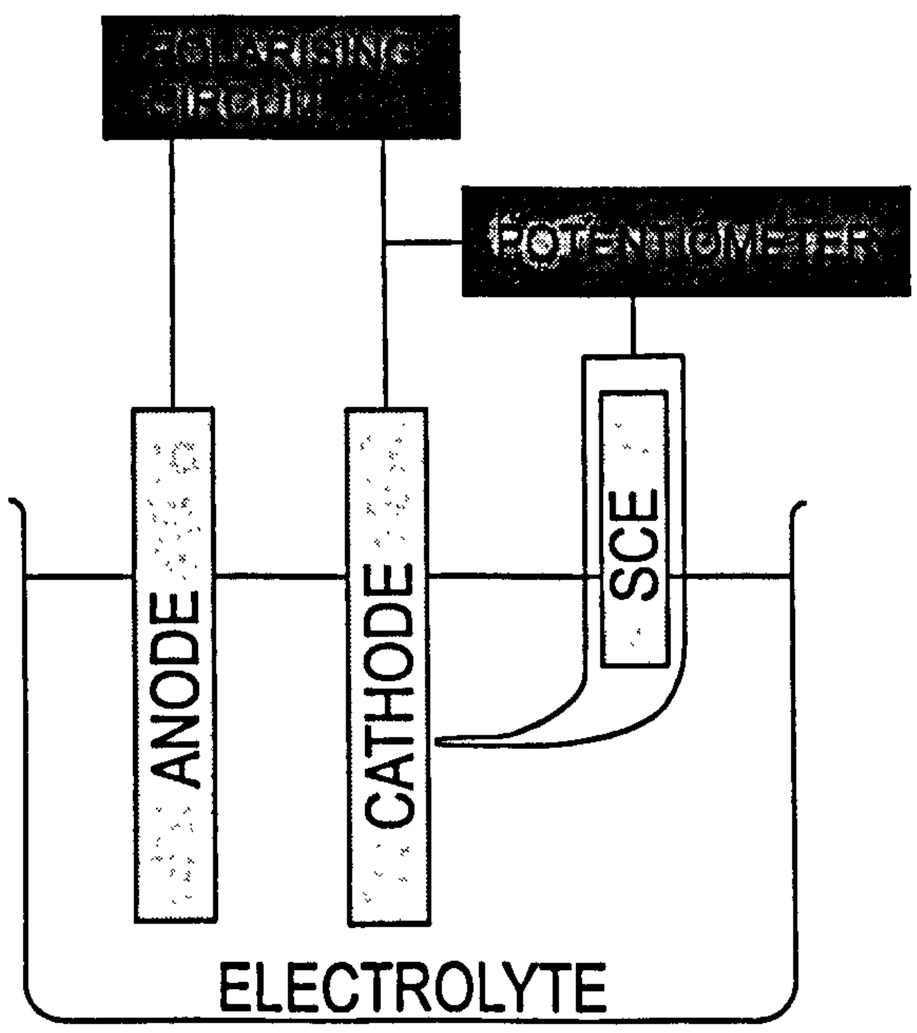

Figure 2.2 "The three electrode cell"

The discharge of a metal ion M^{x+} in solution at the cathode proceeds in accordance with (1) to form a metal.

$$M^{x+}_{(aq)} + xe^- \rightarrow M_{(s)} \quad (1)$$

It follows, that a counter reaction must occur at the anode to maintain electrical neutrality and balance the charge transfer. Here a species is oxidised by the loss of electrons to the electrode. In most electroplating situations, water is decomposed at the anode (2)

$$2\,H_2O \rightarrow O_2 + 4H^+ + 4e^- \quad (2)$$

Although these reactions represent some of the primary reactions, a number of other cathodic and anodic electrode reactions can occur at the electrodes. Only in few cases is the cathodic discharge of a certain metal ion the only cathode process taking place. Other metal ions and hydrogen are often discharged simultaneously.

The process of metal deposition is much more complex however though it may appear simple from these reaction equations. This is because it consists of several partial processes. Furthermore, the metal deposition depends on a number of variables connected with the electrolysis conditions. These are of great significance for the properties of the deposited metals.

Electrode Potentials

When a pure metal is immersed into a solution containing ions of that metal, an equilibrium is set up between the tendency for the metal to dissolve and enter the solution, to the opposing tendency for the ions to lose their charge and deposit on the metal substrate (3)

$$M_{(s)} \underset{v_c}{\overset{v_a}{\Leftrightarrow}} M^{x+}_{(aq)} + xe^- \quad (3)$$

It is represented as M/M^{+2} (the slash represents the boundary between reacting phases; the metal and the metal ions in solution), this compact notation is used to express half-cell reactions. In the absence of an external voltage, an equilibrium between the two reaction processes will quickly result. Such an electrode will adopt a potential difference with respect to the solution whose value is a function of the position of equilibrium. When all the equilibrium components of a half-cell are in their standard states of unit

activity, the electrode is said to be a standard electrode and to adopt its standard potential. When considering the overall chemical reaction taking place in an electrochemical cell, the cell will be made up of two independent half-reactions. For reference, the standard electrode potentials are all relative to the standard electrode potential for hydrogen evolution (4). The potential for this reaction is taken as 0.00 V.

$$H_2 \Leftrightarrow 2H^+ + 2e^- \quad (4)$$

Such reference electrodes are made up of phases having constant composition. With a constant composition, its potential will remain fixed, and changes in the cell will be solely responsible by the working electrode, allowing a better study of potential.

The metals then form a series according to their electrode potentials. Those elements which possess the greatest negative potentials, will have the greatest tendency for their ions to pass into solution (Basic Metal). Those having the greatest positive potentials tend to be inert (Noble Metal).

Electrode Reactions During Electrodeposition

An overall electrode reaction is composed of a series of steps that cause the conversion of the dissolved oxidised species to a reduced form. In general, the current (electron reaction rate) is governed by the rates of processes such as (a) Electron transfer at the electrode surface, (b) Mass transfer of oxidised species from the bulk solution to the electrode surface, and (c) Other processes include chemical reactions preceding or following the electron transfer and other surface reactions, such as adsorption or crytallisation (electrodeposition). Information about an electrode reaction is often gained by determining current as a function of potential (i-E curves).

Electron Processes

When a pure metal is immersed in a solution containing ions of that metal, a dynamic equilibrium between the anodic and cathodic processes is established. An accurate kinetic picture of this dynamic process (3) is now considered. v_a is the rate of the ionisation (dissolution) or anodic process while v_c represents the rate of the discharge or the cathodic process. The rates for these processes may be expressed as shown in equations (5) and (6), where k_a and k_c are corresponding rate constants and $[M^{n+}]$ is the concentration of metal ions (strictly the value at the electrode surface).

$$v_a = k_a e^{-\Delta G_a^* / RT} \quad (5)$$

$$v_c = k_c \left[M^{n+} \right] e^{-\Delta G_c^* / RT} \quad (6)$$

At equilibrium $v_a = v_c$ so that

$$k_a \exp\left[-\frac{\Delta G_a^*}{RT} \right] = k_c \left[M^{n+} \right] \exp\left[-\frac{\Delta G_c^*}{RT} \right] \quad (7)$$

in terms of $\Delta G = \Delta G_c^* - \Delta G_a^*$

$$\exp\left[-\frac{\Delta G}{RT} \right] = \frac{k_c}{k_a} \left[M^{n+} \right] = \exp\left[nF\Delta\phi RT \right] \quad (8)$$

In terms more commonly used this becomes the Nernst equation (9)

$$E = E^{\bullet} + \frac{RT}{nF} \ln\left[M^{n+} \right] \quad (9)$$

If an external potential is now applied, and the potential is made steadily more negative than the equilibrium value, reduction of the metal ions in solution would commence. This departure of the electrode potential (or cell potential) from the equilibrium value upon passage of faradaic current is termed polarisation. Current potential curves, particularly those obtained under steady-state conditions, are sometimes referred to as polarisation curves. The extent of polarisation is measured by the overpotential, n, which is the deviation of the potential from the equilibrium value (10)

$$\eta = E - E_{eq} \quad (10)$$

This theory is also extended to show the dependence of current on potential under various circumstances. For such a situation ΔG_c^* and ΔG_a^* become (11) and(12). Here η serves two functions (a) part of it assists the cathodic process; (b) a fraction retards the anodic process. α is known as the transfer coefficient. In terms of the new activation energies the rates of cathodic and anodic processes now become (13) and (14)

$$\Delta G_c^* = \left(\Delta G_c^\bullet\right)^* + \alpha n F \eta \quad (11)$$

$$\Delta G_a^* = \left(\Delta G_a^\bullet\right)^* - (1-\alpha) n F \eta \quad (12)$$

$$v_c^{'} = k_c \left[M^{n+}\right] \exp\left[-\frac{\{\left(\Delta G_c^\bullet\right)^* + \alpha n F \eta\}}{RT}\right] \quad (13)$$

$$v_a^{'} = k_a \exp\left[-\frac{\{\left(\Delta G_a^\bullet\right)^* - (1-\alpha) n F \eta\}}{RT}\right] \quad (14)$$

Respective rates may be expressed in terms of cathodic and anodic current densities as follows (15) and (16). Thereby (13) and (14) are simplified to yield (17) and (18).

$$v_c^{'} = \frac{i_c}{nF} \quad (15)$$

$$v_a^{'} = \frac{i_a}{nF} \quad (16)$$

$$i_c = i_0 \exp\left[-\frac{\alpha nF\eta}{RT}\right] \quad (17)$$

$$i_a = i_0 \exp\left[\frac{(1-\alpha)nF\eta}{RT}\right] \quad (18)$$

i_0 is the exchange current density and is a very important kinetic characteristic of an electron transfer process. At dynamic equilibrium at the surface of the working electrode, the reduction of O and the oxidation of R are both occurring, but the processes are of equal rate (19)

$$I_c = I_a = I_o \quad (19)$$

Therefore the net cathodic current density $i = i_c - i_a$ is given by (20), which is known as the Butler-Volmer equation. When electrochemical reactions involving more than one electron are considered, it is usual to replace α by αc and to replace $(1-\alpha)$ by α_a since $\alpha_c + \alpha_a \neq 1$ except for n=1, (21)

$$i = i_0\left\{\exp\left[-\frac{\alpha nF\eta}{RT}\right] - \exp\left[\frac{(1-\alpha)nF\eta}{RT}\right]\right\} \quad (20)$$

$$i = i_0\left\{\exp\left[-\frac{\alpha_c nF\eta}{RT}\right] - \exp\left[\frac{\alpha_a nF\eta}{RT}\right]\right\} \quad (21)$$

This must be regarded as the fundamental equation of electrode kinetics, and it shows the way in which current density varies with exchange current density, overpotential and the transfer coefficients. When a large overpotential is applied towards a cathodic reaction, only the first exponential term in equation (20) is significant, the second becomes very small by comparison. The dependence of cathodic current density on overpotential is therefore given by (22), which is the Tafel equation.

$$\ln i = \ln i_0 - \frac{\alpha n F \eta}{RT} \quad (22)$$

Individual electrode overvoltages, may be determined experimentally by means of the circuit in Fig. 2.2. Here a constant electrolysis current density is maintained by a high-tension battery/series resistance combination to polarize the electrodes. Each electrode in turn is then combined with a reference electrode and the emf values of the two cells successively formed in this way measured via the potentiometer. Since the reference electrode potential is known, the potential of the anode and cathode may be determined at the current density imposed.

However, the measurement of electrode potentials has to be carried out carefully. When current flows, a portion of the cell voltage is spent in meeting solution resistance (IR) drop. The most common form arises from the passage of electric current through an electrolyte solution surrounding the electrode. Such a solution is not of infinite conductivity and shows resistance to the current flow, with the result that an ohmic (IR) drop in potential occurs between the working electrodes. This effect may be reduced by protecting the reference electrode from the working solution by enclosing the former in a fine glass capillary, the open end of which is brought as close to the surface of the electrode as possible. The optimum position is a matter of experiment, this largely removes the IR contribution to the measured overpotential.

Mass Transport

In considering electron-exchange reactions at electrodes, the layer of solution very close to the electrode surface comes under scrutiny. When conditions do exist or are imposed so that electron transfer may take place between the electrode material and an electroactive solute material, current flows through the electrode, through the external circuit and through the complimentary electrode. In order to sustain a current for a given potential it is necessary for the supply of material at the electrode surface to be sustained and the movement of ions through the solution. Such movement cannot be increased indefinitely and a point must be reached where solute species react with the electrode as fast as they reach it. The current then approaches a limiting point, a saturation level called the *limiting current density*. The term *limiting current density* is used to describe the maximum rate at 100% current efficiency, at which a particular electrode reaction can proceed in the steady state. This rate is determined by the composition and transport properties of the electrolyte and by the hydrodynamic condition at the electrode surface. Sometimes for a system, a *limiting current density* is not seen due to its masking by the presence of another reaction at the electrode surface. For instance, if the hydrogen overvoltage on a cathode is lower than the potential for the limiting current, a *limiting current density* plateau may not be evident.

There are three mechanisms of ionic mass transfer, (a) electromigration of anions and cations caused by the applied potential gradient between the electrodes, (b) diffusion, caused by the concentration gradient of the metal ions, and (c) convection due to fluid mixing usually by thermal and mechanical stirring effects. Mass transfer to an electrode is governed by the Nernst-Planck equation, written for one dimensional mass transfer along the x-axis (23), where $J_i(x)$ is the flux of species i (mol sec^{-1} cm^{-2}) at a distance x from the surface. The three terms on the right-hand side represent the contributions of diffusion, migration and convection, respectively to the flux.

$$J_i(x) = -D_i \frac{\partial C_i(x)}{\partial x} - \frac{z_i F}{RT} D_i C_i \frac{\partial \phi(x)}{\partial x} + C_i v(x) \quad (23)$$

Steady State I-E Curves

The electron and mass transport steps have been considered in isolation, although it was recognized that the former increases with overpotential (21), while the maximum rate of the mass transport step depends only on the bulk concentration of the electroactive species and the mass transport regime.

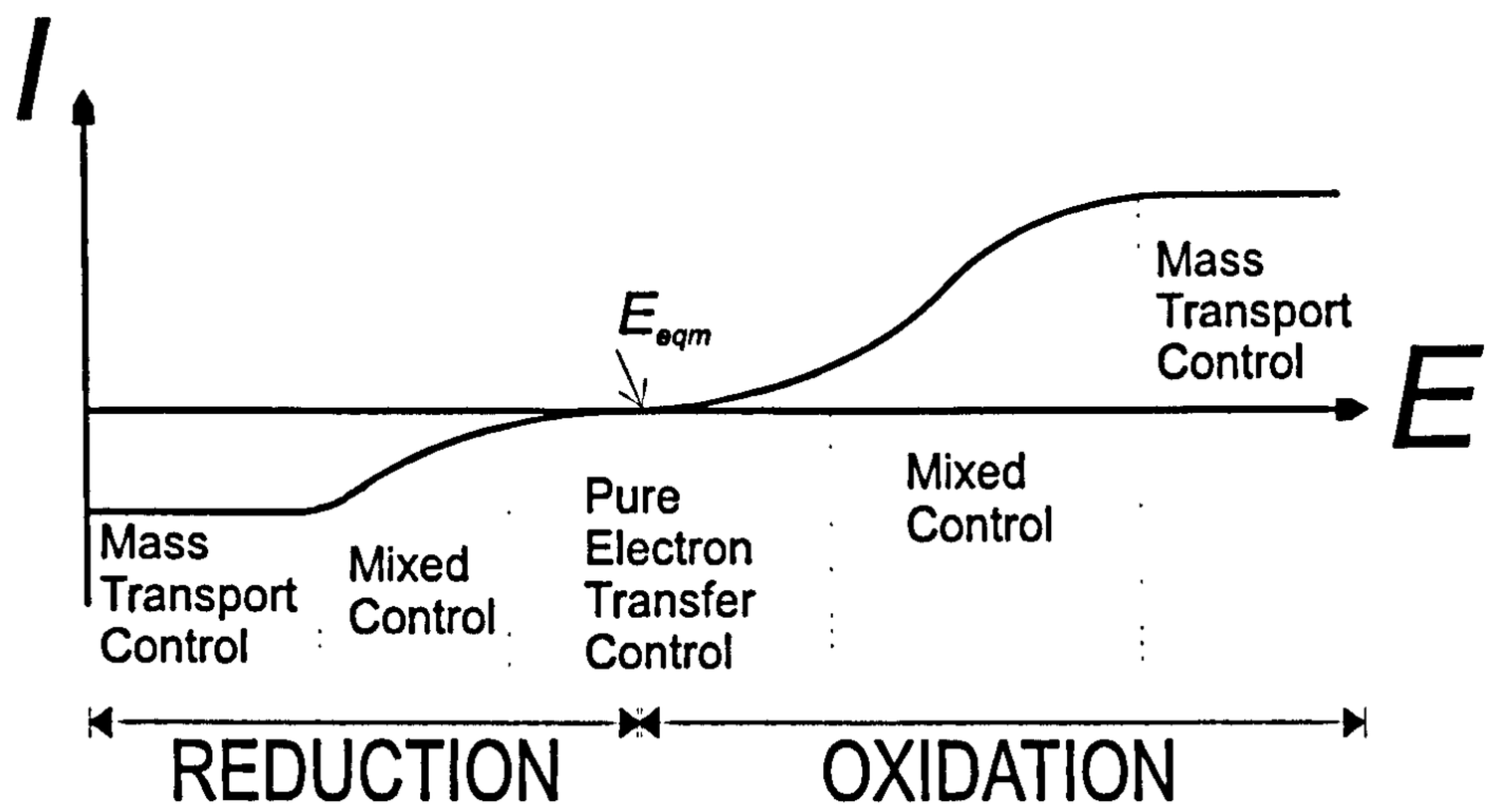

Figure 2.3 "A typical I-E profile for an electron transfer reaction"

To show how the processes interact with each other, a steady state I-E curve is considered. It is very characteristic of potential - current density profiles (Fig 2.3) of numerous electron transfer reactions, where upon increasing the applied potential steadily, the current density is initially very low. The extent of the resulting chemical change at the electrode surface is small and hence the surface concentrations of oxidised and reduced species are not significantly different from the bulk concentrations. In this region, mass transport conditions will have a negligible effect on the experimental current or surface

concentrations; it is under these conditions that the current is solely determined by the rate of electron transfer and equation (20) applies. As the applied potential is increased further, an intermediate region is reached where there is mixed control of the current by mass transfer and electron transfer steps, where mass transport is essential to maintain a constant surface concentration, it is also sensitive to overpotential. With a further increase in applied potential we reach a second limiting region, corresponding to an overpotential where electron transfer is very fast and mass transport is the sole rate determining step. Now the surface concentration of electroactive species will be effectively zero - only for a deposition reaction (i.e. as soon as the species reaches the surface, it undergoes electron transfer). The measured current is independent of overpotential, but is very sensitive to any changes in stirring or agitation.

Hydrogen Evolution & Influence On Metal Deposition

The deposition of hydrogen is of particular importance in electroplating technology [15]. Cathodic metal deposition is often accompanied by simultaneous hydrogen evolution. In principle, the situation is the same in the codeposition of metals and hydrogen as in the discharge of two metal ions. During the cathodic electrodeposition of metals from aqueous solutions, three main types of reactions can occur, metal deposition (24), metal ion reduction (25) and hydrogen evolution (26).

$$M^{n+} + ne^- \rightarrow M_{(s)} \quad (24)$$

$$M^{n+} + ne^- \rightarrow M^{(n-1)+} \quad (25)$$

$$2H^+ + 2e^- \rightarrow H_2 \ (Acid\ Media) \quad or \quad 2H_2O + 2e^- \rightarrow H_2 + 2OH^- \ (Alkali) \quad (26)$$

Hydrogen evolution competes with metal deposition if the deposition potential is close to that of hydrogen. When hydrogen is evolved, the resulting rise in pH in the diffusion layer may cause precipitation of the metal hydroxide and

its inclusion in the deposit where it may cause brittleness, internal stress or roughness. When hydrogen and metal are codeposited, the current efficiencies depend on the relative slopes of their current potential curves. Usually metal current efficiencies decrease as the current increases, but for some metals, the slope of the metal deposition curve is greater than that for hydrogen, in this case the higher the current density the greater the current efficiency.

The dynamic equilibrium potential for hydrogen discharge is 0.0V, the fact that electronegative metals can be electrodeposited at all derives from the fact that hydrogen has a large overpotential (upto 1.0V), that is, it actually deposits at much more negative potentials than the thermodynamic value, because of other rate controlling steps in the discharge process. Such metals include zinc (E = - 0.76). The value of the hydrogen overpotential (η) depends on several factors (a) solution pH (b) current density (c) the metal concerned, defined by its exchange current density i_0.

The essential stages of hydrogen discharge [16] and gas evolution at the cathode are firstly, diffusion of H_3O^+ ions from the bulk of solution to the edge of the diffusion layer. Then the H_3O^+ ions are transferred across the layer, desolvated and partially discharged at the electrode surface, expressed overall as (27)

$$M + H_3O^+ + e^- \rightarrow M - H + H_2O \quad (27)$$

The H atom now absorbed onto the electrode surface then combines with another H atom in the adsorbed state to form adsorbed H_2 molecules, in one of two possible ways (28) and (29). This is followed by the desorption of the adsorbed hydrogen molecules as bubbles and the diffusion of the bubbles and evolution of gas from the electrode surface. The generation of hydrogen on the cathode surface is substantially dependent upon the identity and nature of the surface itself. The general conclusion is that adsorbed hydrogen is higher for high current density, lower temperature and lower pH.

$$M-H+M-H \rightarrow 2M+H_2 \quad (28)$$

$$H_3O^+ + M-H+e^- \rightarrow M-H_2+H_2O \quad (29)$$

Deposition Process

In aqueous solutions, metal ions are present as either hydrated ions or complex ions. Hydrated cations have only water molecules attached to them. A salt composed of several ions, e.g. fluoborate and pyrophosphate, when dissolved in water, will form a complex ion when it becomes coupled with metal ions. Electrolytes in which the metal ion is bound in a complex, predominate for metal deposition in electroplating technology. This is because two different metals can be deposited from them even though their standard equilibrium potentials are so far apart. In a simple salt solution, simultaneous discharge of two metal ions whose reduction potentials are far apart, is nearly impossible. For the electrodeposition of a binary alloy, the transition from the hydrate to the complex bond, both deposition potentials for the respective metals are displaced in the direction of less noble values. Most often the more noble metal according to the electrochemical series is subject to a stronger displacement of the deposition potential towards less noble values than the metal which is less noble according to the series. Now, under these electrolytic conditions, an intersection of the two potential - current density curves for the two metals takes place.

As the ions capable of being deposited arrive at the cathode, they enter the diffusion layer, across which there is a concentration gradient from the surface to the edge of the layer. The diffusion layer is dependent on the electrode configuration, temperature, stirring, current density and electrolyte composition. The thickness of the layer, δ, has a magnitude of the order of 0.05cm under static conditions, which becomes reduced to the region of 0.001cm with rapid stirring. The field strength in the diffusion layer is not

sufficient enough to dispossess the metal ion of its ion complex. Once the metal ion complex passes though this diffuse part of the fixed double layer, it enters the fixed double layer, termed the Helmholtz double layer (0.01 -0.001 microns). The field strength here is so high that the metal ion is released from the complex. Once the electron transfer is complete, then the reduced metal species diffuses along the cathode surface until it is incorporated into the crystal lattice of the cathode. Crystal growth then proceeds by 'repeatable steps', referred to as active sites or growth areas.

Co-Deposition of Metals

The position and trend of the potential-current density curves of individual metals is a very important consideration when trying to choose and accurately control the desired composition of the depositing alloy. Fig 2.4 illustrates two possible schemes which are typical cases for the electrodeposition of two simultaneously deposited metals A and B. The figure shows two extreme cases, one mass transfer controlled and the other kinetically controlled.

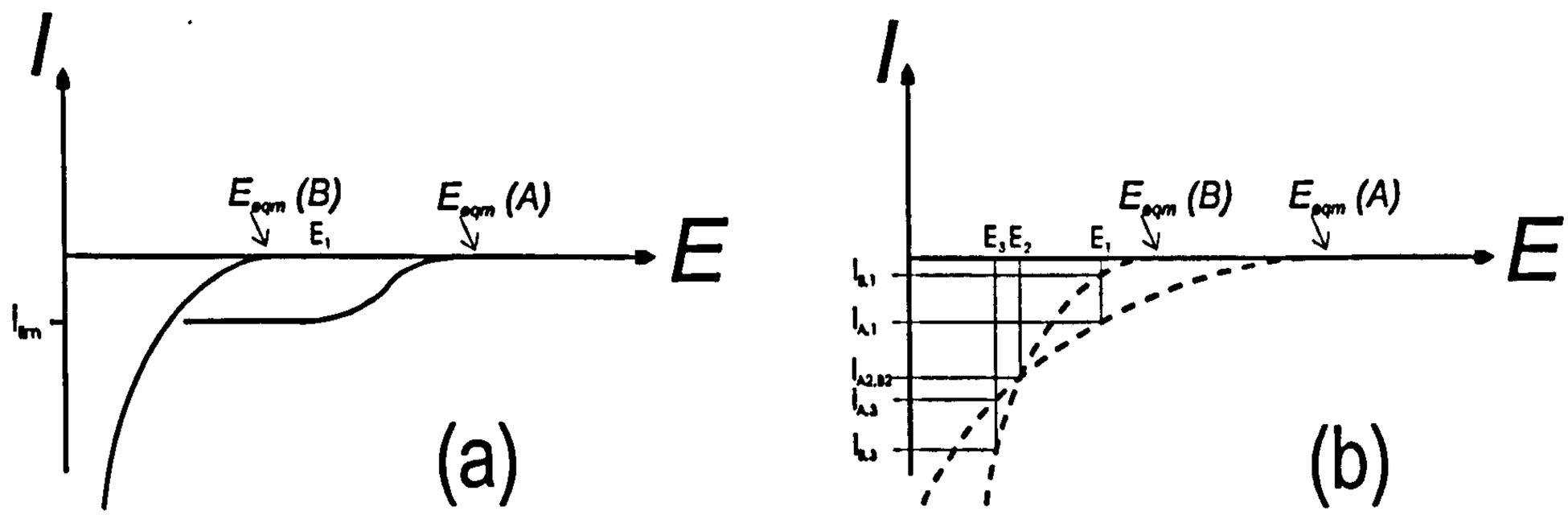

Figure 2.4 "Deposition mechanisms"

Fig 2.4(a) represents the most desirable scheme for the simultaneous deposition of two metals, where one has reached the limiting current density, as it allows greater control of the chosen alloy composition. From the rest potential a negative potential is imposed and reduction of the more noble metal A will begin and increase in rate as the potential is increased. With a further increase in overpotential the deposition potential of metal B is

obtained. At the potential E_1, the limiting current density i_{lim} of the more noble metal A is reached and a limiting current plateau is formed. The current for metal B continues to increase with increasing potential. Because metal A is mass transport controlled but B is kinetically controlled, the current density for A remains constant as the potential is further increased, while the current density for metal B never reaches a limiting condition. The alloy composition is easily determined from the partial currents of metals A and B (30), where X_A is the content of metal A in the alloy and i_A is equal to the limiting current of A.

$$X_A = \frac{i_A}{i_A + i_B} \quad (30)$$

In the second scheme, A as well as B are kinetically controlled and both current densities are variable, making alloy predictions harder to control. At the potential E_1 the partial current densities are $i_{A,1}$ and $i_{B,1}$ ($i_{A,1} > i_{B,1}$). At the potential E2 the partial current densities are equal and thus the current efficiency for both A and B is 50%. At the potential E3 the partial current density is $i_{B,3} > i_{A,3}$. With such a curve trend, the partial current density i_B increases more rapidly with increasing current density than does i_A.

For an accurate prediction of alloy composition at chosen plating potentials, the current efficiencies for metals A and B must be known at each plating potential. In practice, various values for the current efficiency may be found depending on the relative positions of the potential - current density curves. Ultimately, such a situation makes the realisation of plating an alloy with a desired composition (± 0.1%), very difficult.

The above considerations apply to the deposition of alloys only when the cathode potential-current density curves of the individual metals do not interact and modify each other as a consequence of the simultaneous discharge. This is rarely found to be the case however. In electrolytic crystallization of alloys, the discharge of the more noble metal can take place

at less noble cathode potentials than that for the discharge of the noble metal alone. Conversely, the discharge of the less noble metal can take place at a much more noble cathode potential than when it is deposited alone. With given electrolyte composition and working conditions, the position of the cathode potential-current density curves for the alloys relative to those for the curves of the separate metals, depends on the composition and the electrochemical properties of the alloy to be deposited. Under certain circumstances, the less noble metal, as judged by the cathode potential-current density curve for single deposition, may behave as the more noble metal during simultaneous discharge of two metal ions and may be deposited preferentially.

Current Investigations

Electrodeposition, is currently used to manufacture magnetic, wear and corrosion resistant thin films. There have been prior attempts to fabricate shape memory thin films by electrodeposition by J.Frimpong et al [17]. They produced a Cu-Zn alloy which displayed shape memory effects during simple bending tests. However, the shape memory experiments were not entirely systematic which led to several contradictions and ambiguities: (1) The alloy composition under test was 51% Cu - 49% Zn. This composition lies outside the regime where shape memory behavior can be expected [18]. (2) It is well known that microstructure of electrodeposited alloys are different from those obtained metallurgically. However, since the microstructure of the alloy was not determined, no comparison of shape memory effect between these two methods can be made. (3) There was no direct evidence to prove that the alloy switched between martensitic and austenitic phases. Therefore, it remains unclear if electrodeposited and metallurgically prepared alloys undergo exactly the same kind of phase transformation as observed in those prepared by metallurgical means.

REFERENCES

1. J.W.Kim, E.S.Lee, T.J.Cho and Y.G.Kim, Journal of Materials Sci. Letters, Vol 9, 1990, p.463.
2. S.Miyazaki and K.Otsuka, ISIJ Int., Vol 29, 1989, p.353.
3. K.Adachi, K.Shoji and Y.Hamada, ISIJ Int., Vol 29, 1989, p.378.
4. M.H.Wu, 'Engineering Aspects of Shape Memory Alloys', (ed. T.W.Duerig et al.)., p.69, 1990, London, Butterworth-Heinemann.
5. R.Elst, J.Van Humbeeck, M.Meeus and L.Delaey, Z.Metallkd., Vol 77, 1986, p.421.
6. K.Adachi, J.Perkins and C.M.Wayman, Acta Metall., Vol 36, 1988, p.1343.
7. S.Eucken, P.Donner and E.Hornbogen, Mater. Sci. Eng., Vol 98, 1988, p.469.
8. N.Nakanishi, and T.Shigematsu, 'Sintering '87', (ed. S.Somiya *et al.*), Vol 1, p.605, 1988, Barking, Essex, Elsevier Applied Science.
9. J.S.Benjamin, Metall. Trans., Vol 1, 1970, p.2943.
10. J.S.Benjamin, 'New Materials by mechanical alloying techniques', (ed. E.Arzt and L.Schultz), 3, 1989.
11. L.Lu, M.O.Lai and S.Zhang, Materials Science and Technology , Vol 10, 1994, p.319.
12. C.Suryanarayana, R.Sundaresan and F.H.Froes, Mater. Sci. Eng., A153, 1992, p.648.
13. W.R.Grove, Philos. Trans.Faraday Soc., p.87, 1852.
14. I.Langmuir, General Electric Rev. 26, 731 (1923).
15. C.J.Raub, Plating & Surface Finishing, Vol 80, 1993, p.30.
16. J.O'M. Bockris and A.K.N.Reddy, Modern Electrochemistry, Plenum, New York (1970).
17. J.Frimpong, C.H.Sonu, T.R.Hymer and T.J.O'Keefe, Proc. of SPIE, p.362, Washington, USA, 1993.
18. M.Hanson and K.Anderko, "Constition of Binary Alloys, Metallurgy and Metallurgical Engineering Series (McGraw-Hill Book Company, NY) p.649 (1958).

CHAPTER 3

- PLATING BATH -

3.0 BRASS PLATING BATHS

Brass has been plated for well over 100 years and although many alternative types of plating baths have been investigated, electrodeposition from cyanide solutions remains the only established industrial practice. This is because deposits are bright, adherent and of good colour. Importantly, they have compositions which can be controlled by the deposition potential. Phases ranging from the α solid-solution to the ε-phase can be produced, although there is debate about whether the compositions of these phases are the same as those found in brasses made by metallurgical processes [1, 2].

Even though brass is commercially electrodeposited from cyanide baths as they satisfy most of the important requirements of a plating solution, the toxicity of cyanide has provided the incentive to choose an alternative electrolyte for this study. In addition, cyanide baths decompose during operation because they are unstable, which necessitates frequent addition of cyanide. Other problems relate to low current efficiency, low applied current density and sluggish mass transport.

A fairly voluminous literature has been growing up on the deposition of brass from non-cyanide plating baths. The majority of reports on non-cyanide electrolytes, claim these electrolytes to be less stable than cyanide baths, and that the deposits obtained from them are difficult to control and reproduce. For example, there have been some suggestions by Brenner [3], that deposits from a glycerol - zincate bath containing both copper and zinc may not be alloyed together, but exist separately, either as metals or in an oxidised state. The more successful electrolyte alternatives consist of thiocyanate [4], glycerol [5, 6, 7], pyrophosphate [8, 9, 10], glycerate - zincate [11], alkaline tartrate [12, 13, 14], thiosulfate [15, 16] and ethanolamine [17]. Among the other baths that have been investigated, include ethylene-diamine, tartaric acid-glycerol, oxalate and tartrate-zincate.

Although a number of non-cyanide brass plating solutions have been studied and proposed, none of them have had commercial application. The most promising non-cyanide bath of them all is the pyrophosphate bath. In fact, this electrolyte has been commercialised for copper plating in the electronic industry for the fabrication of through the hole printed wiring boards [18]. A pyrophosphate plating bath offers a number of desirable features when compared with the cyanide solution. It has good throwing power, the pyrophosphate ion forms complexes with a number of metals, it is non-corrosive, non-toxic, and of high solubility and stability, easier bath control and maintenance, and a wider range of alloy compositions. Brass deposits containing 40 – 99% of copper [19], have been produced from pyrophosphate electrolytes containing copper and zinc. The deposits have excellent physical properties, being adherent, smooth, fine grained, non-porous and corrosion resistant [20].

3.1 THE PYROPHOSPHATE BATH

The first scientific study of metal deposition from a pyrophosphate bath was investigated as early as 1847 by Roseleur [21]. However, the development of a commercial copper pyrophosphate solution had to wait until 1941 [22, 23]. The electrodeposition of brass from a pyrophosphate bath was first touched on by M de Kay Thompson [12] in 1912. The first serious research into brass plating from a pyrophosphate bath was later under taken by Rama Char [8, 9, 19, 24], Persantseva and Titov, and consequently there have followed more recent investigations [25, 26]. However, there are considerable disagreements between their results, which warrants a more critical and comprehensive investigation into this process.

The pyrophosphate plating bath used in this study operates at pH 8.4. Between pH 8-9, the solution is highly buffered and there is no chemical breakdown of the constituents such as the hydrolysis of pyrophosphate to

orthophosphate or formation of precipitates. There are several claims as to the best operating pH range. The literature generally refers to a pH range of between 8.2-8.8 [27, 28]. However, there are quite different claims, proposing the optimum pH to be 9.5 and 9.7 [8, 25], while others consider it more desirable to increase the pH to 10.0 – 10.5 in order to increase the throwing power and efficiency of the plating solution [29]. Consequently, outside the pH range of 8-9, it is believed that a low pH will precipitate copper and zinc pyrophosphate, while a high pH will cause precipitation of hydroxides. Again, some literature claims no breakdown of products even at a pH approaching 11.0.

The solution must contain an excess of complexant, namely potassium pyrophosphate for successful complexation of the metallic ions and to increase electrical conductivity. Potassium pyrophosphate is preferred to the sodium pyrophosphate salt used in some baths, as it is more soluble, and a potassium solution has a higher electrical conductivity. In addition, the limited solubility of the sodium salt restricts the range of metal concentrations which can be used in the plating solutions.

For optimum plating, the weight ratio of pyrophosphate ($P_2O_7^{4-}$) to metal ions (M^{2+}) is extremely important. Literature suggests that this ratio should be kept in the range of 7:1 to 8:1. Ratios of 8.5:1 or higher, promote the breakdown of pyrophosphate to form orthophosphate. The $P_2O_7^{4-}$: M^{2+} ratio has also been found to exert a much greater influence on the appearance of the deposit than the overall metal content of the solution [29]; for example, if the ratio falls below 7:1 the bath becomes unstable and rough surfaced deposits would result. However, there are discrepancies in the literature, indeed work by Rama Char et al proposed an optimum $P_2O_7^{4-}$: M^{2+} ratio of 2.2:1 [8].

Nitrate ions are also added to the electrolyte as they increase the limiting current density by acting as a proton acceptor (Equations 1, 2, 3). The cathodic current increases linearly with respect to the amount of KNO_3 added [30]. Based on this result, it is proposed that the main function of NO_3^- is to

maintain a constant level of reducible species other than $Cu(P_2O_7)_2^{6-}$ at the cathode [27, 31]. This will prevent the potential of the cathode from drifting to a more negative value at a given current density. This explanation is consistent with NO_2^- being found in a used process solution [32].

$$NO_3^- + 2H^+ + 2e^- \rightarrow NO_2^- + H_2O \quad (1)$$

$$NO_2^- + 8H^+ + 6e^- \rightarrow NH_4^+ + 2H_2O \quad (2)$$

$$\underline{OVERALL:} \quad NO_3^- + 10H^+ + 8e^- \Leftrightarrow NH_4^+ + 3H_2O \quad (3)$$

Other factors considered were (1) the concentrations of the metal ions; attempts to bring the deposition potentials of copper and zinc closer by the use of addition agents to favour co-deposition has met with little success. However, at very low copper concentrations of the solution, the copper potential approaches that of zinc [8]. (2) The plating baths can be operated up to 60° C, an increase in temperature was reported to increase the current efficiency of the system. Temperatures greater than 60° C can lead to the breakdown of bath constituents. (3) The baths must be very well agitated for good deposits to develop.

The principal pyrophosphate electrolyte used in this study for brass deposition comprised of 0.01M $Cu_2P_2O_7$, 0.09M $Zn_2P_2O_7$, 0.23M $K_4P_2O_7$, and 0.12M KNO_3, giving a $P_2O_7^{4-}$: M^{2+} ratio of 7.5:1. The pH was 8.4. In order to maintain good electrolyte agitation, all deposits were plated at a rotating cylinder cathode.

REFERENCES

1. E.Raub and D.Krause, Z.Elektrochem, Vol.50, p.91 (1944).
2. T.Banerjee and A.J.Allmond, Trans. Faraday Soc. Vol.44, p.819, (1948).
3. A.Brenner, Electrodeposition of Alloys, Volume I, Academic Press, New York, p.462 (1963).
4. N.Thon and J.Pinella, J.Chem. Phys, Vol.28, p.651 (1931).
5. G.L.Schnable, J.Electrochem. Soc. Vol.108, p.964 (1966).
6. S.K.Ray, H.F.K.Udupa and B.B.Dey, J.Sci. Ind. Res., India, Chem. Abstr. Vol.50, 7623d (1955).
7. A.I.Stabrovski, J.Appl. Cherm U.S.S.R, Vol.25, P.1031 (1952).
8. V.Sree and T.L.Rama Char, J.Sci. Ind. Res., India, Vol.16A, p.325, (1957)
9. T.L.Rama Char, Electroplating Metal Finishing, Vol.10, p.391 (1957).
10. V.Sree and T.L.Rama Char, Symp. Electrodeposition Met. Fin., Proc. Karaikudi, India, p.39, (1957).
11. S.K.Ray, H.F.K.Udupa and B.B.Dey, J.Sci. Ind. Res., India, Vol.14B, No.12, p.652, (1955).
12. M.DE.K.Thompson, Met. And Chem. Eng. V10, p.458 (1912).
13. T.Banerjee and S.K.Ray, Indian Patent 45,565 (1952).
14. S.K.Ray and T.Banerjee,J. Sci. Ind. Research (India) 12B, No.1, p.438, (1953).
15. D.C.Gernes, G.A.Lorenz and G.H.Montillon, Trans. Electrochem. Soc. 77, p.177 (1940).
16. D.C.Gernes and G.H.Montillon, Trans. Electrochem. Soc. 81, p.231 (1942).
17. R.Sadagopachari, N.B.Shivaraman and T.L.Rama Char, Current Sci. (India) Vol.20, p.154 (1951).
18. D.A.Luke, Trans. Inst. Metal Finishing, Vol.47, p.36 (1969).
19. V.Sree and T.L.Rama Char, Electroplating and Metal Finishing, Vol 12, p.326, 1959.
20. T.L.Rama Char, Electroplating and Metal Finishing, Vol.. p.347 (1957).

21. A.Roseleur, Manipulations Hydroplastiques-Guide Practique du Doreur, de L'Argenteur et de Galvanoplaste, 1st ed., Roseleur, Paris, 1855.
22. J.E.Stareck, U.S Patent 2,081,121, (1937).
23. J.E.Stareck, U.S Patent 2,250,556, (1941).
24. G.R.Nagaraj and T.L.Rama Char, Proc. 41st Indian Sci. Congress Bangalore Part 3, p.103, (1954).
25. Y.Fujiwara and H.Enomoto, Plating and Surface Finishing, p.52 (1993)
26. T.Vagramyan, J.Leach and J.R.Moon, Electrochim. Acta, Vol.24, p.231 (1979)
27. F.A.Lowenheim, Modern Electroplating, Technical Reference Publications Ltd., Arrowsmith, Bristol, UK, 1955.
28. C.A.Hamilton Jr., Plating & Surface Finishing, Vol 82 Prt 8, p 48 (1995).
29. D.Povey and U.F.Marx, A pilot investigation, Wilmot Breeden Laboratories, Solihull, England. p.70.
30. T.M.Tam and R.Taylor, J.Electrochemical Society, Vol 133, No 6, p.1101 (1986).
31. F.Passel, Plating, Vol 46, p 628 (1959).
32. T.M.Tam and G.A.Fung, J.Electrochemical Society, Vol 130, No 4, p.874 (1983).

CHAPTER 4

- EXPERIMENTAL -

4.0 ELECTROLYTE

Cu-Zn alloys were electrodeposited from a pyrophosphate electrolyte whereby copper pyrophosphate and zinc pyrophosphate salts were dissolved in an excess of potassium pyrophosphate and potassium nitrate. With the exception of zinc pyrophosphate, all of the other plating bath constituents were supplied by Aldrich Chemical Suppliers.

Zinc pyrophosphate was obtained by adding a 0.5M $ZnSO_4$ (Aldrich > 99.99%) saturated solution to a 0.252M $K_4P_2O_7$ (Aldrich > 97%) saturated solution, both maintained at 40 °C. Upon contact, zinc pyrophosphate immediately precipitated out and was collected by suction filtration. The precipitate was then dried in a oven for 3 days and collected as a fine white powder. The zinc, phosphorus, potassium and sulfur contents were then analysed by atomic absorption spectroscopy (AAS) to assess purity.

The Cu-Zn alloys were deposited from a pyrophosphate electrolyte, that was produced by dissolving 0.23 moles of $K_4P_2O_7$ (Aldrich > 97%) in 800ml of H_2O. H_2O was obtained from a Milli-U10 ® water purification system (Millipore Corporation). To aid dissolution, the solution was constantly stirred by means of a magnetic stirring unit. Once dissolved, 0.01moles of $Cu_2P_2O_7.H_2O$ (Aldrich > 99.9%), 0.09 moles of $Zn_2P_2O_7$ (> 96.971%) and 0.12 moles of KNO_3 (Aldrich > 99%) were added to the solution ($P_2O_7^{4-}$:M^{2+} ratio 7.5:1). The solution was then made up to 1 litre with H_2O. The pH of the electrolyte was adjusted with 0.03 moles of $H_4P_2O_7$ (Aldrich > 99%) to pH 8.4 using a HANNA HI 8424 microcomputer pH meter and BDH pH electrode probe (309/1050/03).

Zinc pyrophosphate and copper pyrophosphate electrolytes were made by the same method outlined above, but with the omission of the corresponding metal ion pyrophosphate salt and a reduction in the addition of $K_4P_2O_7$, to

maintain the weight ratio of $P_2O_7^{4-}$ to M^{2+} at 7.5. All the plating solution compositions are shown in Appendix .A .

4.1 ELECTRODEPOSITION

4.1.1 Apparatus

The electrochemical cell employed in the plating experiments is shown in Fig 4.1. Thin brass foils were plated onto the rotating cylinder cathode (pre-plated with a copper strike layer) which was maintained at a constant speed for the duration of each experiment. The speeds employed ranged from 500 rpm to 2000rpm, controlled by a variable speed motor. The cathode cylinder was made from stainless steel (diameter 1cm; length 4cm) and polished prior to every experiment with 4000 grade silicon carbide papers. Then the detachable cathode was mounted on the rotation shaft and immersed in the electrolyte. A concentric platinum coated titanium mesh anode was placed at a distance of 3.8 cm from the outer diameter of the cylinder. A saturated calomel reference electrode (SCE) was placed at a distance of 1.8 cm, by means of an extending capillary, as shown in Fig 4.1. The cell was constructed from Perspex with a capacity of holding 800ml of the electrolyte. Plating was always done by direct-current plating using a Sycopel Scanning Ministat Potentiostat.

4.1.2 Procedure

Since Cu-Zn alloys did not adhere well to the stainless steel surface, a thin layer of copper was plated on the surface of the steel prior to the brass. The copper electrolyte used, was prepared by dissolving 0.1 mole of $CuSO_4.5H_2O$ (BDH Analar Grade > 99%) and 1.0 mole of H_2SO_4 (BDH Analar Grade > 98%) in one litre of > 18 Ω purity water. Plating was performed galvanostatically using a dc power supply (Thurlby-Thandar PL 320). A current density of 15.91 mA/cm^2 was employed, and the rotation speed of the cathode was fixed at 1000 rpm. Assuming a 100% current efficiency, plating proceeded for the duration of ten minutes, corresponding to a copper strike

layer of approximately 10 μm thick. Foils were plated up to a thickness of 50 microns with respect to the current efficiency at each plating potential. After

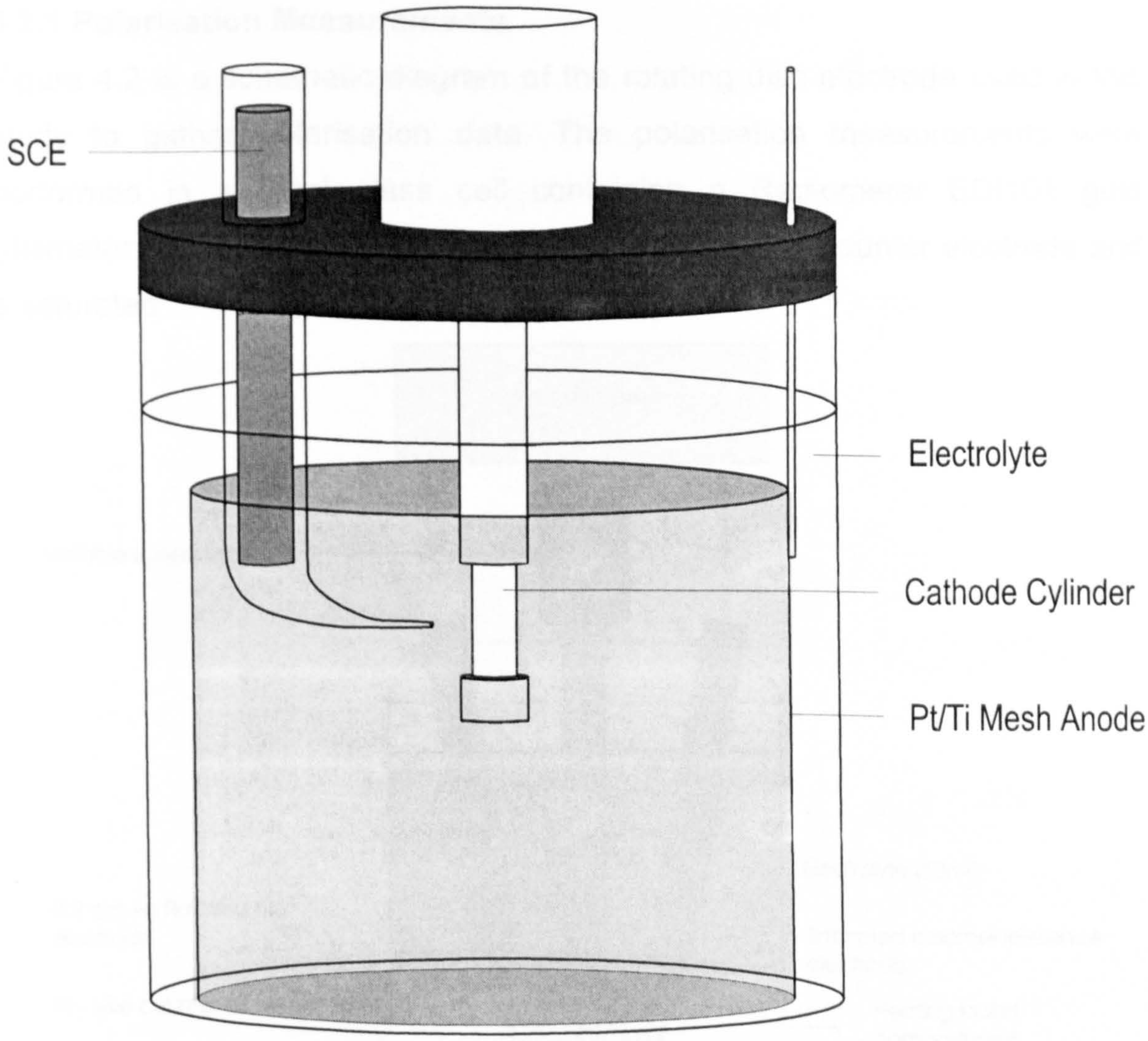

Figure 4.1 "Rotating cylinder cathode"

plating, the cathode was washed with de-ionised water, washed with methanol and air dried. The cathode was then removed from the rotating shaft. The foil was then removed from the cathode by scouring down one side of the cathode and peeling it off. All foils were electrodeposited at room temperature.

4.2 ELECTROCHEMICAL STUDIES

4.2.1 Polarisation Measurements

Figure 4.2 is a schematic diagram of the rotating disc electrode used in this study to gather polarisation data. The polarisation measurements were performed in a 50ml glass cell containing a Radiometer EDI101 gold (diameter 0.2cm) rotating disc electrode, platinum wire counter electrode and a saturated

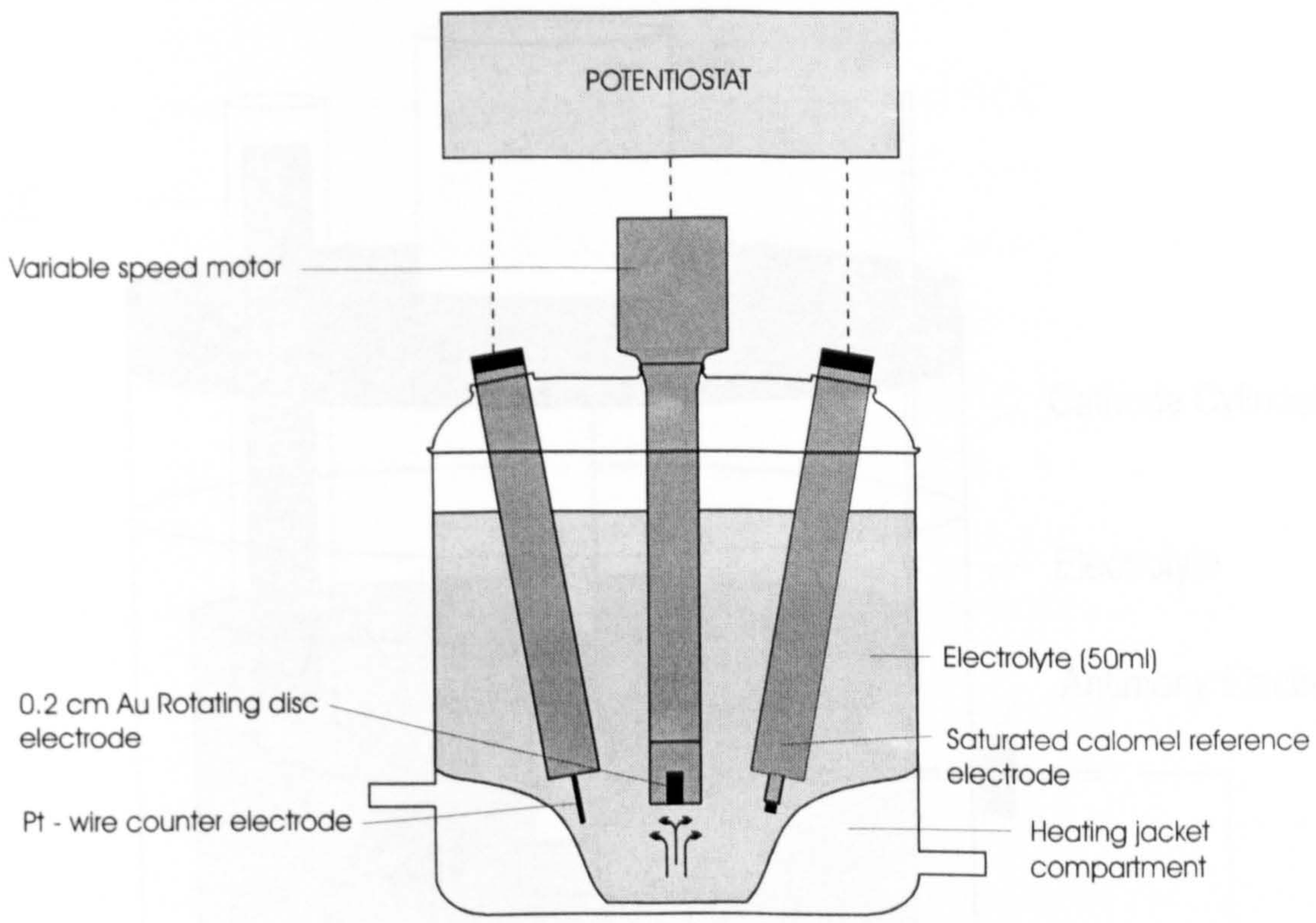

Figure 4.2 "Rotating Gold Disc Electrode"

calomel reference electrode (SCE). The EDI101 is controlled by a speed control unit, the CTV101. Experiments were carried out using a high performance 20V / 1A potentiostat (Radiometer Copenhagen VoltaLab 21 Model PGP201) interfaced to a PC using the VoltaMaster 1 Data Management Program. Cyclic voltammetric analysis was carried out covering a polarisation range of -1700mV to 400mV and scan rates varied between 100 - 500 mV/min.

4.2.2 Monitoring pH Change at the Electrode Surface

The pH of the brass electrolyte is well buffered at 8.4. However, since the pH at the electrode surface can differ significantly from the bulk, an attempt to measure the pH close to the electrode surface was also carried out. This was done by placing antimony electrodes very close to the cathode cylinder (0.072mm) during deposition experiments, allowing the pH of the surface to be monitored with respect to change in plating potential and rotation speed.

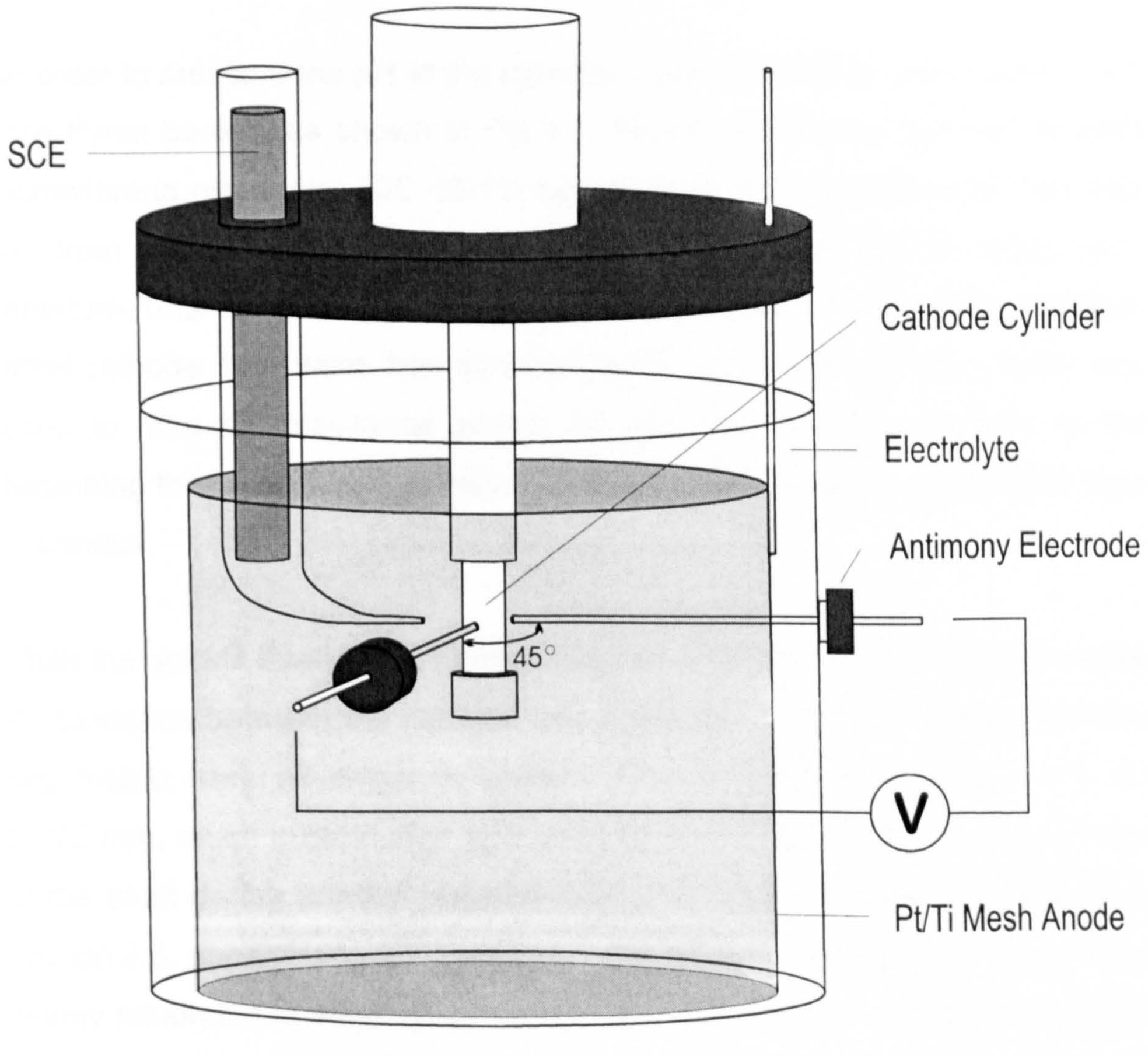

Figure 4.3 "Electrode Surface pH measurement"

The antimony electrodes were prepared [2] by sealing one end of a 2mm diameter glass tube in a bunsen burner. Then small pellets of antimony shot were fed down the glass tube and melted, the antimony formed a plug of approximately 1cm in length at the bottom of the glass tube. When the tube

had cooled, a copper contact wire was attached to the antimony plug by means of silver epoxy resin. The copper wire protruding from the glass tube was anchored with Araldite epoxy resin. The sealed end of the electrodes were then ground down with silicon carbide papers. This exposed an antimony disk of approximately 1mm in diameter to the electrolyte. The antimony electrodes were then calibrated against Fisher Scientific International Buffer Solution Standards, pH 4, 7 and 10. This was carried out by standing them in the standards under vigorous stirring. The pH of the electrode was read after 5 minutes, during the calibration experiments.

In order to measure the pH at the cylinder surface, the RCE was placed in a 1 litre Pyrex beaker, as shown in Fig 4.3. This Pyrex beaker had two Quickfit screwthread glass joint (QC 18/11) apertures at 90° to each other half way up from the bottom. An antimony electrode was then placed within each aperture, until their tips were in contact with the central area of the stainless steel cathode, they were then screwed tightly in position. A digital meter was used to read the resistance across the antimony and the cylinder. In the beginning the resistance was very small because the antimony and steel were in contact.

Then the quickfit thread was slowly loosened, until there was a sharp increase in resistance between the cathode and antimony electrode, showing that the two metals were no longer in contact. This distance was measured to be 0.072 mm, much greater than that used for static electrodes. The movement of the shaft during rotation resulted in such a large tolerance. As detailed in section 4.3, once plating commenced, readings were taken every minute, until twenty minutes had elapsed, by which time the pH had settled to a constant value for each experiment.

4.2.3 Current efficiency Measurements

Current efficiencies were initially determined by integral analysis of the cathodic and anodic currents gathered from the polarisation data for copper and zinc. The area under the cathodic region of the graph was measured, the

size of this area (*I v t*) was a direct measure of the charge passed. The anodic stripping peak area, is the portion of the charge accounting solely for the oxidation of the metallic species. The ratio of the two values were used to determine current efficiency. To cross-check the results obtained from charge integration, current efficiencies for copper, zinc and brass were determined by gravimetric analysis using the RCE. This was carried out by measuring the charge passed during deposition, compared to the maximum theoretical weight that could have been deposited. Samples were weighed to an accuracy of 0.0001g in these experiments.

4.2.4 Nitrate Reduction

The reduction of nitrate to nitrite during eletrodeposition, was followed by spectroscopic measurements made with a Unicam 8700 UV-VIS spectrophotometer. A freshly made copper and zinc pyrophosphate electrolyte employed for 12 hours of a deposition trial, was sampled and analysed at hourly intervals.

Two identical 10mm rectangular glass cells, the reference cell and the sample cell, were filled with 18 Ω purified water, a blank scan was run to determine if the cells were correctly matched so there was no discernible difference in optical density.

Potassium nitrate and potassium nitrite solutions (10 g/L) were each made by dissolving 10 g of compound in 1 litre of 18 Ω purified water. Employing the spectrophotometer, the percentage transmission for each solution was measured by filling the sample cell with solution, then performing a scan over the wavelength range 250 - 500 nm, in steps of 1.0 nm, at a speed of 50 nm/min. From the resulting curves, the wavelength of maximum absorption was evaluated for the nitrate and nitrite species.

A calibration curve was constructed for potassium nitrate by measuring the transmission of solutions containing 4.0, 6.0, 8.0, 10.0, 12.0 and 14.0 g/L of potassium nitrate, at the wavelength of maximum absorption. This was

repeated with solutions of 1.0, 2.0, 3.0, 4.0, 5.0 g/L of potassium nitrite. A linear calibration graph was produced for each. The concentrations of nitrate and nitrite in the plating bath were then read from the graphs by extracting a small electrolyte sample during the deposition of a thin film brass foil and performing a scan.

4.2.5 Modelling of pyrophosphate speciation

The equilibrium concentrations of various pyrophosphate species present in the plating solution was calculated using the computer program MINEQL$^+$ [1]. This is a general purpose program for solving chemical equilibrium problems in aqueous systems [1, 2]. To perform the calculation, the concentration of all metal ions and ligands along with stability constants of any complexes that may be formed were entered into the program. MINEQL$^+$ then solved iteratively the mass balance equations for each metal ion, and then computed the final species distribution. Stability constants for various copper and zinc pyrophosphate and hydroxide complexes were obtained from standard critical compilations [3]. As well as calculating the equilibrium concentrations of these complexes, MINEQL$^+$ also checked for the formation of precipitates. For the solutions used, the precipitation of $Cu_2(P_2O_7)_2$, $Zn_2P_2O_7$, $Cu(OH)_2$ and $Zn(OH)_2$ were considered.

4.3 MATERIAL CHARACTERISATION

4.3.1 X-Ray Diffraction (XRD)

X-ray diffraction was used to determine the phases present in the plated foil. The thin films were examined by both powder X-ray diffraction and straightforward examination of the as-plated foil. Analysis by powder X-ray diffraction employed the use of a Hägg-Guinier focusing camera with monochromatic Cu$K\alpha_1$, radiation (λ = 1.54056Å). Exposure times of 90 minutes at 50kV and 15mA were used. The positions of X-ray reflections were measured and from these, d-spacing and $\sin^2\theta$ values were generated by a computer aided line scanner. Approximate proportions of the various phases

were estimated visually by the scanner from the intensities of the reflections, taking into account the larger scattering power of materials containing heavier metals/elements. For powder analysis, foils were crushed in a mortar and pestle with the addition of potassium chloride as an internal standard.

The second method of analysis was undertaken using a Phillips vertical PW1050 type X-ray diffractometer, set up on CuKα radiation (λ = 1.542Å). This was used to obtain α, β and γ phase spectra of the as-plated electrodeposited foils in order to determine specific peak areas and hence α:β:γ ratios and changes in phase composition with varying brass compositions. For foil analysis, 1cm^2 samples were required. The brass deposits needed to be > 10microns thick to prevent x-rays from penetrating through the brass and interacting with the copper underlayer. Prior to X-ray analysis, the copper underlayer was removed in certain experiments, so the x-ray diffraction patterns of only the Cu-Zn foil could be obtained. Removal of the underlayer was carried out by exposing the copper to 15% nitric acid for 50 seconds, effectively etching away almost entirely the copper.

4.3.2 Scanning Electron Microscopy & EDAX

A Hitachi S-2400 scanning electron microscopy equipped with EDAX was used to check the actual composition of each brass foil. Secondary Electron Imaging (SEI) and Back Scattered Electron Imaging (BEI) modes were used to image the thin foils and to characterise the microstructure. In addition to the EDAX facility, further compositional analysis was also possible using X-ray line scanning.

The samples were prepared by mounting the foil in resin and polishing with silicon carbide papers to a mirror finish. Alternatively, to obtain better information on growth and grain formation, the freshly deposited foils were removed from the RCE then placed in liquid nitrogen and cracked. This had the effect of cleaving the foils, and the cleavage occurred along grain boundaries. They were then mounted onto a SEM examination stub by means of carbon tape.

4.3.3 Transmission Electron Microscopy (TEM)

Use of a transmission electron microscope was employed due to its high resolution power of < 1μm to gather details on crystal lattice arrangements or atomic placements within the foils/phases. For analysis, the brass foils had to be thinned and removed of their entire copper underlay. Metals are generally too hard for ultra thinning. Mechanical thinning and polishing was engaged followed by ion-beam thinning. Several techniques were employed to perfect this; (1) a $3mm^2$ sample cut from a plated foil was glued to a brass block with the copper underlayer showing, it was then polished on a grinders wheel using 0.5 and 0.1 micron diamond pastes at speeds of 0.1 - $20mms^{-1}$. (2) Tripod method; $3mm^2$ of brass foil was glued to a stainless steel block with the copper layer showing, the block was then bolted on to the bottom of a polishing tripod. Each of the tripod's leg lengths was adjustable by means of separate built-on micrometer, once the legs were set to the desired lengths, they were held in position by individual locks. The feet of the tripod were made from PTFE. By this arrangement, the edge of the sample was able to be polished to any angled desired, whereby a very low angle enabled all of the copper to be polished away and produce a very fine brass tip that was almost transparent at the edge. Polishing then preceded as before, using 0.5 - 0.1 micron diamond pastes. (3) The final method employed a 'LogiTech' polishing machine. This method allows a precise level pressure to be applied to the $3mm^2$ diameter sample (glued to the bottom of a stainless steel wheel and set on a polishing bed), evenly removing layers accurately upto 2microns.

Each method was able to produce fine samples, however upon their removal from each grinding apparatus by dissolving the glue which held them, the samples were found to be very fragile and possess several microcracks. The microcracks may have been induced by the polishing techniques or occurred during the removal of the foils from the rotating cylinder cathode. This situation was worsened when the delicate samples were mounted in a standard TEM electrolytic copper specimen support grid ($3mm^2$ diameter 15 um thick) and ion milled overnight to produce an brass edge that would be

less than 2 - 100 nm thick (transparent). Due to the delicate nature of the prepared samples and that several possessed microcracks, many samples were lost or destroyed by ion milling.

Ion milling involved, a collimated beam of energetic positive ions, Ar^+ (inert and heavy), directed at an angle at the alloy surface under vacuum, causing the metallic atoms to be removed by the process of sputtering. The brass sample was bombarded from both sides by the narrow beams of argon ions, and was simultaneously rotated in its own plane about the axis in its centre. The ion beams were at an incident angle of 10° to the surface in order to produce a large area of thinned foil around the perforation that the beam will develop in the sample. The sample once milled was loaded into a microscopy holder and loaded into the TEM for examination.

The TEM column was also employed to produce electron diffraction patterns to reveal the internal structure and degree of crystallinity of the foils. From the high resolution transmission image, an area of the specimen that represented itself to be characteristic of martensitic, was examined by electron diffraction patterns produced in the back focal plane of the objective lens. Enlarged on a screen, this was documented by taking photographs of the regions and phases of interest.

The detection of phase transformations was also undertaken using TEM, as heat treatments were carried out in-situ with the specimens under examination by TEM. Under vacuum, the specimens were heated upto 200°C and their reactions were documented by video recording. The precaution of removing the copper underlayer from the brass samples before heat treatment is essential for the detection of phase transformations. The microstructure of the copper may drive the transformation reaction and influence the microstructure of the resident and newly produced martensite during the in-situ heat treatment of the foil.

4.3.4 Differential Scanning Calorimetry (DSC)

The thermal behaviour of the plated brass foils was monitored by a Mettler Toledo DSC821 module. DSC was employed to provide evidence of a martensitic phase change within the brass below room temperature and also characterise the hysteresis temperature profile.

Specimens were cut from the plated foils by means of an ultrasonic drill. The foil was glued to an aluminum block. A stainless steel hollow o-ring (3mm dia) connected to an ultrasonic drill was then lowered on top of the foil. The drill piece resting on the foil, was covered with distilled water heavily concentrated with tungsten carbide particles. When the drill was switched on, a downward pressure was applied to the drill on top of the foil and hence 3mm^2 diameter circles were cut in the foil by the grinding action of the tungsten carbide particles. The samples were then removed from the aluminum block by dissolving the glue.

The circular brass samples were loaded into an aluminum crucible up to a collective weight of 20mg with respect only to the percentage composition of brass in the sample. The crucibles were then sealed with an aluminum top. The crucible was then placed into the DSC unit. Samples were heated and cooled at a rate of 10 K/min upto 150 °C and down to -150 °C, followed by a re-heat to room temperature. Reverse measurements were also carried out, first cooling then heating. A plot was then extracted from the data showing temperature versus exothermic or endothermic heat change. Samples were also heat treated in-situ, by holding the samples at pre-determined temperature limits. The upper temperature limit was 500 °C, however, these heat treatments could only be undertaken in a normal air atmosphere.

4.3.5 Heat Treatments

Heat treatments not carried out in situ-TEM or DSC, were carried out in a high temperature computer controlled furnace. The brass foils were sandwiched tightly between two quartz slides and placed upon a alumina crucible. The

crucible was then placed in the oven. Experiments were carried out with various times up to a temperature of 500 °C.

REFERENCES

1. MINEQL^{+}: Chemical Equilibrium Management System, Environmental Research Software, Hallowell, Maine (1994).
2. W.D. Scherer and D.C. McAvoy, Comp. Environ. Urban Systems, 16, 1992, p.65.
3. A.E. Martell and R.M. Smith, Critical Stability Constants, Vol. 4-6, Plenum, New York (1976-1989).

CHAPTER 5

- POLARISATION DATA -

5.0 POLARISATION MEASUREMENTS

Polarisation data for Cu and Zn electroreduction at a gold rotating disc electrode are shown in Fig 5.1. The rotation speed of the gold RDE is 1000 rpm and the scan rate is 0.3 V s^{-1}. The electrode potential was cycled from 0.20 V in an electronegative direction and then back. For copper reduction, the lower limit of the scan is - 1.1 V, whereas for the zinc deposition it is - 1.5 V. A cathodic current for copper is observed when the electrode potential reaches

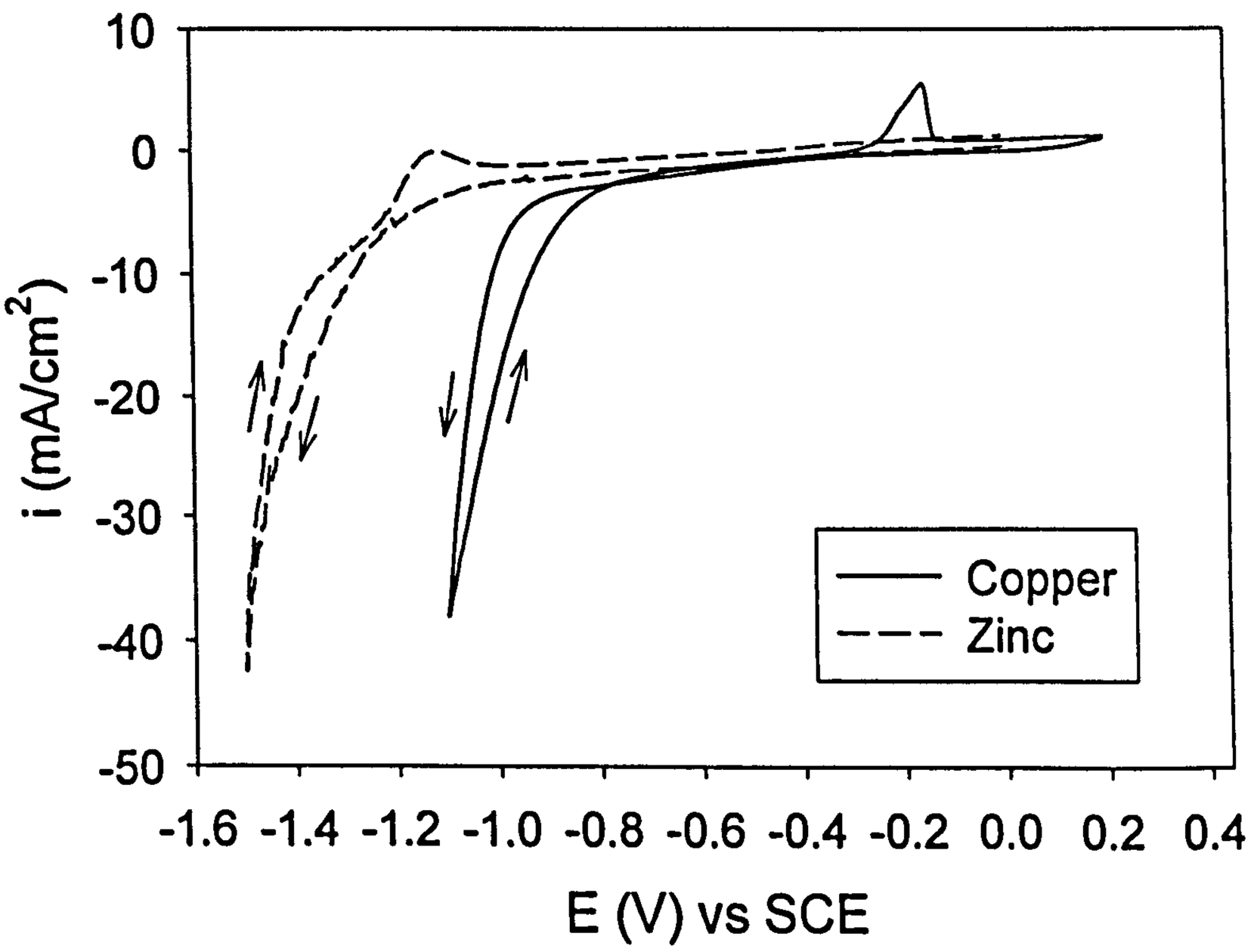

Figure 5.1 "Polarisation profiles for Cu & Zn reduction"

Cyclic voltammograms of copper in pyrophosphate solution, pH 8.4; [$P_2O_7^{4-}$] 0.0324M; [Cu^{2+}] 0.01M; [NO_3^-] 0.12M, and zinc in pyrophosphate solution, pH 8.4; [$P_2O_7^{4-}$] 0.299M; [Zn^{2+}] 0.09M; [NO_3^-] 0.12M; using a gold rotating disc (1000rpm). Scan rate is 0.3 V s^{-1}

below - 0.8 V. As the potential is swept to more negative values, the current increases. The reverse scan exhibits hysteresis, with the reversible potential

shifting towards - 0.7 V. A dissolution peak with a shoulder is observed at potentials greater than - 0.38 V. A cathodic current is observed with the zinc deposition electrolyte at - 1.1 V and dissolution peak is observed at - 1.3 V.

The polarisation profile for brass electroreduction at a RDE under the same conditions performed for copper and zinc electroreduction is shown in Fig 5.2. In this instance with a lower scan limit of - 1.2 V, a cathodic current is detected at - 0.8 V and on the reverse scan a broad dissolution peak appears at - 0.31 V, however it was observed that the features of this scan like the profile of the dissolution peak are dependent on the lower limit of the scan and hence the variation in alloy composition of the brass.

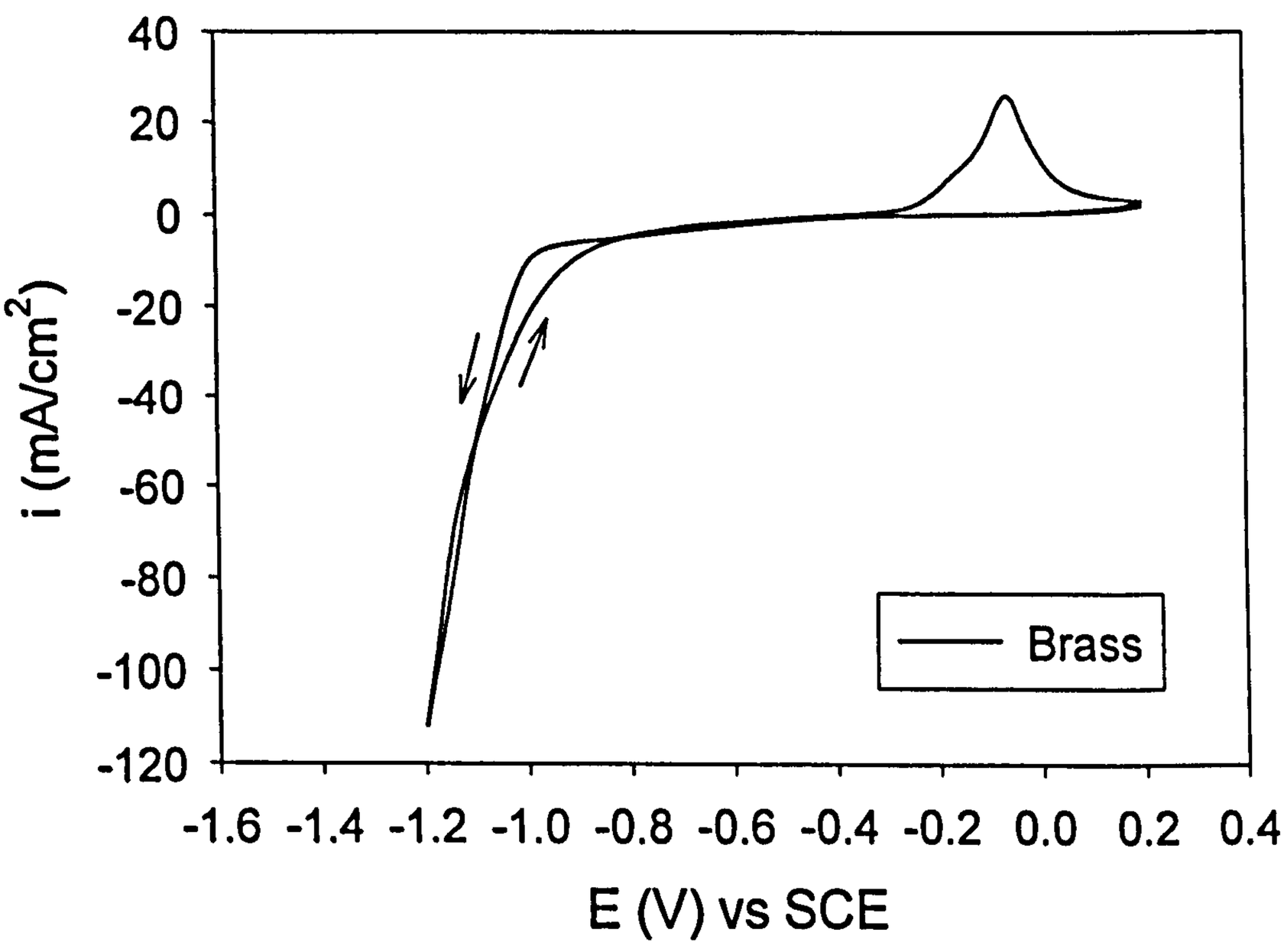

Figure 5.2 "Polarisation profile for Brass reduction"

Cyclic voltammogram of copper and zinc in pyrophosphate solution, pH 8.4; $[P_2O_7^{4-}]$ 0.33M; $[Cu^{2+}]$ 0.01M; $[Zn^{2+}]$ 0.09M; $[NO_3]$ 0.12M; using a gold rotating disc (1000rpm). Scan rate is 0.3 V s^{-1}

5.1 BACKGROUND CURRENT

Partial currents for copper and zinc discharge can be computed from the polarisation data if the current for hydrogen evolution is known and subtracted. In an attempt to determine the background current for hydrogen evolution, cyclic voltammetry was carried out upon a 0.23 M potassium pyrophosphate solution, omitting copper and zinc from the electrolyte.

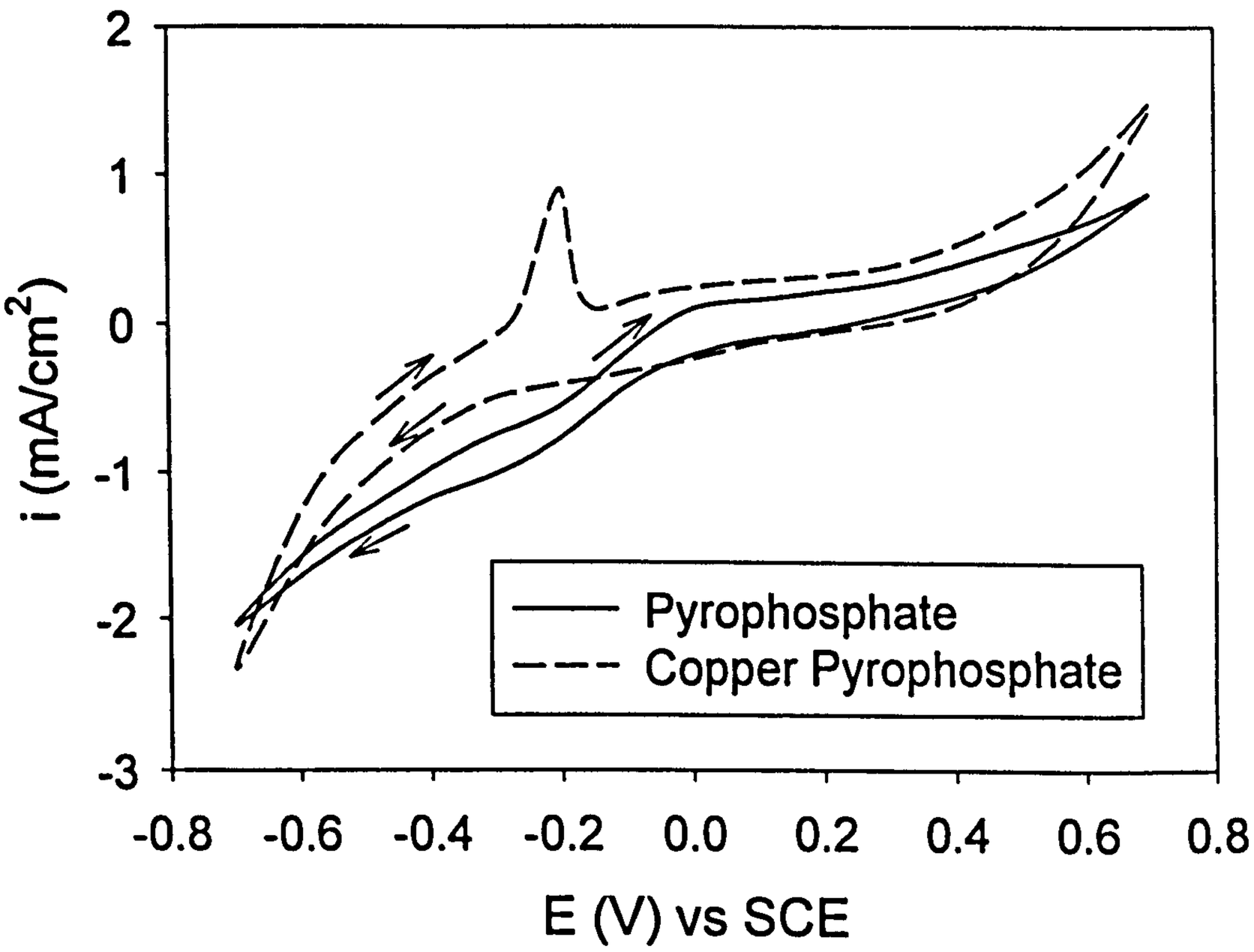

Figure 5.3 "Hydrogen evolution current"

Cyclic voltammograms of copper in pyrophosphate solution, pH 8.4; $[P_2O_7^{4-}]$ 0.0324M; $[Cu^{2+}]$ 0.01M; $[NO_3^-]$ 0.12M, and pyrophosphate, pH 8.4; $[P_2O_7^{4-}]$ 0.23M; $[NO_3^-]$ 0.12M, using a gold rotating disc (1000rpm). Scan rate is 0.3 V s^{-1}

However, as shown in Fig 5.3, it was observed that with the absence of copper and zinc ions from the electrolyte, the discharge currents were found

to be 'higher'. With this event, the actual partial currents for copper and zinc could not be calculated from RDE polarisation experiments.

5.2 CURRENT EFFICIENCY

Determination of Current Efficiencies

Integral Analysis: The current efficiency information gathered from the polarisation data from cyclic voltammetry for copper and zinc pyrophosphate baths, proved inconclusive due to the formation of a blue-green surface oxide upon copper deposits and a grey-blue one on zinc deposits at positive overpotentials. These oxide films prevented absolute dissolution of the metal deposits when sweeping the potential anodically. Polarisation data from both RDE and RCE cyclic voltammetry provided inaccurate current efficiency information.

Gravimetric Analysis: The most accurate way found to determine current efficiency was by carrying out the second series of experiments employing RCE - gravimetric analysis at set plating potentials for copper, zinc and brass. Fig 5.4 shows the current efficiency for copper, zinc and brass deposition. The current efficiency for copper and zinc discharge was small and difficult to measure approaching the reversible potential, and an excessive overpotential, the accuracy of data in these regions was questionable and is not presented here. The current efficiency for copper discharge rises sharply peaking at a maximum of 45% at -0.95 V, then begins to fall just as sharply before a more gradual decline. Exactly the same phenomenon for the current efficiency of zinc was witnessed, although the current efficiency is much less efficient, peaking at -1.64 V, always below 15%. Brass plated in the region -1.35 to -1.66 V appears to have a linear current efficiency function, whereby it follows a trend line from the point where the current efficiency for copper deposition peaks for copper rich brasses lowering to the current efficiency peak for zinc as the brass becomes richer with zinc.

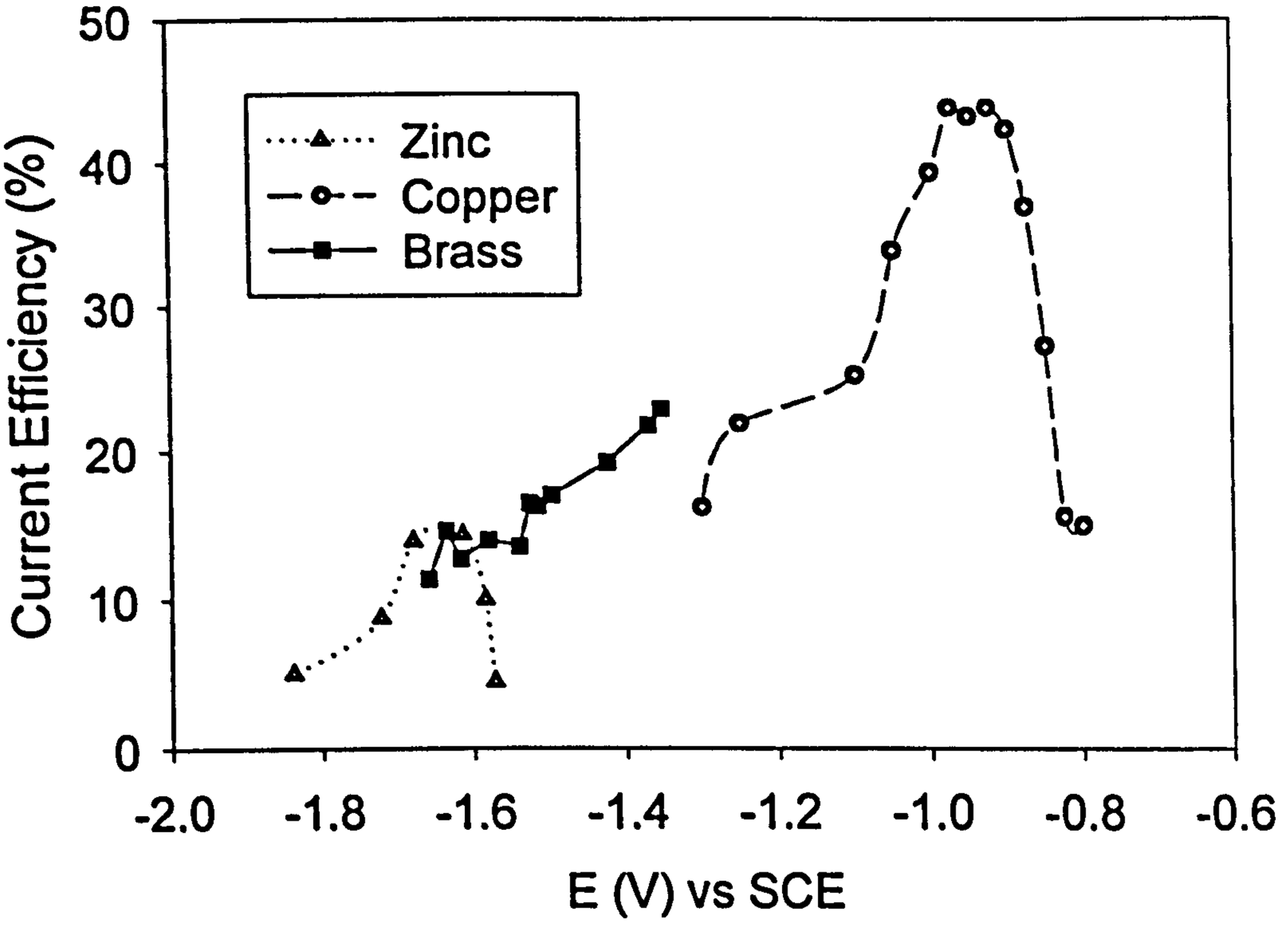

Figure 5.4 "Current Efficiency"

Current efficiency values for copper, zinc and brass pyrophosphate plating solutions determined by gravimetric analysis.

Omission of Nitrate

To determine the influence of nitrate ions on the current efficiency of electroplated brass foils, nitrate was left out of a newly prepared electrolyte. Although current efficiency values did increase, Fig 5.5 shows that the polarisation data from RDE experiments was often erratic and not reproducible. The deposits produced employing a RCE were rough, crumbly and had succumbed to severe phase separation.

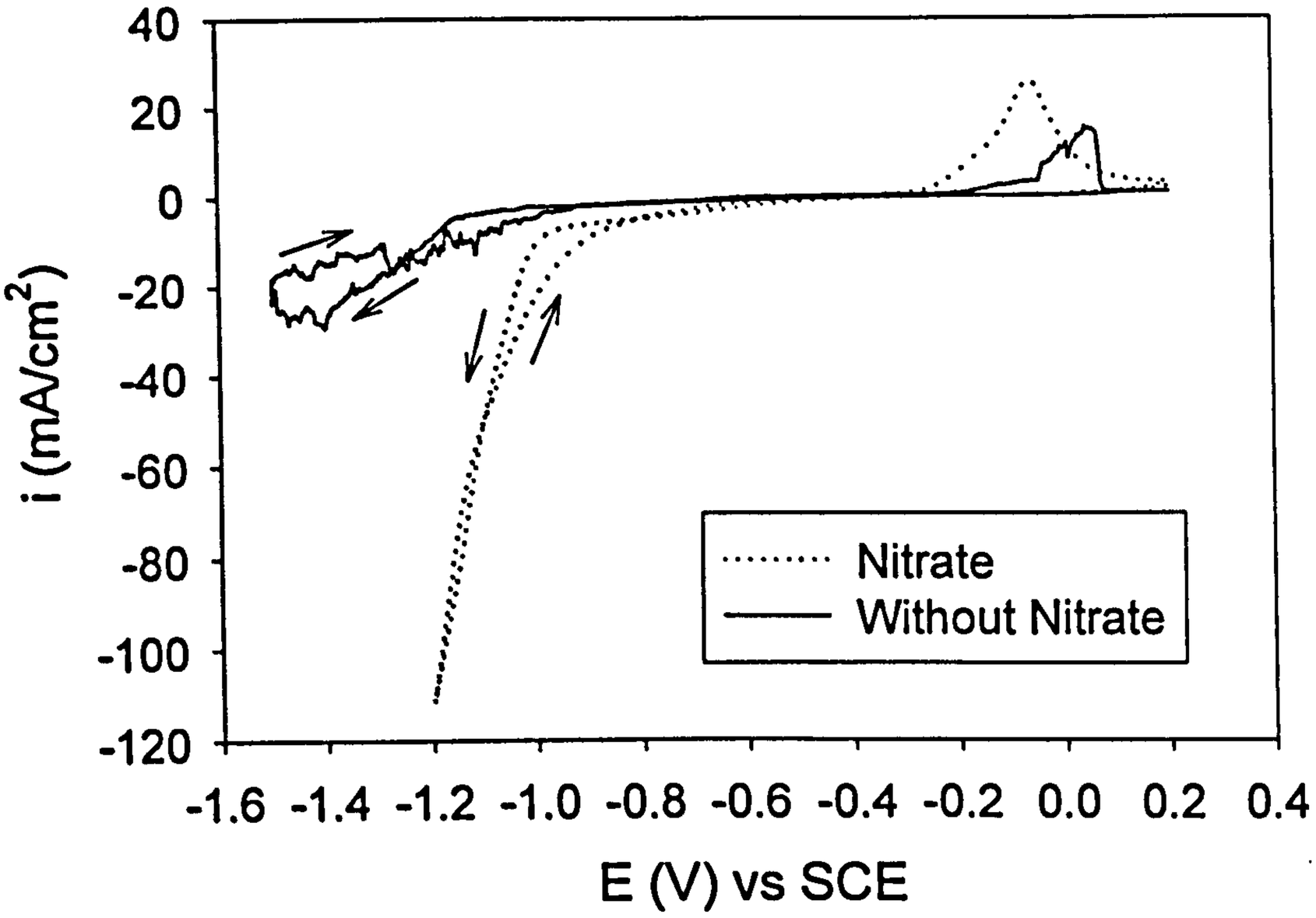

Figure 5.5 "The influence of Nitrate ions"

Cyclic voltammograms of copper and zinc in pyrophosphate solution, pH 8.4; $[P_2O_7^{4-}]$ 0.33M; $[Cu^{2+}]$ 0.01M; $[Zn^{2+}]$ 0.09M, with and without $[NO_3^-]$ 0.12M, using a gold rotating disc (1000rpm). Scan rate is 0.3 V s^{-1}

Nitrate loss from a pyrophosphate plating solution

Employing a RCE for 12 hours at -1.52 V (current density 30.55 mA/cm^2) with a freshly made electrolyte, produced a brass deposit with a composition of 39.41 wt % zinc. During deposition, the pH of the electrolyte increased from 8.40 to 8.63.

UV-VIS spectroanalysis was employed to measure nitrate depletion. The UV-visible spectrums of a 1 and 2 hour old pyrophosphate plating solution (Fig 5.6 & 5.7), exhibit absorption peaks at 294.1 and 293.2 nm respectively for the nitrate species. Nitrite absorption is expected at 354.5 nm as determined

from the calibration set, the literature value and from the addition of potassium nitrite to a fresh plating solution (the same peak was obtained).

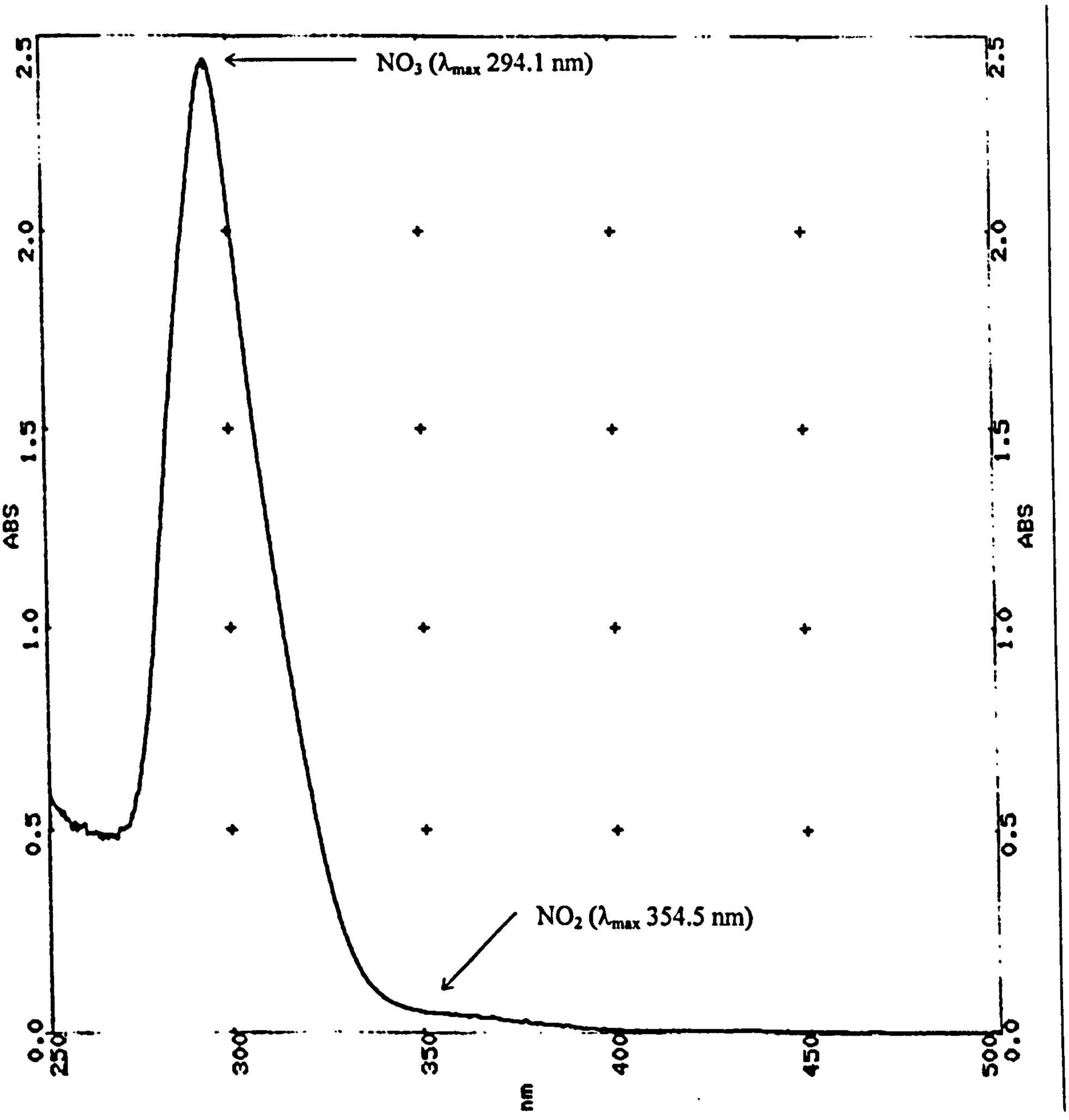

Figure 5.6 "Cu-Zn Pyrophosphate solution 1 hour old"

UV-Visible spectrum of the copper-zinc pyrophosphate electrolyte, after depositing brass for 1 hour at 30.55 mA/cm^2; Bandwidth 1.0 nm; Scan speed 50 nm/min; No smoothing.

The spectrums 1 hour apart, show a decrease in nitrate concentration and a slow increase in nitrite concentration. Of the 0.12 moles of nitrate originally in the electrolyte, 0.01997 moles was reduced to the nitrite species. The final concentration of nitrite in the used electrolyte was found to be 0.00544 moles. The unaccounted loss of a further 0.01453 moles of nitrate after its reduction to nitrite would have been further reduced to produce ammonia.

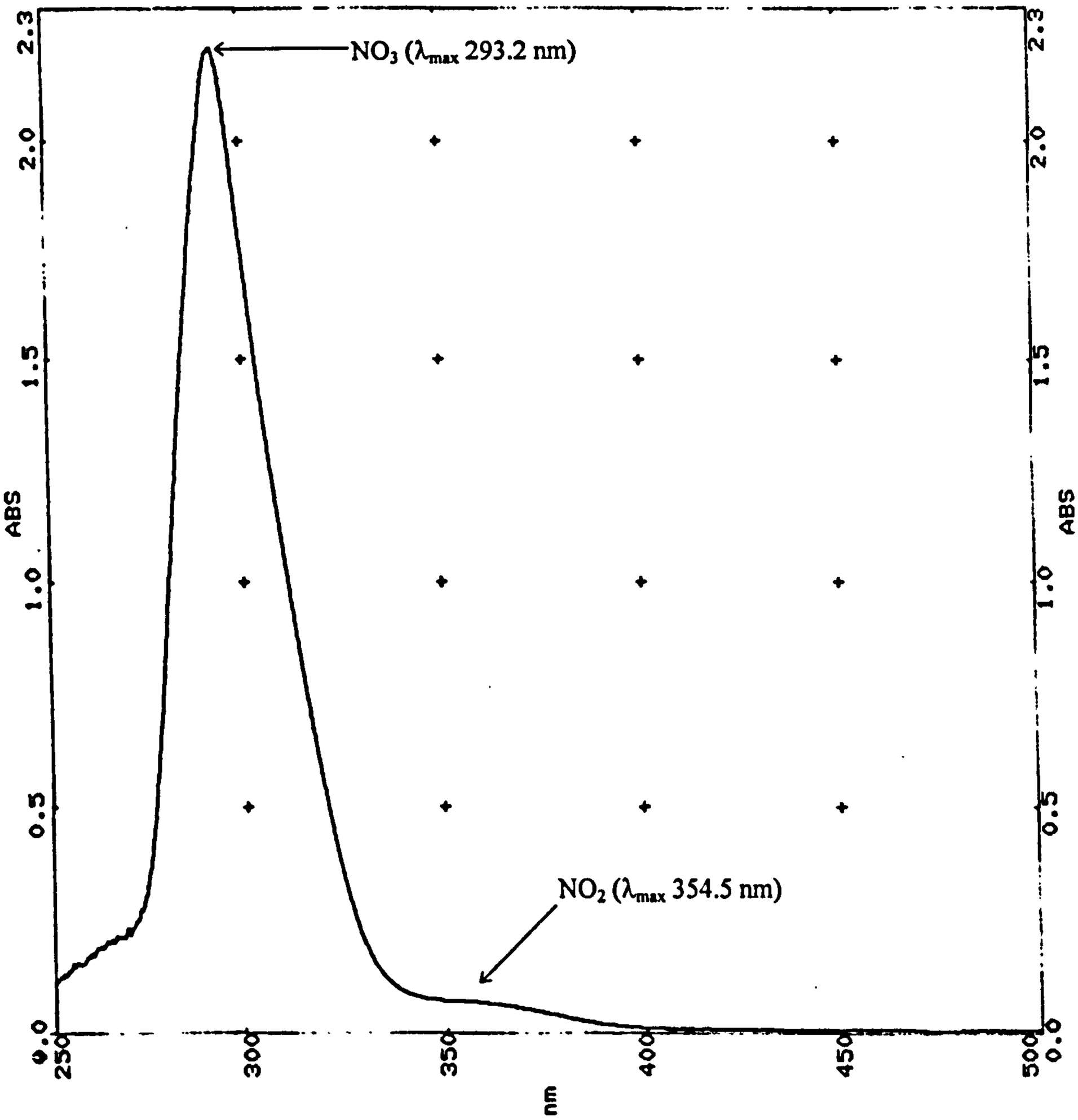

Figure 5.7 "Cu-Zn Pyrophosphate solution 2 hours old"

UV-Visible spectrum of the copper-zinc pyrophosphate electrolyte, after depositing brass for 2 hours at 30.55 mA/cm^2; Bandwidth 1.0 nm; Scan speed 50 nm/min; No smoothing.

The current efficiency for the deposition of brass determined by gravimetric analysis was found to be 16.31%. A further 5.80% and 12.66% of the total current passed was from the reduction of the nitrate to nitrite and nitrite to ammonia respectively.

5.3 PARTIAL CURRENTS

Copper & Zinc Deposition

Fig 5.8 shows the applied current densities used for plating copper and zinc foils at a RCE for gravimetric analysis. This figure then shows the applied current densities as a function of the observed current efficiencies performed at these plating potentials to reveal the true partial currents for copper and zinc.

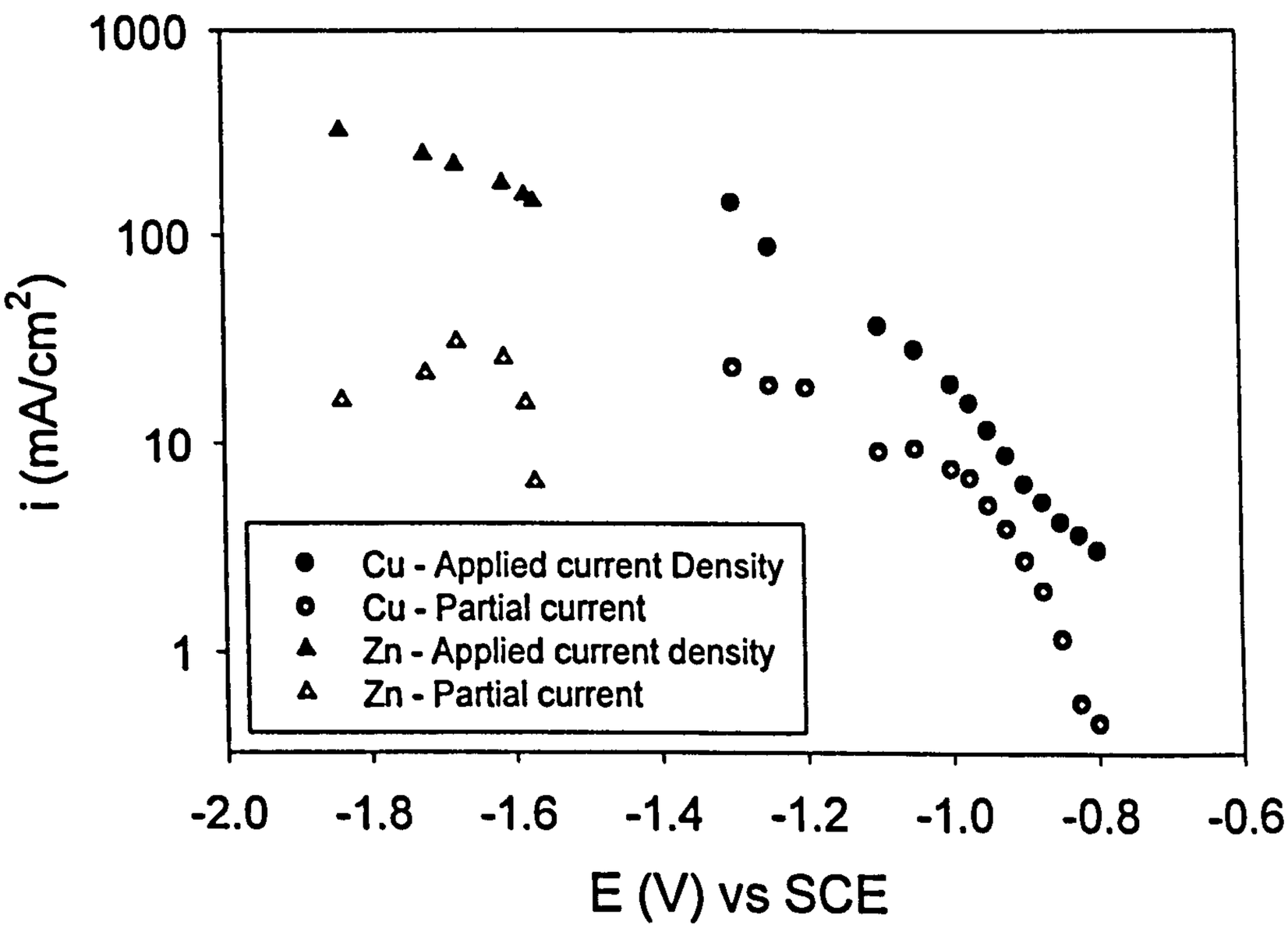

Figure 5.8 "Applied and partial currents of Cu & Zn"

Total measured currents for copper and zinc pyrophosphate plating solutions at set plating potentials. Partial currents determined from the total measured currents as a function of current efficiency.

Copper reduction is shown to begin approximately at - 0.8 V, the reduction current then transcends in a linear fashion up to - 1.0 V, whereupon it starts to level out reminiscent to a mass transfer limiting current plateau. For a rotation

speed of 1000 rpm, a metal ion concentration of 0.01M and a diffusion coefficient of 7.2×10^{-6} cm^2 s^{-1} the diffusion limiting current is calculated to be 10.8 mA cm^{-2}. The reduction current for zinc follows a similar trend as seen for copper. Zinc deposition commences at potentials below -1.5 V, this is followed by a sharp rise in reduction current to the emergence of a possible plateau region. Further analysis for zinc was impossible, due to the formation of dark, fragile, non-metallic deposits at higher negative overpotentials.

Brass Deposition

The separate partial currents for copper and zinc during brass deposition at constant potentials was determined by gravimetric analysis and alloy composition by EDAX and from a measure of the total current passed are shown in Fig 5.9. Zinc reduction from the brass electrolyte commences at approximately - 1.35 V, a much higher negative potential when compared with zinc deposition from the zinc electrolyte, - 1.1 V. A limiting current plateau for zinc with a smaller order than that seen with the zinc electrolyte is evident. Copper deposition from the brass electrolyte occurs at - 0.5 V, a lower negative potential when compared with electrodeposition from the copper electrolyte, - 0.8 V. Copper also forms a limiting current plateau. Both the partial currents for copper and zinc start to decline with an increasing negative overpotential, although the actual trends could not be fully determined as deposition beyond - 1.66 V, produced deposits very brittle, dark and rough. Over the narrow potential range of 300mV from - 1.35 V to - 1.65 V, brass foil compositions ranged from 0 - 60.5 wt % zinc.

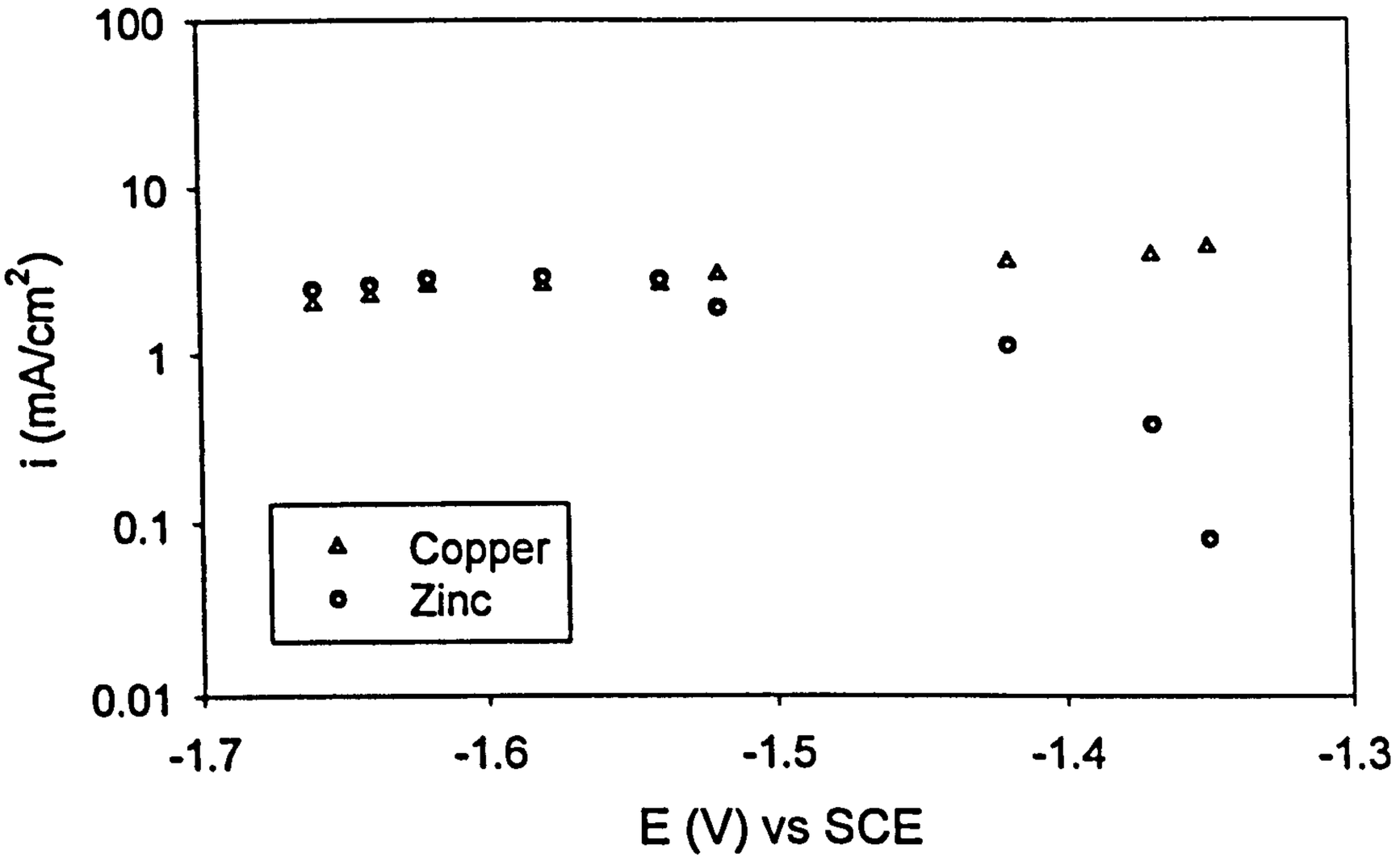

Figure 5.9 "Partial current densities during brass deposition"

Partial currents of copper and zinc from a copper / zinc pyrophosphate plating solution, determined from set plating potentials, gravimetric analysis and EDAX measurements.

5.4 ROTATION SPEED EFFECTS

Polarisation Data

A study into the effect of rotation speed of the RDE revealed that the polarisation data for copper and zinc experienced only a slight change when the rotation speed was increased from 500 to 1000 rpm. This is shown in Fig 5.10 from the forward scans of cyclic voltammetry performed on copper and zinc pyrophosphate electrolytes. Further increments in RDE rotation speed up to 2400 rpm revealed little notable change than when performed at 1000 rpm. The scans evidently show there are no strong mass transfer limitations in either case.

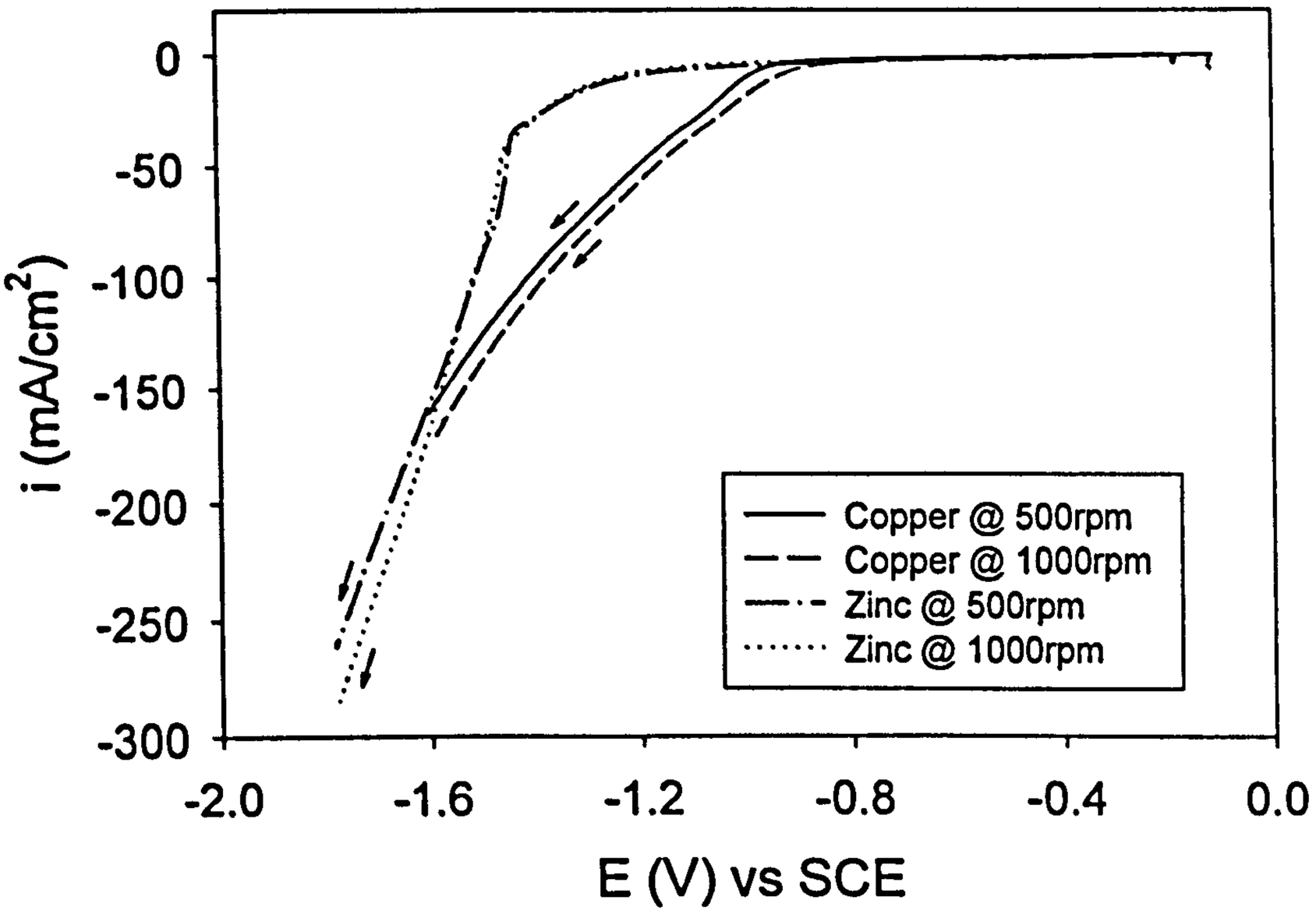

Figure 5.10 "RDE Rotation Speed"

Forward scans of cyclic voltammograms of copper in pyrophosphate solution, pH 8.4; $[P_2O_7^{4-}]$ 0.0324M; $[Cu^{2+}]$ 0.01M; $[NO_3]$ 0.12M, and zinc in pyrophosphate solution, pH 8.4; $[P_2O_7^{4-}]$ 0.299M; $[Zn^{2+}]$ 0.09M; $[NO_3]$ 0.12M; performed with a gold rotating disc at 500 & 1000rpm. Scan rate is 0.3 V s^{-1}.

$CuZn_5$

The deposition of brass at a RCE with a rotation speed of 500 rpm was found to always be preceded by a 1.5μm $CuZn_5$ layer. The variation in current densities at fixed potentials during the first few minutes of electrodeposition with different RCE rotation speeds is shown in Fig 5.11. At 500 rpm, it was revealed for the initial period of 4 - 5 minutes the current density was always relatively high, in comparison to the final current density. The current density dropped dramatically after this initial period and became constant for the duration of the experiment. This phenomenon never revealed itself during the plating trials with RCE rotation speeds of over 1000 rpm.

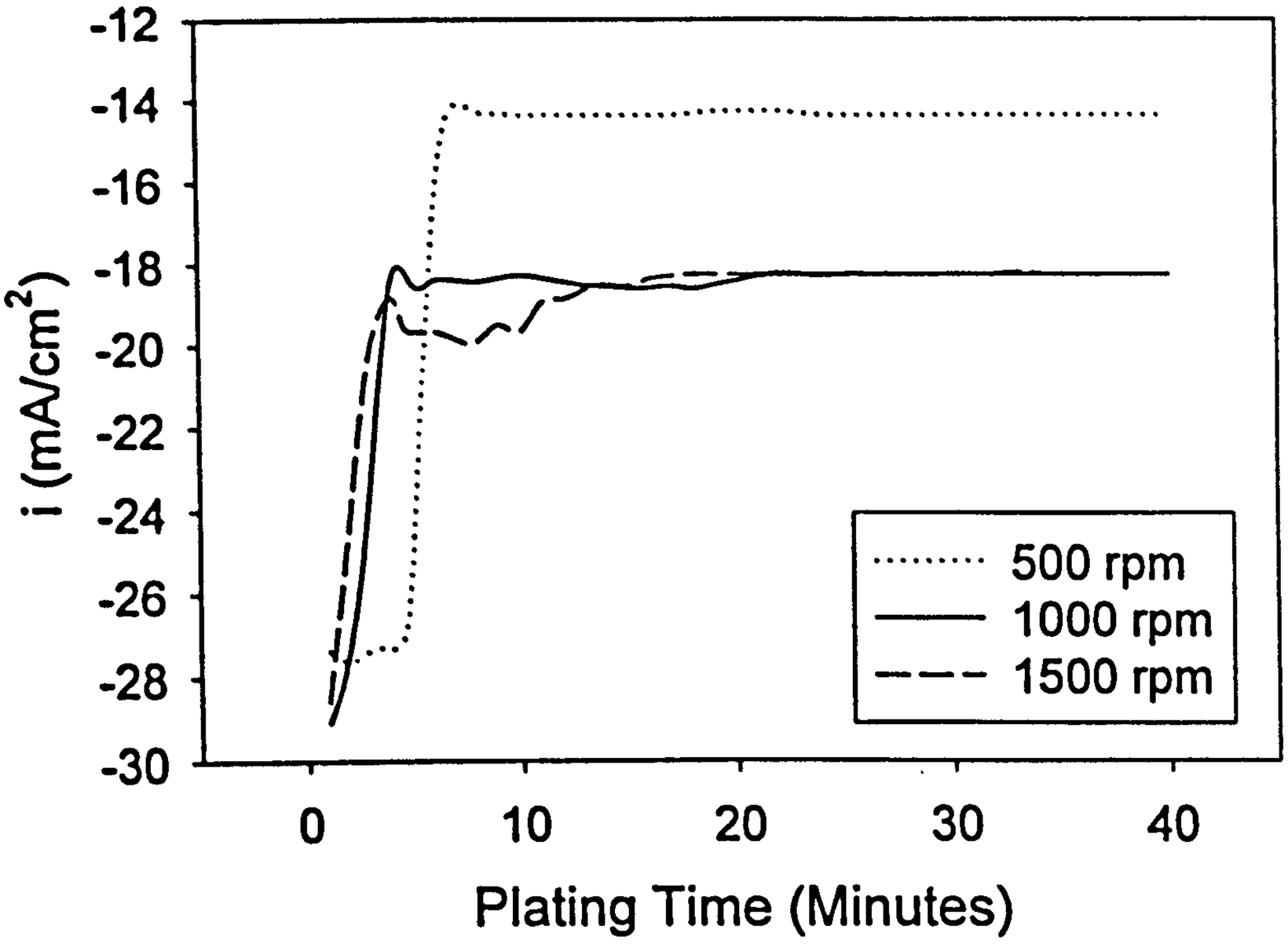

Figure 5.11 "Current Density Fluctuation"

Current density variation during the first 40 minutes of brass deposition from a copper and zinc pyrophosphate solution under potentiostatic control, pH 8.4; $[P_2O_7^{4-}]$ 0.33M; $[Cu^{2+}]$ 0.01M; $[Zn^{2+}]$ 0.09M; $[NO_3^-]$ 0.12M; using a RCE.

pH Change at electrode surface

Employing a rotation speed of 1000 rpm, brass foils were electrodeposited with compositions from 29 to 53 wt % zinc, with respect to increasing the applied current density from 24.18 to 39.78 mA/cm^2 for each plating experiment. The small variation in pH at the electrode surface was observed (Fig 5.12) to be between pH 10.18 to 10.60 during these electrodeposition trials.

With a rotation speed of 500 rpm, brass foils were electrodeposited with compositions varying from < 1 to 64 wt % zinc, with the corresponding change

in applied current density from 17.18 to 45.43 mA/cm^2. A large variation in pH was observed (Fig 5.13), between pH 9.98 and 11.55.

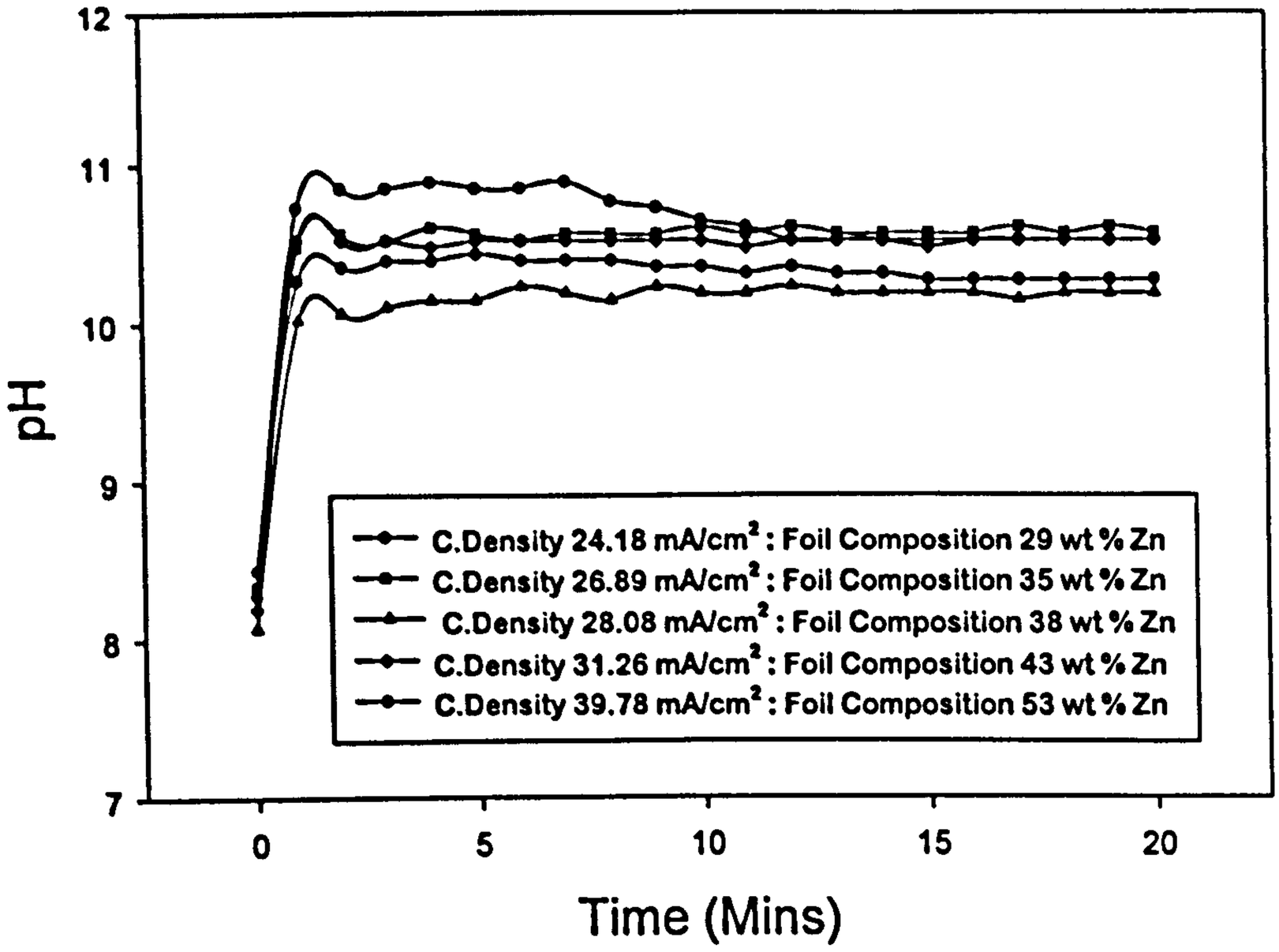

Figure 5.12 "pH at RCE surface: Rotation Speed 1000rpm"

Measurement of pH at the RCE surface during the first 20 minutes of brass deposition from a copper and zinc pyrophosphate solution, pH 8.4; [$P_2O_7^{4-}$] 0.33M; [Cu^{2+}] 0.01M; [Zn^{2+}] 0.09M; [NO_3^-] 0.12M; employing a RCE (1000rpm) at different applied current densities.

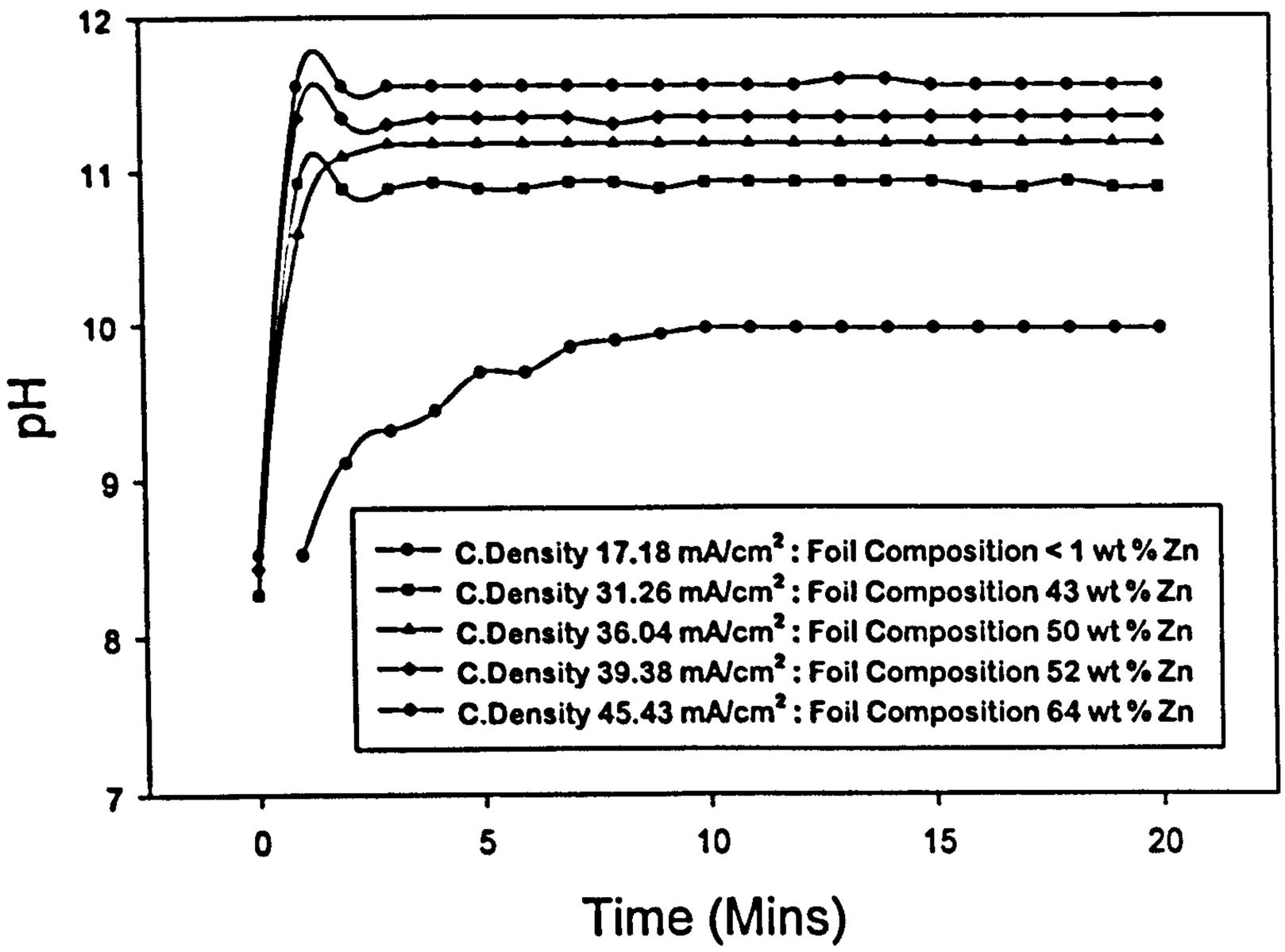

Figure 5.13 "pH at RCE surface: Rotation Speed 500rpm"

Measurement of pH at the RCE surface during the first 20 minutes of brass deposition from a copper and zinc pyrophosphate solution, pH 8.4; $[P_2O_7^{4-}]$ 0.33M; $[Cu^{2+}]$ 0.01M; $[Zn^{2+}]$ 0.09M; $[NO_3]$ 0.12M; employing a RCE (500rpm) at different applied current densities.

Modelling of pyrophosphate speciation

The distribution of copper and zinc species for the pyrophosphate plating bath are shown in Fig's 5.14 and 5.15 respectively, as a function of pH. At the solution pH of 8.4, the dominant copper species is shown to be $Cu(P_2O_7)_2^{6-}$ (97%) with a small amount (3%) of $CuP_2O_7^{2-}$ also present. The main species present for zinc at a pH of 8.4 are $ZnP_2O_7^{2-}$ (81%), $Zn(P_2O_7)_2^{6-}$ (15%) and $ZnOHP_2O_7^{3-}$ (4%). Approaching a pH of 10, it is very probable that the solution will become unstable due to the formation of precipitates of $Cu(OH)_2$ and $Zn(OH)_2$. It is noted that the calculated species distribution may not exactly match the experimental distribution due to the difference in ionic

strength and also the neglect of heterogeneous kinetic processes which will perturb the equilibria in the vicinity of the electrode surface. The hydrolysis of pyrophosphate has also been neglected in the model, but the rate of this reaction is known to be very slow under alkaline conditions. Despite these reservations, the speciation calculations should provide an accurate indication of the relative concentrations of the various species present in the pyrophosphate plating solution.

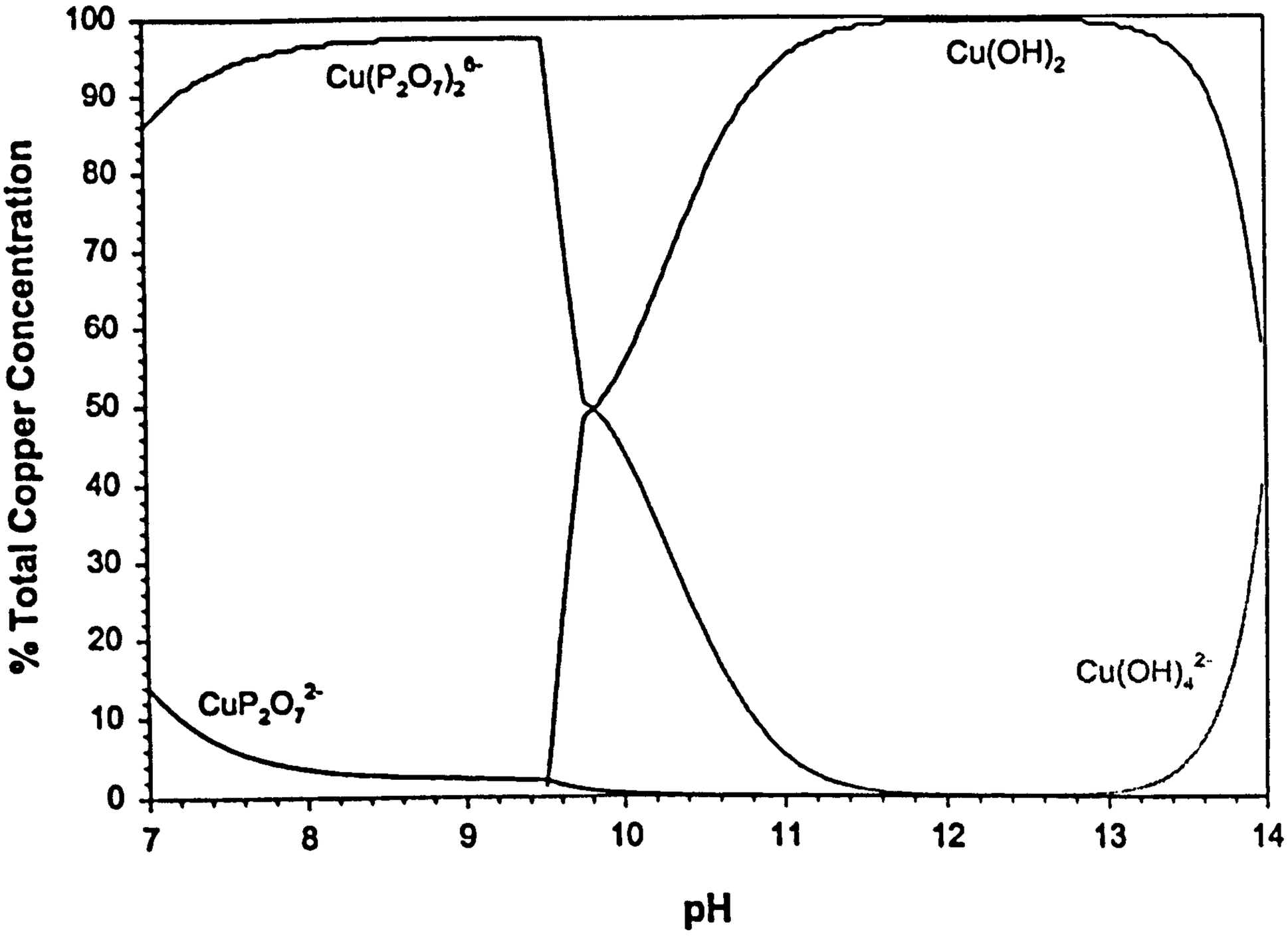

Figure 5.14 "Copper Pyrophosphate Species"

Mineql* distribution plot of the dominant copper species in a copper and zinc pyrophosphate solution, pH 8.4; $[P_2O_7^{4-}]$ 0.33M; $[Cu^{2+}]$ 0.01M; $[Zn^{2+}]$ 0.09M; $[NO_3]$ 0.12M.

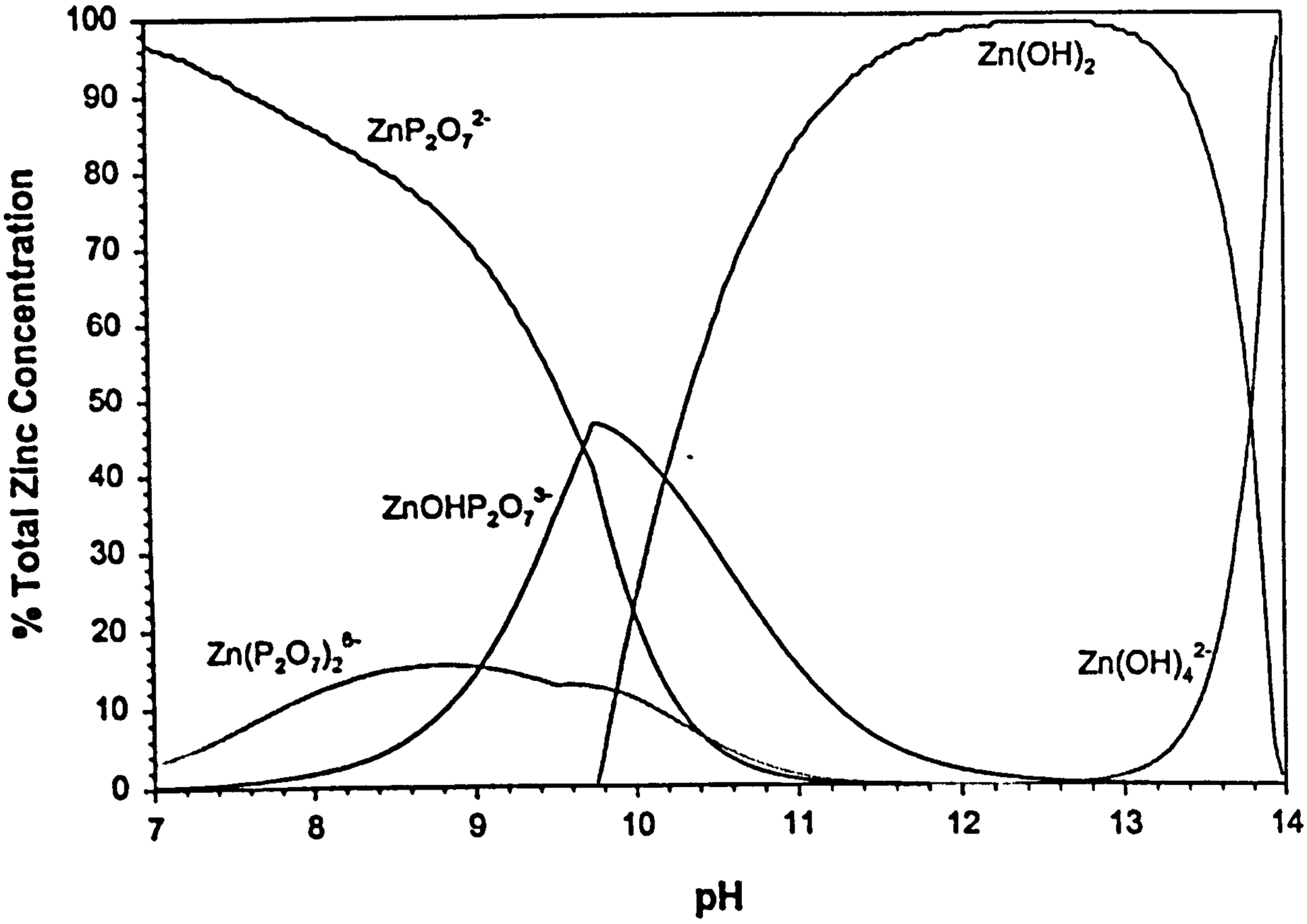

Figure 5.15 "Zinc Pyrophosphate Species"

Mineql* distribution plot of the dominant zinc species in a copper and zinc pyrophosphate solution, pH 8.4; $[P_2O_7^{4-}]$ 0.33M; $[Cu^{2+}]$ 0.01M; $[Zn^{2+}]$ 0.09M; $[NO_3]$ 0.12M.

CHAPTER 6

- MATERIAL CHARACTERISATION -

6.0 X-RAY DIFFRACTION (XRD)

Figures 6.1 to 6.5 show the x-ray diffraction patterns for brass foils of compositions 15.89, 22.12, 38.75, 44.53 and 55.16 wt % zinc respectively. Figure 6.6 is the X-ray diffraction pattern for $CuZn_5$. Tables 6.1 to 6.5 precede each diffraction pattern documenting the observed reflections. Further XRD spectra and data is catalogued and tabulated in Appendix B.

Table 6.1

"Diffraction angles for a 15.89 wt % zinc Brass Foil"

PEAK	Strength	Reflection (2θ)	d - spacing (A)	Orientation	Phase
A	Very Strong	42.5 - 43.2	2.127 - 2.094	111	α
B	Very Strong	41.3 - 42.1	2.186 - 2.146	-	$CuZn_5$
C	Strong	91.3	1.078	-	$CuZn_5$
D	Medium	44.2 - 44.3	2.049 - 2.044	-	S.Holder
E	Medium	89.8	1.092	311	α
F	Medium	77.5	1.232	-	$CuZn_5$
G	Medium	50.0	1.824	200	α
H	Weak	73.8	1.284	220	α
J	Weak	81.6 - 82.0	1.180 - 1.175	-	$CuZn_5$
K	Weak	57.5	1.603	-	$CuZn_5$
L	Weak	64.5	1.444	-	S.Holder

In addition to the reflections from the various brass phases, there are reflections from the XRD mild steel sample holder and although not seen here, the copper underlayer (See Appendix B).

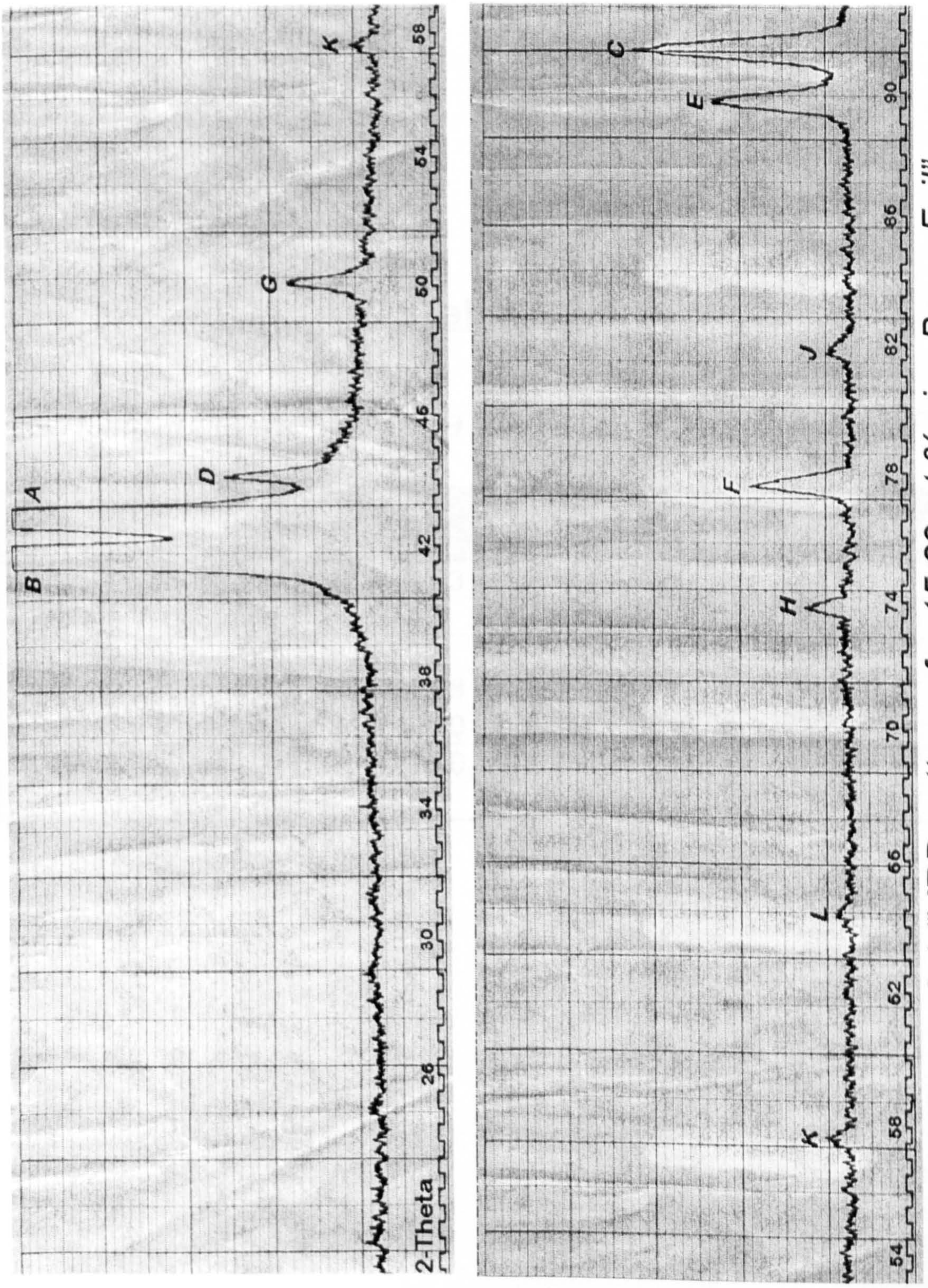

Figure 6.1 "XRD pattern of a 15.89 wt % zinc Brass Foil"

Table 6.2

"Diffraction angles for a 22.12 wt % zinc Brass Foil"

PEAK	Strength	Reflection (2θ)	d - spacing ($\AA$)	Orientation	Phase
A	Very Strong	42.5 - 43.3	2.127 - 2.090	111	α / Cu
B	Very Strong	50.0	1.824	200	α / Cu
C	Strong	44.2	2.049	-	S.Holder
D	Strong	89.5 - 89.8	1.095 - 1.092	311	α / Cu
E	Medium	94.8 - 95.0	1.047 - 1.046	222	α / Cu
F	Weak	73.8 - 74.0	1.284 - 1.281	220	α / Cu
G	Weak	64.5	1.444	-	S.Holder

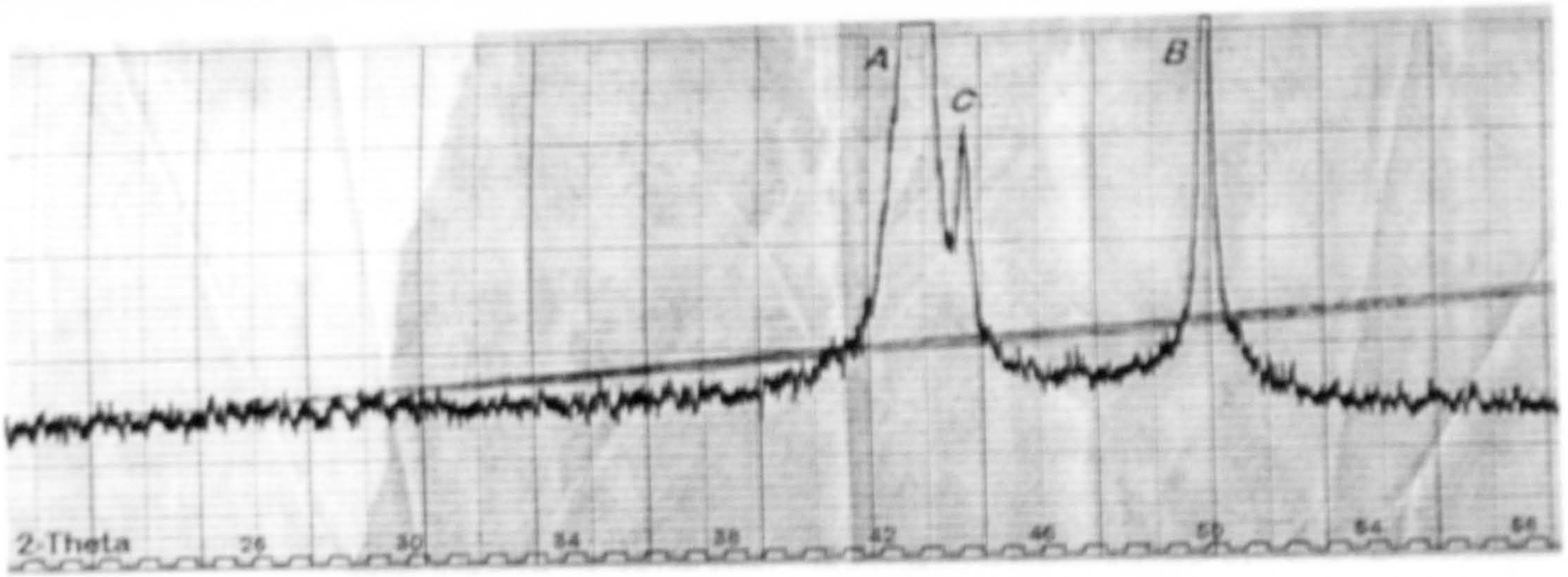

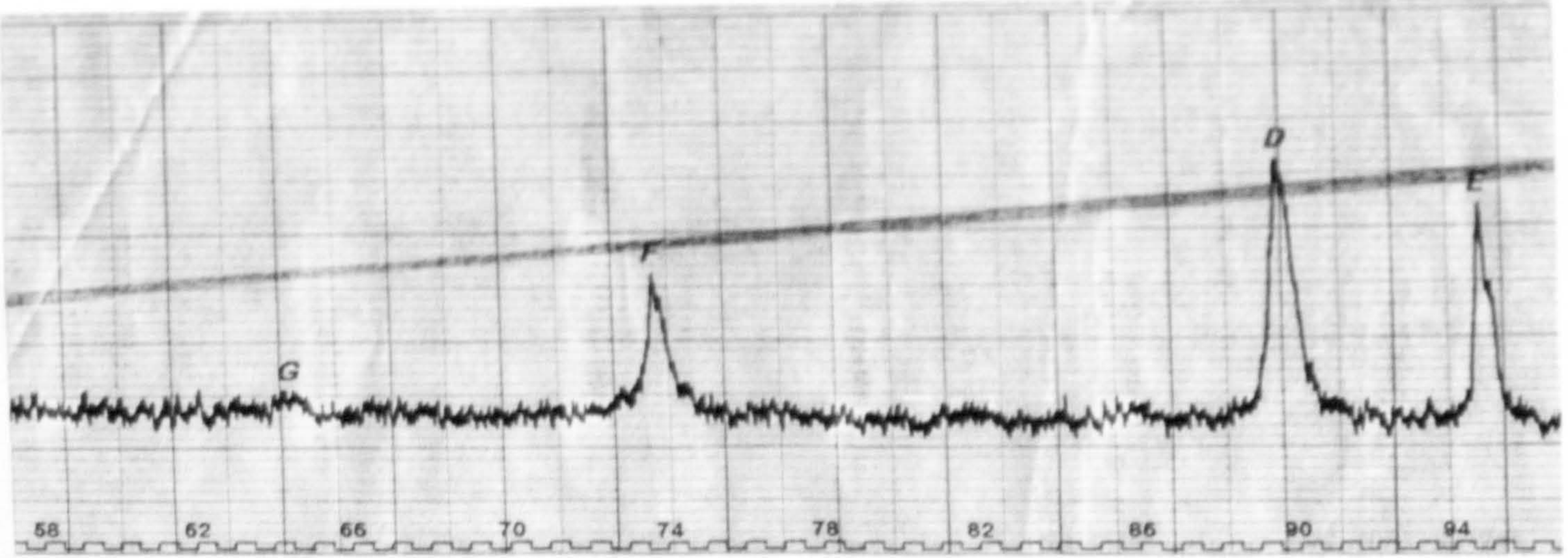

Figure 6.2 "XRD pattern of a 22.12 wt % zinc Brass Foil"

Table 6.3

"Diffraction angles for a 38.75 wt % zinc Brass Foil"

PEAK	Strength	Reflection (2θ)	d - spacing ($\AA$)	Orientation	Phase
A	Very Strong	42.9 - 43.1	2.108 - 2.099	111	α
B	Strong	50.2	1.817	200	α
C	Medium	73.8 - 73.9	1.284 - 1.282	220	α
D	Medium	89.5 - 89.7	1.095 - 1.093	311	α
E	Weak	42.0 - 42.4	2.151 - 2.132	200	β
F	Weak	44.3	2.045	-	S.Holder
G	Weak	39.5 - 40.1	2.281 - 2.249	101/110	β / Mart
H	Weak	94.7 - 95.1	1.048 - 1.045	222	α
J	Weak	87.1 - 88.5	1.119 - 1.105	040/122	β
K	Weak	71.3 - 72.9	1.322 - 1.298	002/020	β / Mart
L	Weak	45.0 - 45.8	2.014 - 1.981	111	β
M	Weak	81.3 - 82.3	1.183 - 1.172	320	β

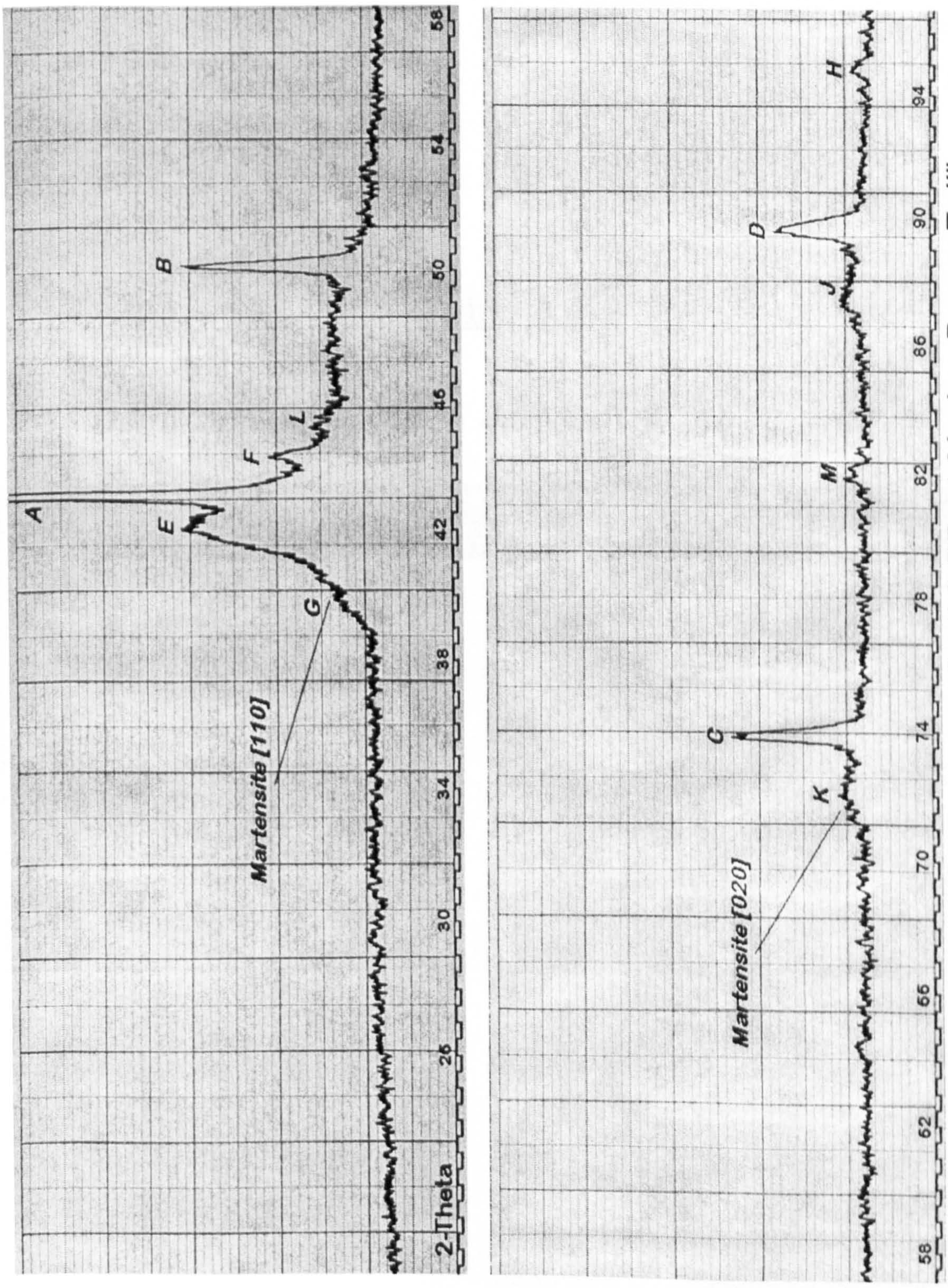

Figure 6.3 "XRD pattern of a 38.75 wt % zinc Brass Foil"

Table 6.4

"Diffraction angles for a 44.53 wt % zinc Brass Foil"

PEAK	Strength	Reflection (2θ)	d - spacing ($\AA$)	Orientation	Phase
A	Very Strong	42.9 - 43.2	2.108 - 2.094	111	α /Cu
B	Medium	44.3	2.045	-	S.Holder
C	Medium	41.6 - 42.3	2.171 - 2.137	200	β
D	Weak	70.1 - 72.2	1.322 - 1.308	002/020	β / Mart
E	Weak	89.6 - 89.8	1.094 - 1.092	311	α /Cu
F	Weak	38.8 - 40.1	2.321 - 2.249	101/110	β / Mart
G	Weak	81.5 - 82.4	1.181 - 1.170	320	β
H	Weak	94.7 - 95.2	1.048 - 1.044	222	α /Cu
J	Weak	50.0 - 50.3	1.824 - 1.814	200	α /Cu
K	Weak	86.0 - 87.4	1.130 - 1.116	040	β
L	Weak	44.6 - 45.3	2.032 - 2.002	111	β

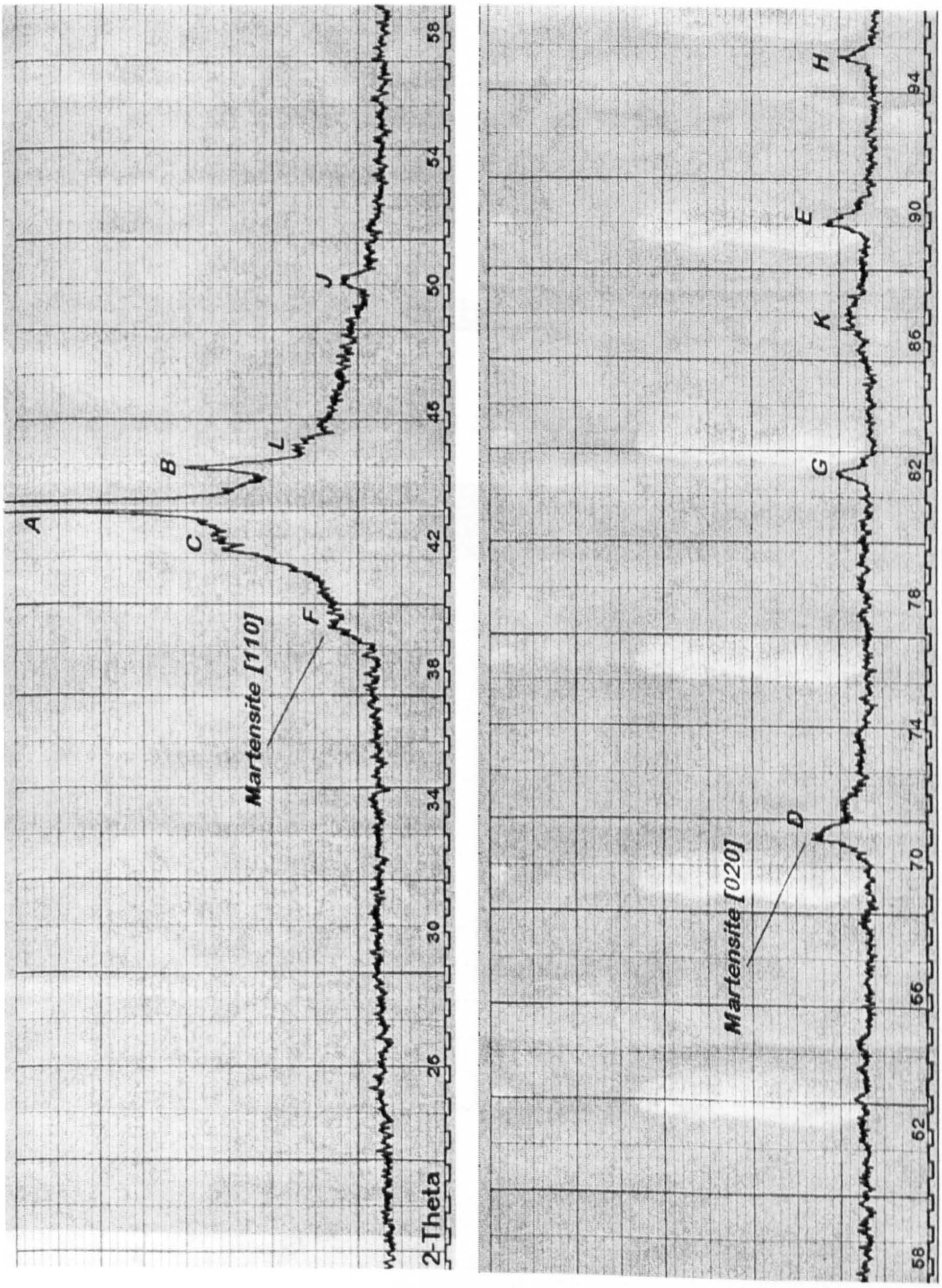

Figure 6.4 "XRD pattern of a 44.53 wt % zinc Brass Foil"

Table 6.5

"Diffraction angles for a 55.16 wt % zinc Brass Foil"

PEAK	Strength	Reflection (2θ)	d - spacing (A)	Orientation	Phase
A	Strong	43	2.103	-	γ
B	Medium	70.6	1.334	002/020	β / Mart
C	Weak	44.3	2.045	-	S.Holder
D	Weak	78.2 - 79.3	1.222 - 1.208	-	γ
E	Weak	34.5 - 35.0	2.599 - 2.564	-	γ
F	Weak	41.5 - 42.4	2.176 - 2.132	200	β
G	Weak	38.8 - 40.1	2.321 - 2.249	101/110	β / Mart
H	Weak	37.9	2.374	-	γ
J	Weak	47.5 - 47.9	1.914 - 1.899	-	γ
K	Weak	86.3	1.127	040	β
L	Weak	81.5 - 82.2	1.181 - 1.173	320	β
M	Weak	89.5 - 89.8	1.095 - 1.092	311	Cu
N	Weak	49.8 - 50.3	1.831 - 1.814	200	Cu
P	Weak	73.6 - 74.1	1.287 - 1.279	220	Cu
R	Weak	94.7 - 95.2	1.048 - 1.044	222	Cu

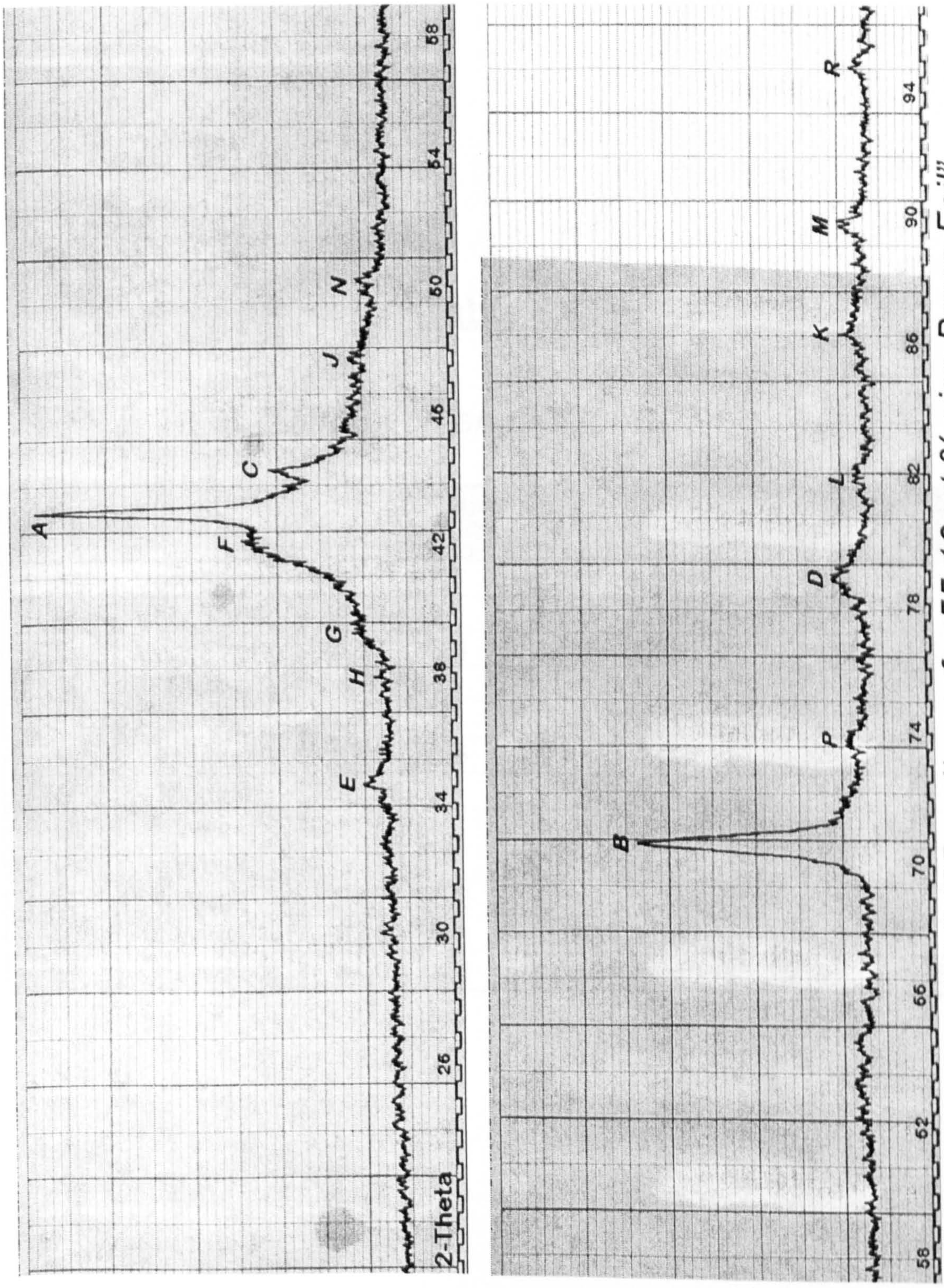

Figure 6.5 "XRD pattern of a 55.16 wt % zinc Brass Foil"

Table 6.6

"Diffraction angles for $CuZn_5$"

PEAK	Strength	Reflection (2θ)	d - spacing (A)	Orientation	Phase
A	Very Strong	77.3 - 77.7	1.234 - 1.229	-	$CuZn_5$
B	Very Strong	41.2 - 42.1	2.191 - 2.146	-	$CuZn_5$
C	Very Strong	42.7 - 43.4	2.118 - 2.085	- / 111	$CuZn_5$/Cu
D	Strong	57.5	1.603	-	$CuZn_5$
E	Strong	91.3	1.078	-	$CuZn_5$
F	Medium	37.3 - 38.5	2.411 - 2.33	-	$CuZn_5$
G	Medium	89.8	1.092	311	Cu
H	Weak	50.0	1.824	200	Cu
J	Weak	73.8	1.284	220	Cu
K	Weak	94.7 - 95.2	1.048 - 1.044	222	Cu
L	Weak	82.9 - 83.3	1.165 - 1.160	-	$CuZn_5$
M	Weak	44.0 - 44.4	2.058 - 2.040	-	S.Holder

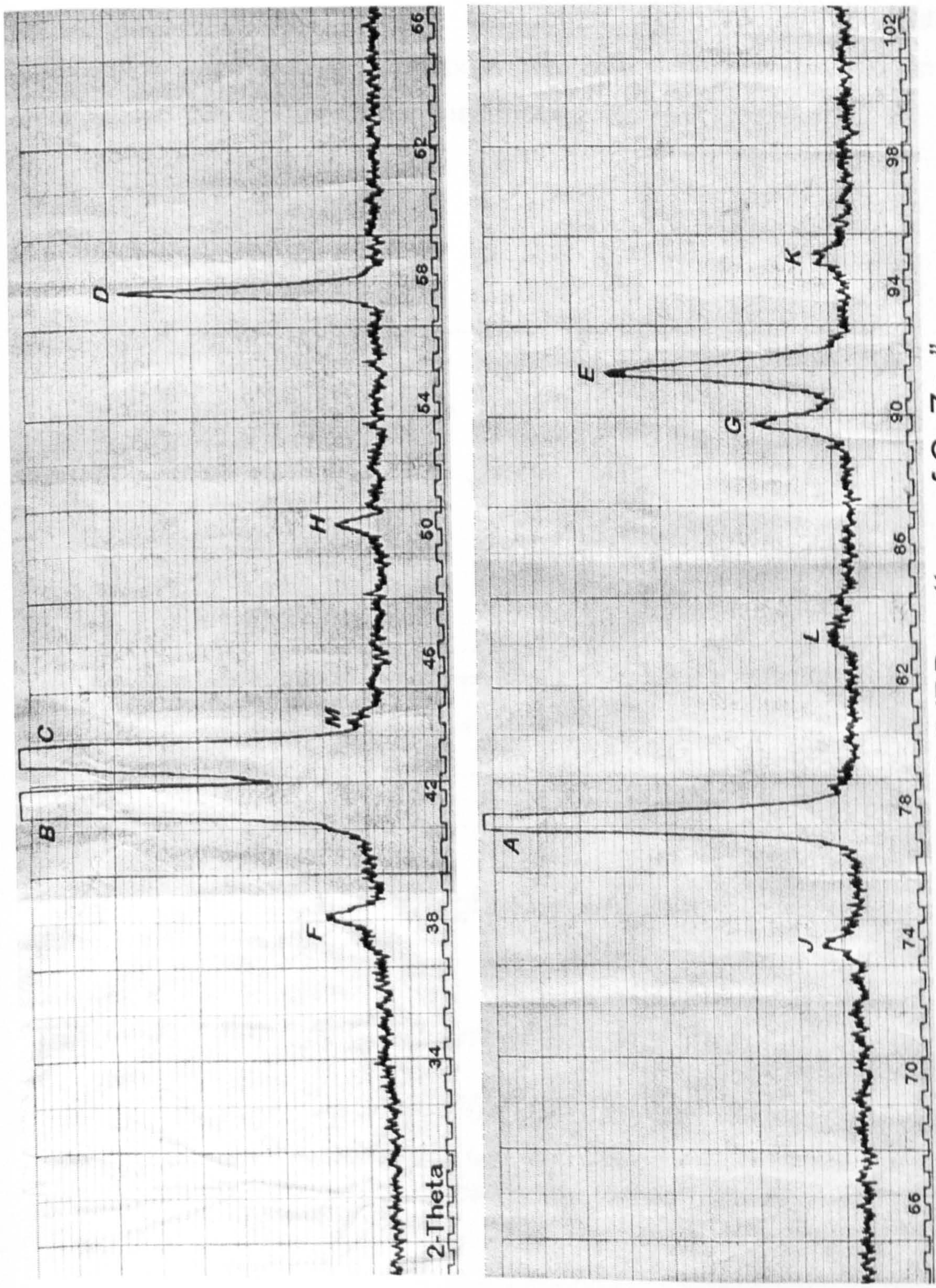

Figure 6.6 "XRD pattern of $CuZn_5$"

Having identified the phase composition for each electroplated brass foil from the phase spectra, a graph (Figure 6.7) showing the deposition potential for each foil against their elemental composition (determined by SEM) was produced. The x-axis also denotes those phases to be expected had brass of the same composition as the foils been produced by conventional metallurgical methods. In retrospect the actual phases present in the electroplated foils are depicted in the legend.

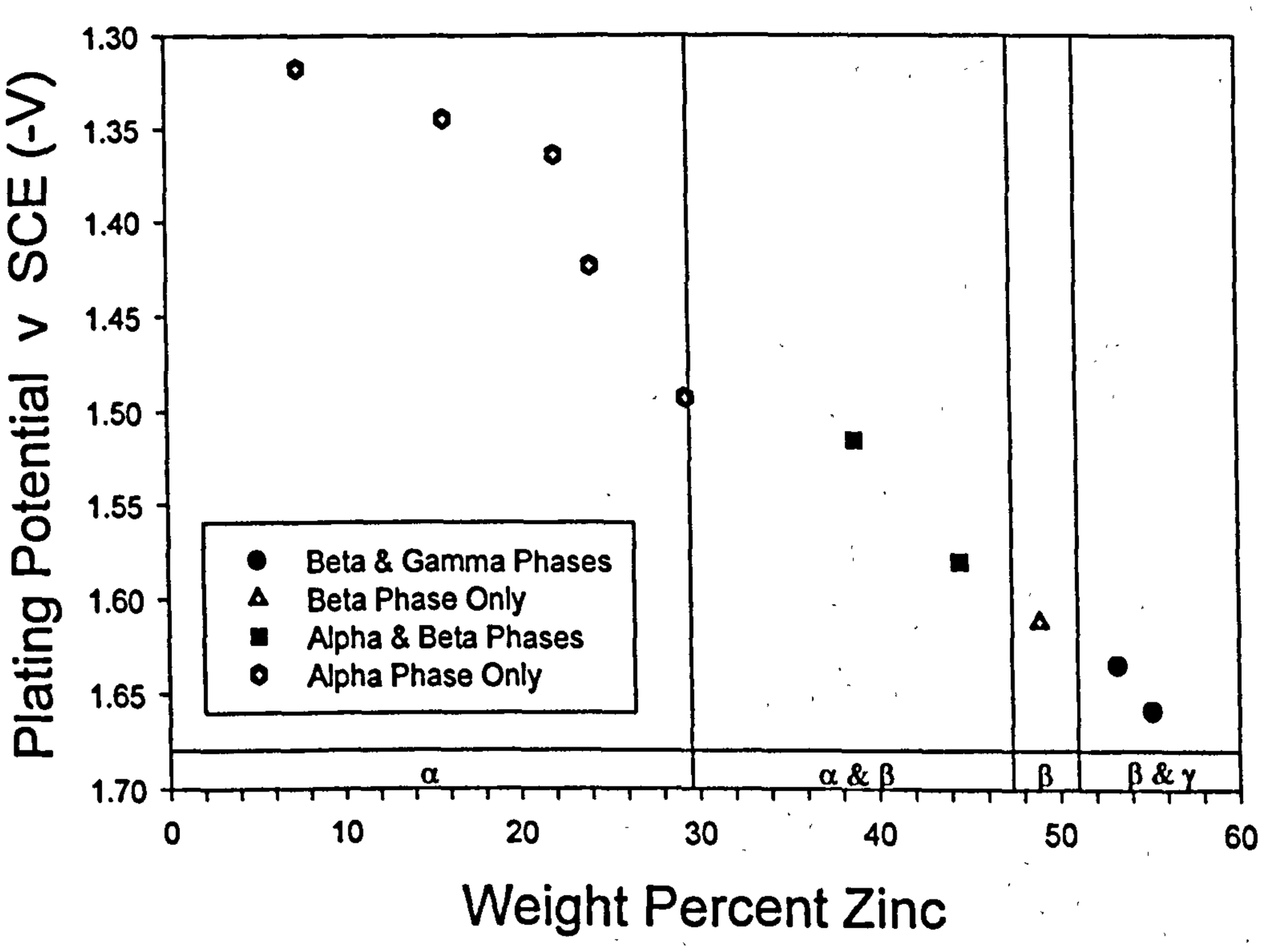

Figure 6.7 "Phase Diagram of Electroplated Brass versus Plating Potential"

The phase composition of deposited brass foils from a copper and zinc pyrophosphate solution, pH 8.4; $[P_2O_7^{4-}]$ 0.33M; $[Cu^{2+}]$ 0.01M; $[Zn^{2+}]$ 0.09M; $[NO_3]$ 0.12M. RCE (1000rpm).

6.1 SCANNING ELECTRON MICROSCOPY & EDAX

The microstructure of the brass foils produced by electrodeposition all appeared (Fig 6.8) to have a very smooth and uniform profile. They were all homogenous, with no voids, oxide inclusions or precipitates detectable. However, the microstructure of the brass foils produced by electrodeposition with the omission of potassium nitrate from the plating electrolyte, all appeared (Fig 6.9) to experience severe phase separation and had a very rough texture (nodular). The approximate areas A to D (Fig 6.9) examined by EDAX were found to have compositions of 85.8, 35.7, 83.5 and 29.9 wt % Zn respectively.

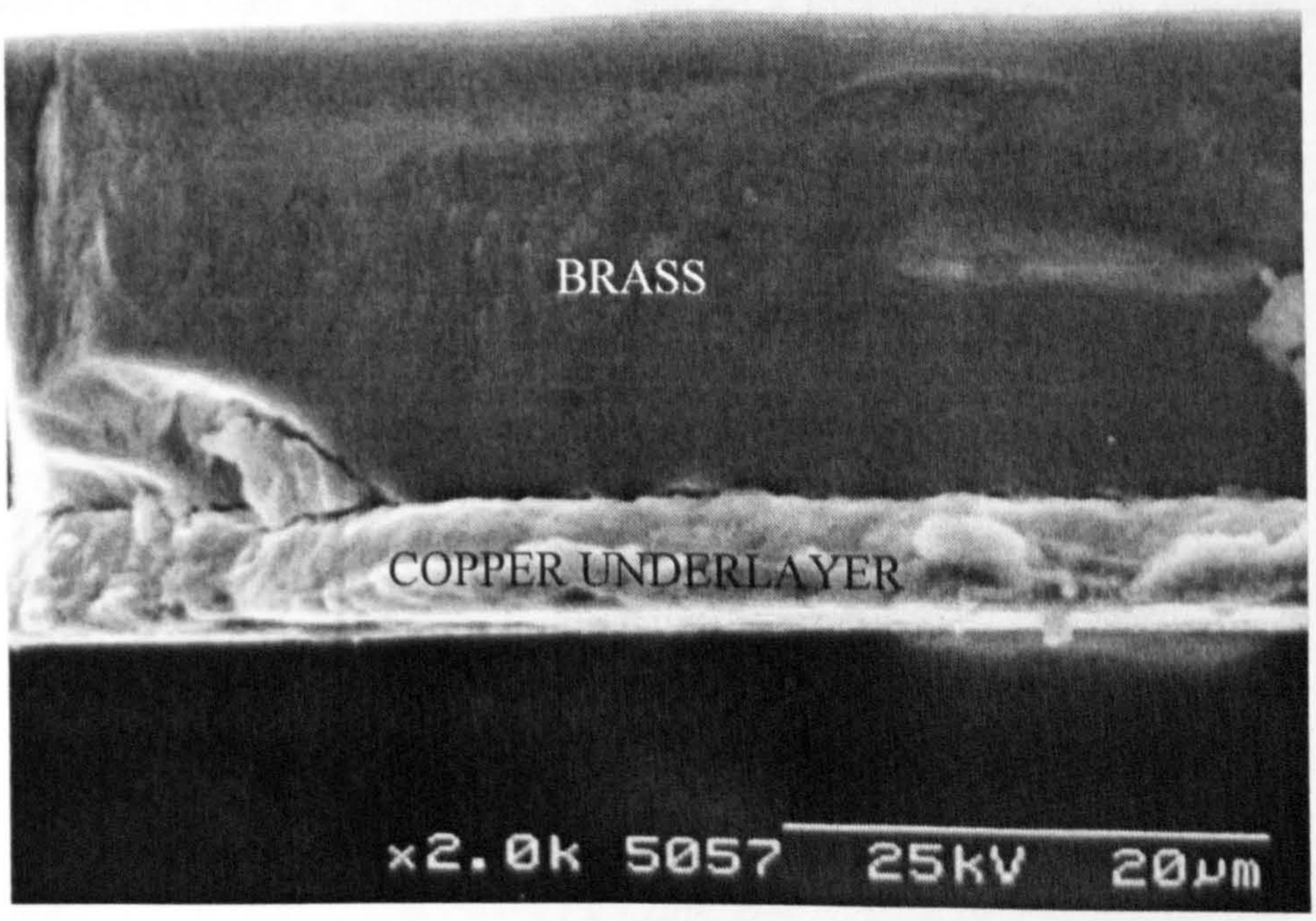

Figure 6.8 "Electroplated brass (39.09 wt % Zn)"

Cross section of a mounted brass foil, as plated on a RCE (1000rpm).

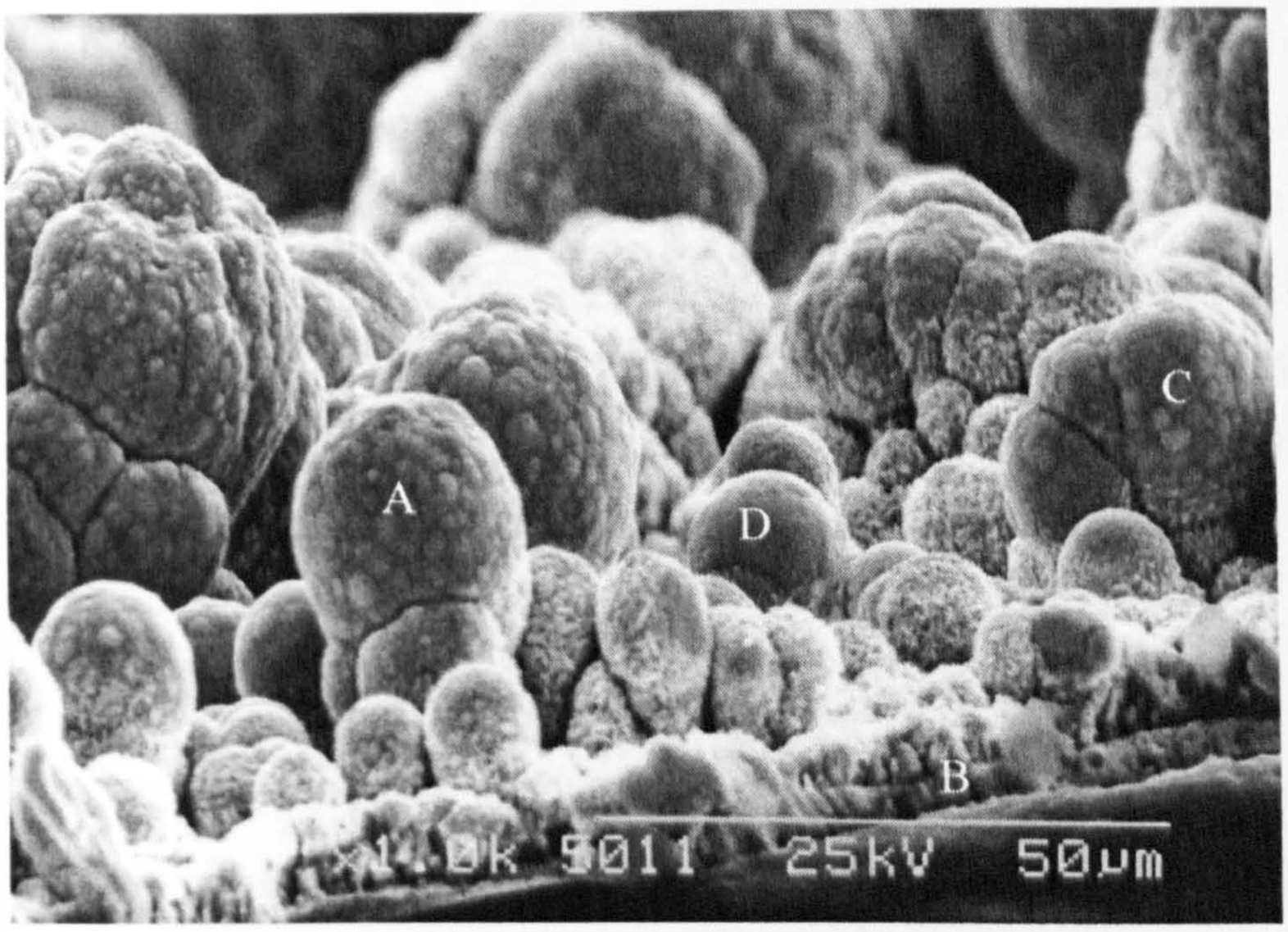

Figure 6.9 "Surface profile of electrodeposited brass with the absence of KNO_3 from the plating bath"

Cross section of a brass foil, removed as plated on a RCE (1000rpm), by cleaving in liquid nitrogen.

A 1.5µm $CuZn_5$ layer always preceded the deposition of brass at low rotation speeds (Fig 6.10).

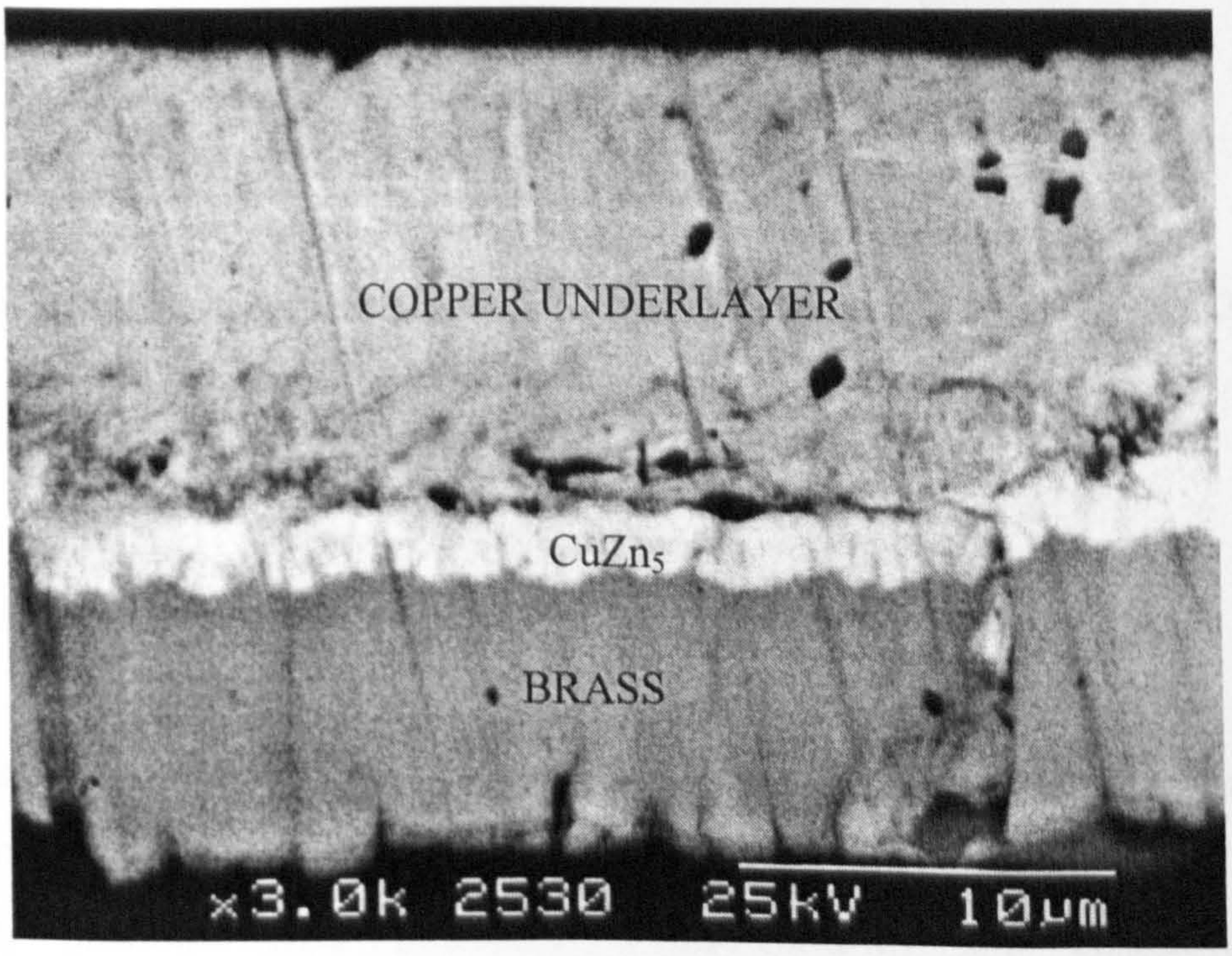

Figure 6.10 "Brass deposited at a low rotation speed"

Cross section of a mounted brass foil, as plated on a RCE (500rpm).

Scanning EDAX performed on the brass foils (Fig 6.11), showed that there was an even spread of copper and zinc with no copper or zinc rich areas or clusters. From left to right and then along the bottom, the first scan shows the secondary electron image of the foil, the second, the back scattered electron image, then copper and zinc source images. The bottom right hand side image shows traces of zinc within the copper underlayer from an overrun of zinc particles during the polishing of the foil stub for SEM analysis.

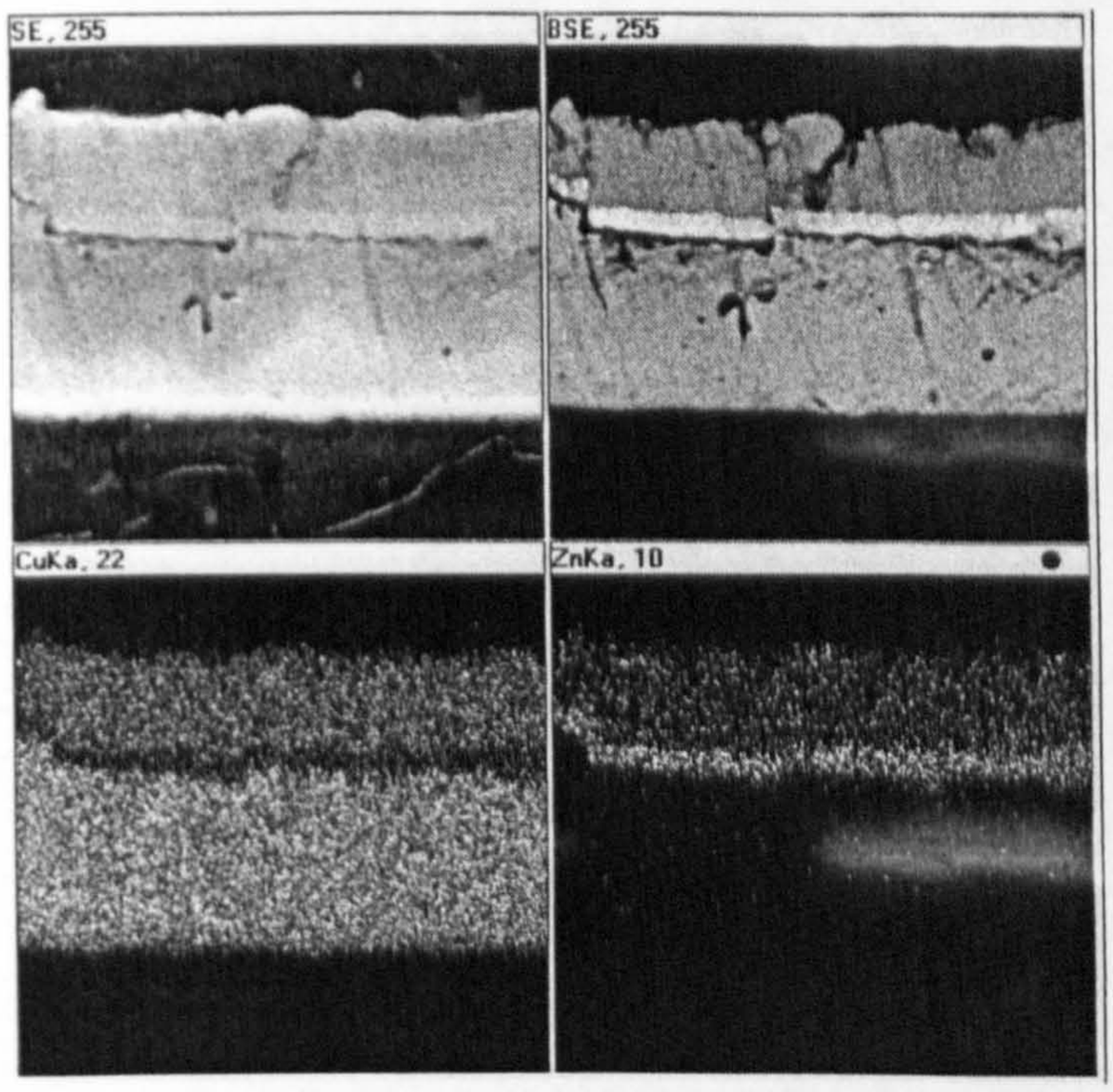

Figure 6.11 "Scanned EDAX image of a brass foil"

Image of the electrodeposited brass foil in Fig 6.10.

6.2 TRANSMISSION ELECTRON MICROSCOPY (TEM)

TEM employed upon electrodeposited samples within the martensitic transformation composition range 38.5 - 41.6 wt % zinc, all showed a universal granular type structure. Predominantly the structures were composed of a fabric of nano sized grains (Fig 6.12), extensive analysis actually showed the structures always to be made up of nano and micro grains co-existing with each other (Fig 6.13). The big grains were always of

similar size (approx. 200 - 400nm) and their distribution within the crystal matrix was very sparse. It was observed that these large structures were always martensitic in nature and never an alternative phase. The martensite grains have a substructure of twinning planes, by which transformation can occur. The smaller grains (approx. < 40nm) are a collection of α, β and martensite and phase grains (Fig 6.14).

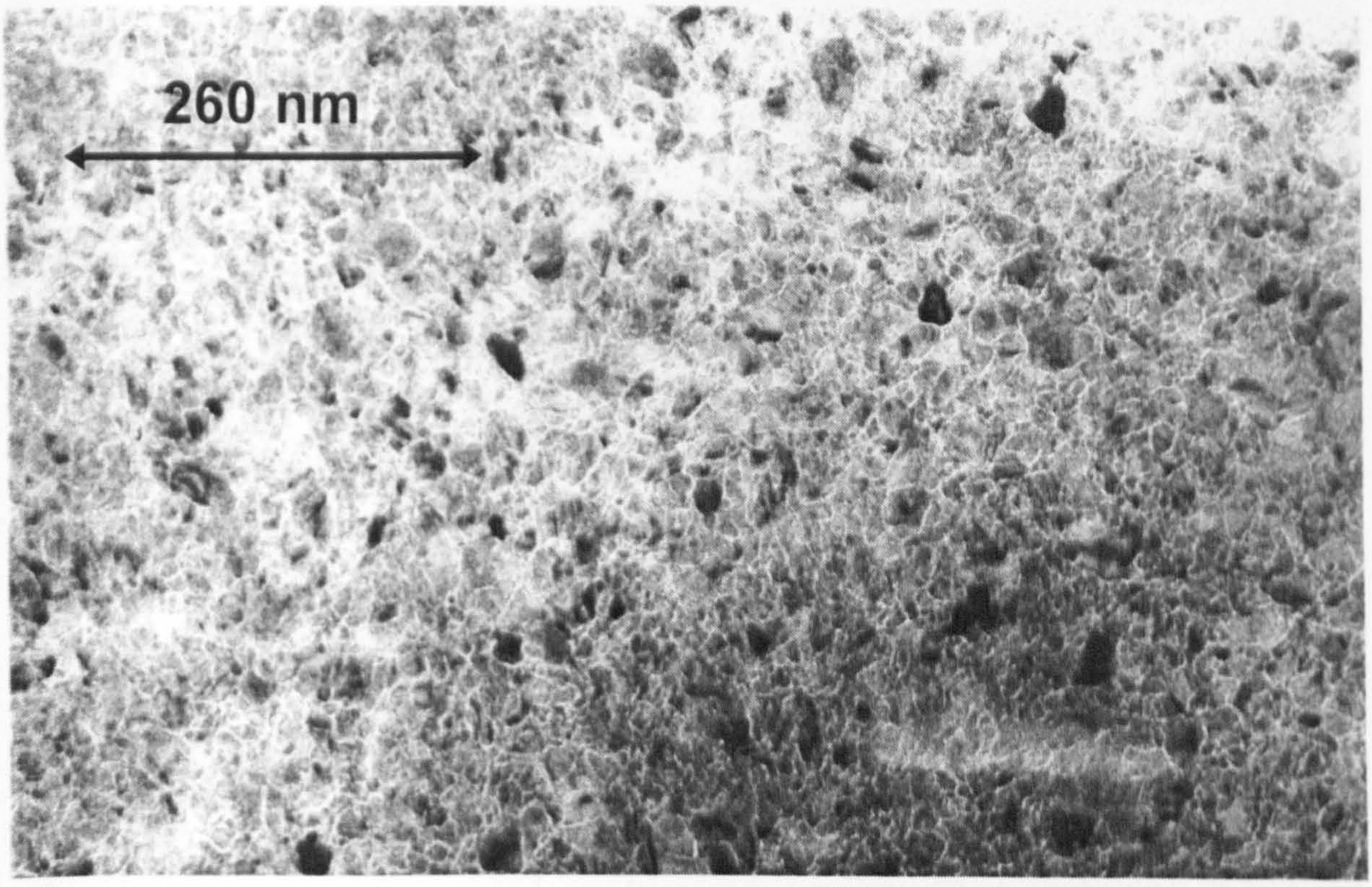

Figure 6.12 "Predominantly a sea of nano sized grains"

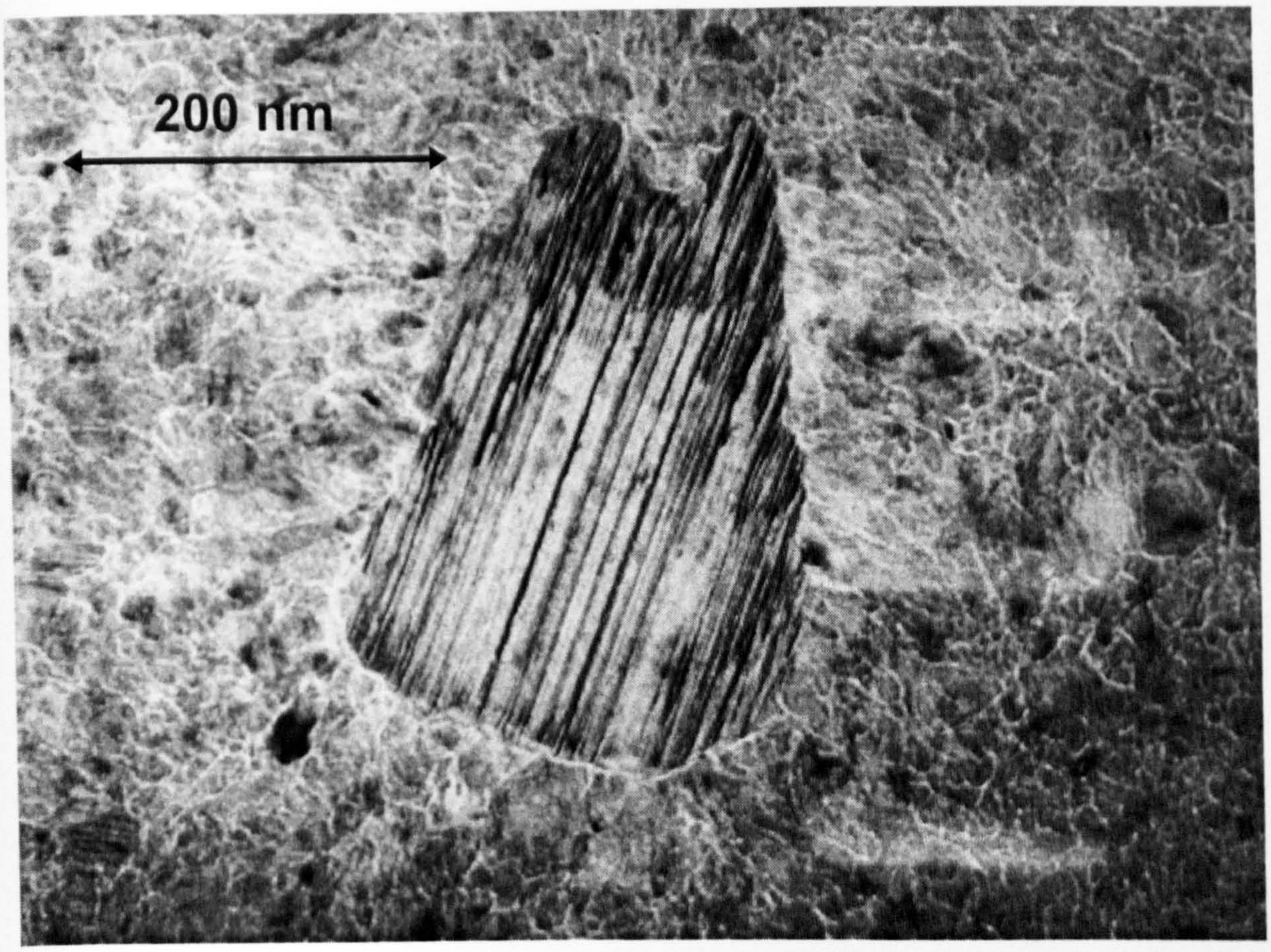

Figure 6.13 "A large island of martensite"

Martensite is recognisable by the parallel lies of the twinning planes.

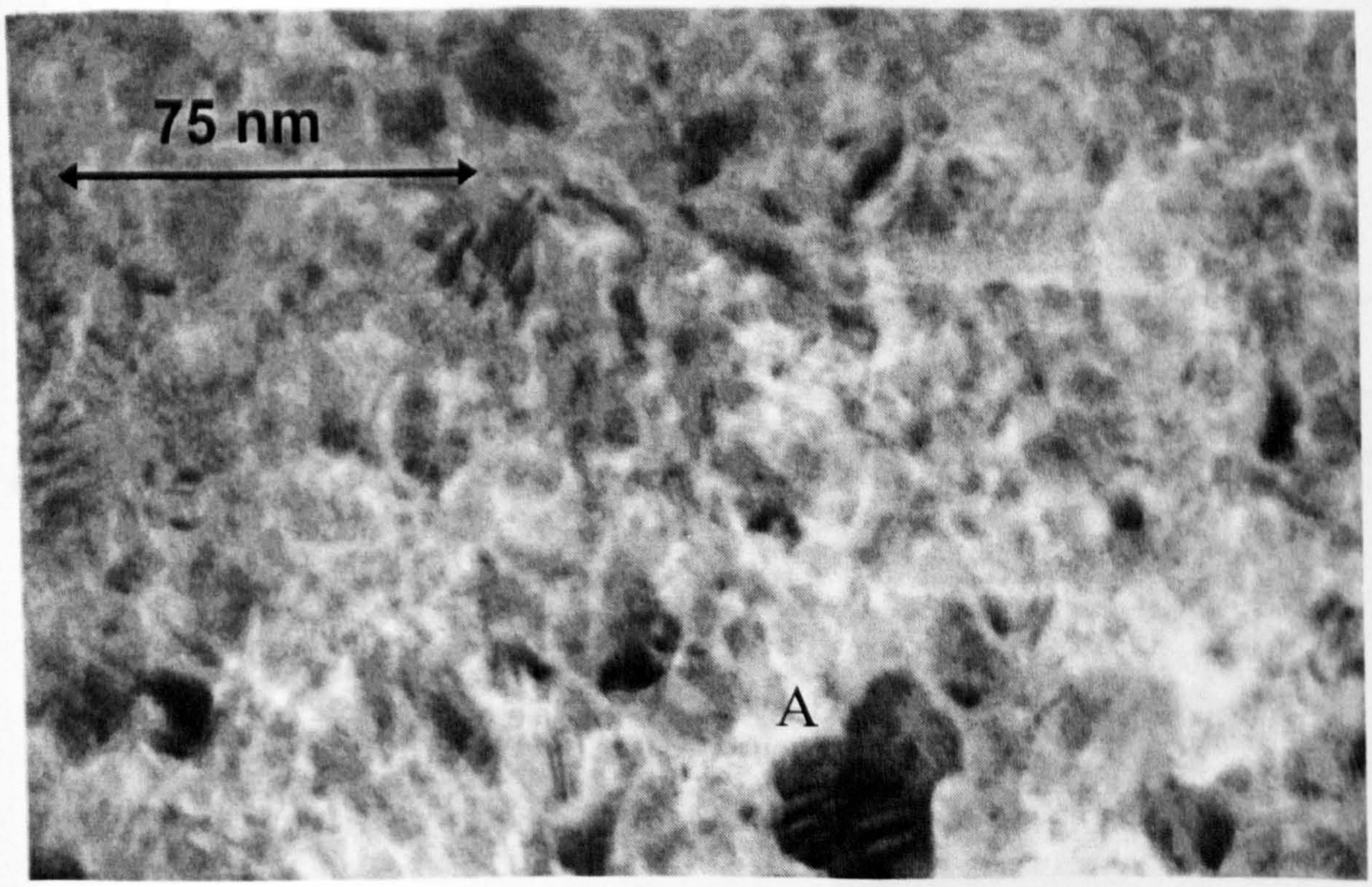

Figure 6.14 "Small grain of martensite (A)"

6.3 DIFFERENTIAL SCANNING CALORIMETRY (DSC)

A brass foil of composition 39.73 wt % zinc was subjected to four continuous thermal cycles. All four temperature profiles of the re-heating stage were identical (Fig 6.15). Each time the same amount of heat was absorbed by the foil sample, starting at -142°C, peaking at -127°C. The temperature profile of the cooling stage (Fig 6.16) does not show any heat given off (reverse reaction).

The same phenomenon was observed for a brass foil with a composition 41.19 wt % zinc. Four identical thermal cycles (Fig 6.17), each showing the same amount of heat absorption during the heating cycle, starting at -147°C, peaking at -134°C. Once again the temperature profile of the cooling stage did not show an exotherm.

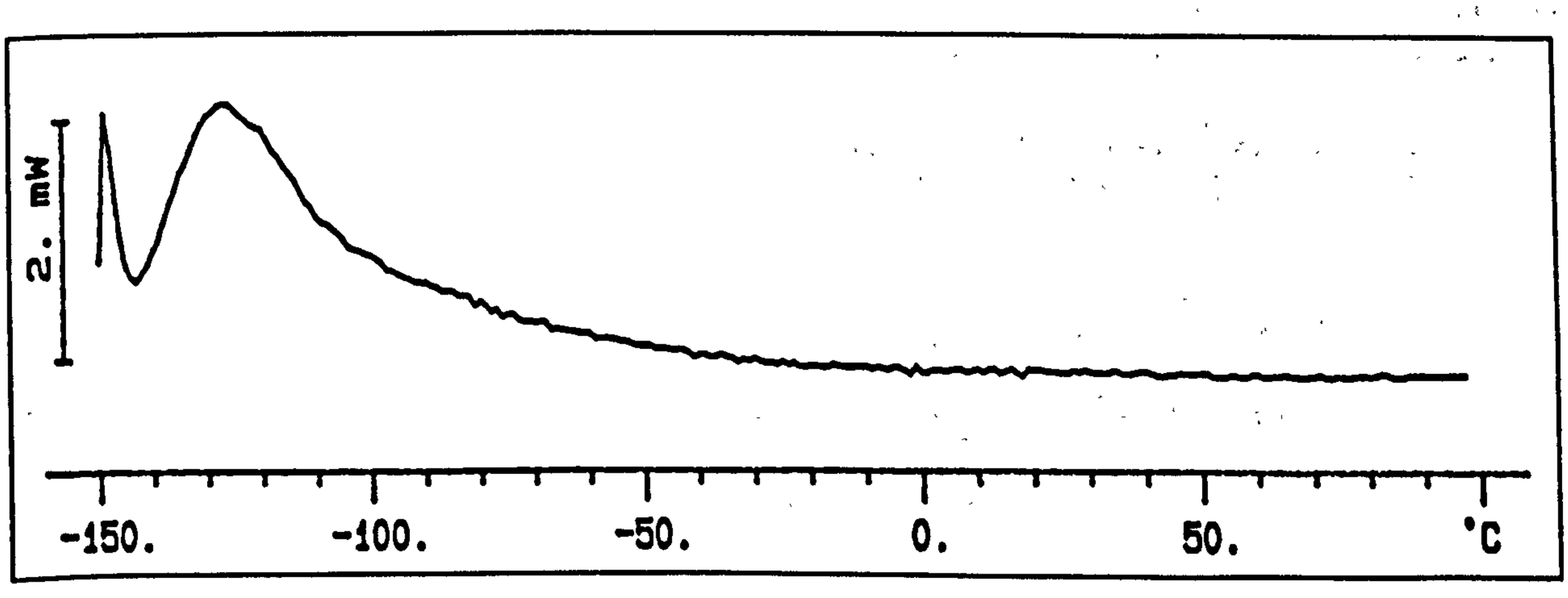

Figure 6.15 "Re-heating stage of brass foil (39.73wt % zn)"

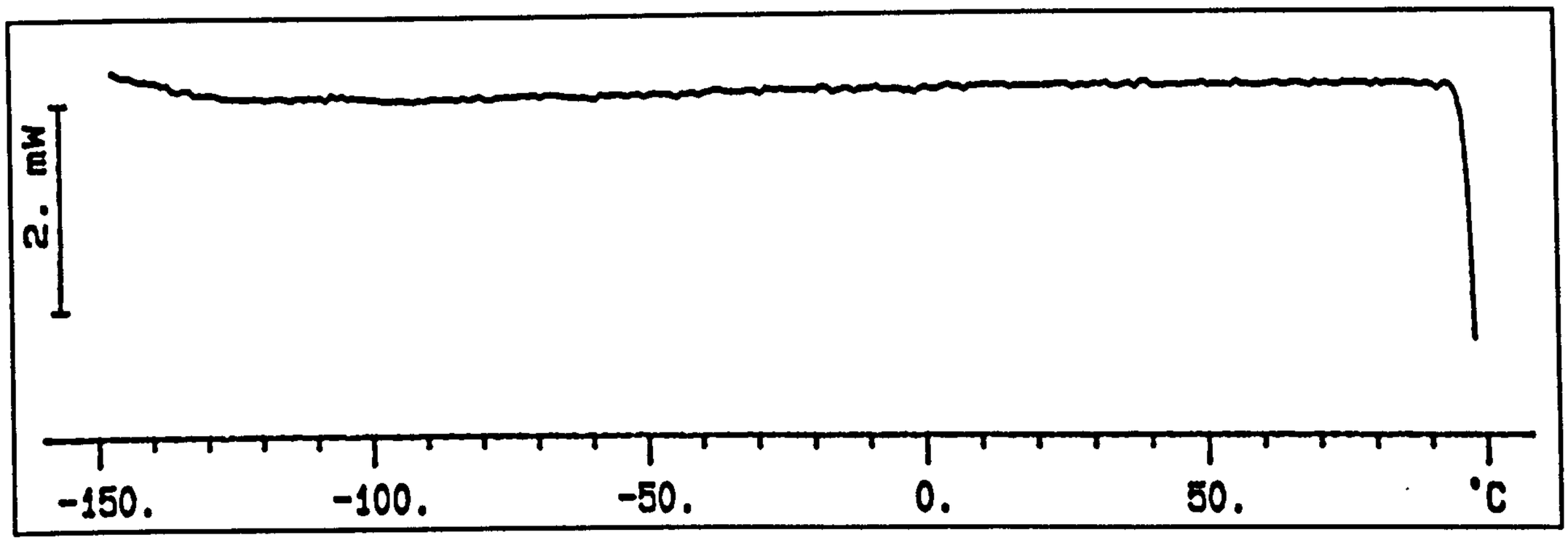

Figure 6.16 "Cooling stage of brass foil (39.73wt % zn)"

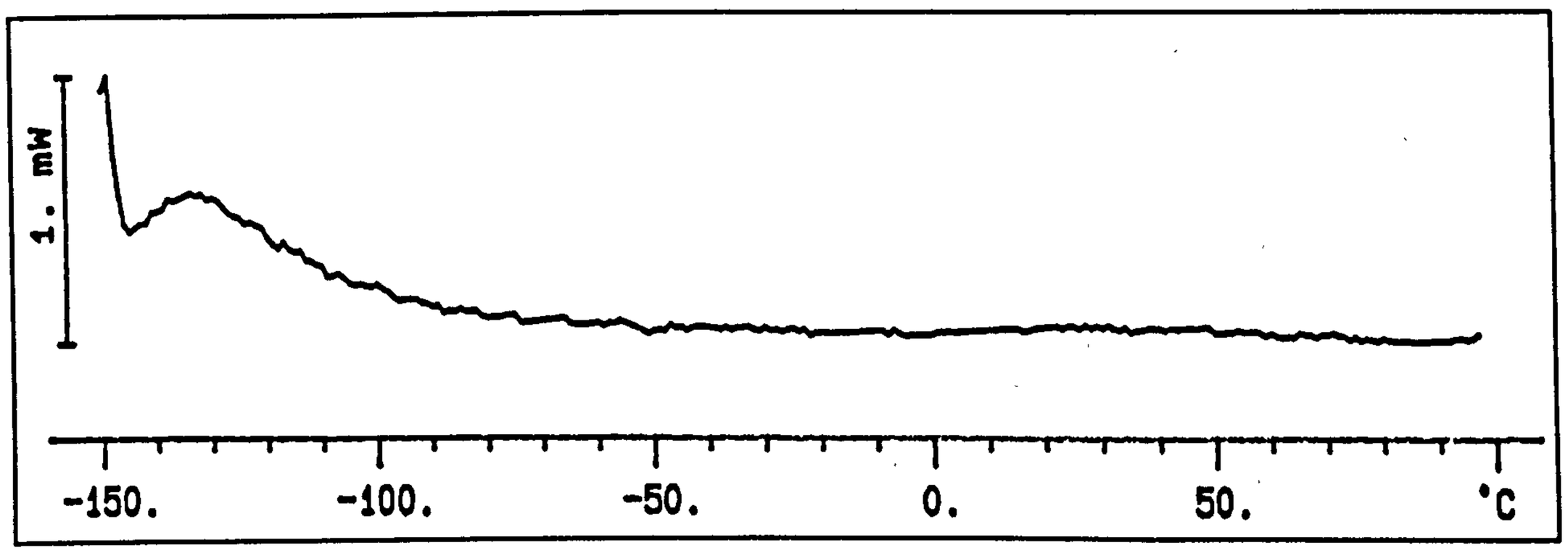

Figure 6.17 "Reheating stage of brass foil (41.19wt % zn)"

Foils heat treated in-situ at 350°C for 30 minutes, no longer showed an exchange of heat during the re-heating stage (Fig 6.18). The cooling stage still showed no thermal reaction exchange.

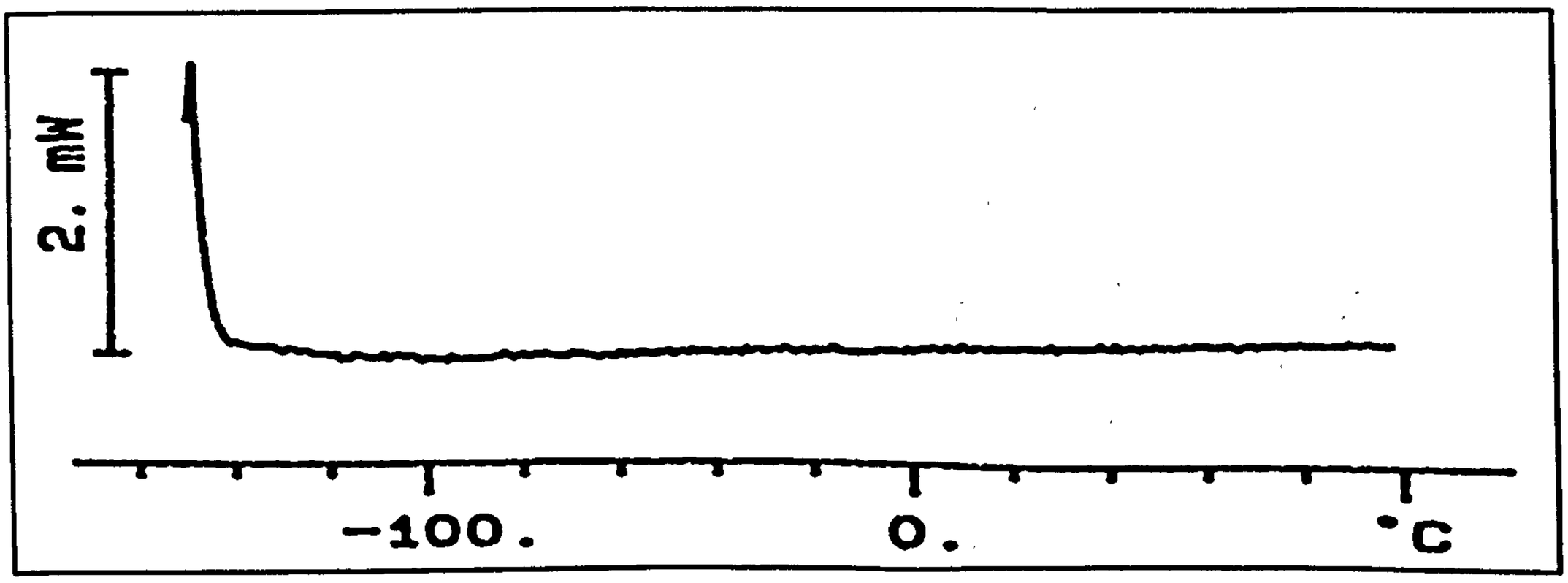

Figure 6.18 "Annealed brass foil (41.19wt % zn)"

CHAPTER 7

- DISCUSSION -

7.0 POLARISATION MEASUREMENTS

The electrode reactions of copper and zinc in the pyrophosphate electrolyte studied by RDE, gathered information about the deposition potential and characteristics of the metal from the electrolyte medium. The actual partial currents of copper and zinc could then be identified by deducing their current efficiencies as a function of potential, thereby being able to predict and accurately control the desired alloy composition to produce thin metal foils in the shape memory composition range (38.5 - 41.6 wt % zinc) for brass.

As shown in Fig 5.1, the polarisation data for copper and zinc are well defined and reproducible. Although there is a slight change in the polarisation data when the rotation speed is changed (Fig 5.8), no strong mass transfer limitations are observed in either case, initially indicating copper and zinc deposition to be kinetically controlled. A comparison of charge consumed during the anodic and cathodic part of the potential sweep for copper and zinc discharge to determine current efficiency showed that a significant portion of the current consumed during cathodic polarisation of copper and zinc was feeding other reactions. At such overpotentials the implication was that hydrogen evolution was consuming a significant proportion of the current, effectively masking the true partial currents of copper and zinc reduction.

Determination of the true partial currents for copper and zinc reduction by subtraction of the hydrogen evolution currents (Fig 5.3) from the polarisation scans found that the reduction current in the absence of copper and zinc ions to be higher, possibly because the metal ion complexes inhibit hydrogen evolution by adsorbing more strongly on the electrode surface than pyrophosphate ions. Therefore partial currents for copper and zinc could not be calculated from RDE polarisation data.

7.1 CURRENT EFFICIENCY

The deduction of the true partial currents for copper and zinc deposition by RDE cyclic voltammetry failed, as current efficiency values determined by the integral analysis of the RDE polarisation data was invalid because the dissolution of electrodeposited metals was not 100%. A visual inspection of the electrode showed a proportion of the metallic deposit still remaining on the electrode surface at the end of voltammetry experiments. This phenomenon was repeated with RCE experiments, a visual inspection showed that passive translucent oxides prevented the absolute dissolution of plated metals.

The mechanism for dissolution of copper and zinc in alkaline pyrophosphate is quite complex. Several stable metal (M) hydroxide intermediates such as MOH^{1+}, $M(OH)_2$ and pyrophosphate complexes such as $M(P_2O_7{\cdot}OH)^{4-}$, $M(P_2O_7)_2^{7-}$, $M(P_2O_7{\cdot}OH)^{3-}$ and $M(P_2O_7)_2^{6-}$ can form [1]. It is proposed these intermediates hydrolyzed to oxides, resulting in passivation, so much so that further removal of the electrodeposits had to be undertaken by dissolving the deposits in acid. The only accurate way to measure current efficiency was found to be by gravimetric means employing the RCE. Current efficiency values for brass deposition are low, below 25% as the deposition reaction competes fiercely with the hydrogen evolution reaction.

Omitting nitrate from the plating solution dramatically increased current efficiency but sacrificed deposit uniformity (Fig 6.9), as deposits experienced severe phase separation. Cyclic voltammetry performed on the electrolyte with the omission of nitrate shows an erratic response to current density as the voltage is swept along (Fig 5.5). Furthermore, current density values are much higher when nitrate is present [2]. It has been shown that nitrate does serve the role of maintaining a constant level of reducible species [3, 4] other than the reduction of copper and zinc from pyrophosphate complexes at the electrode surface, eliminating the drift of current density at set potentials.

However, the reduction of nitrate to nitrite and then to ammonia was shown by UV-VIS spectroanalysis to contribute to almost 20% of the total current passed during the deposition of a 38.73 wt % zinc brass foil. The remaining 80% is attributed to metal deposition and hydrogen evolution. Therefore, to produce an effective homogenous fine grained deposit of brass (Fig 6.8) from a pyrophosphate electrolyte, addition of nitrate is essential. This evidence dispels all contradictory claims that smooth grained deposits have been achieved with current efficiencies for deposition of 100% without the addition of nitrate or a qualified substitute. Indeed, all the current efficiency results reported in this thesis, bring into question a few interpretations regarding copper deposition and dissolution reported previously.

Although the deposition of brass foils were performed at room temperature, initial plating trials conducted at temperatures between 40 - 60°C, decisively showed this increase in temperature had no effect on current efficiency. In this regard, our results corroborate the current efficiencies found by other researchers [5,6,7,8].

7.2 PARTIAL CURRENTS

Brass deposits were only plated in the deposition potential range -1.31 to -1.66 V (7.54 to 55.16 wt % zinc) as shown in Fig 5.7, however further deposition studies revealed that copper deposits were produced from the same electrolyte with a deposition potential as low as -0.5 V, which is much higher than that observed for copper deposition from a copper pyrophosphate electrolyte. Zinc reduction from the brass electrolyte, commences at a negative potentials above -1.3 V, lower than that observed during electrodeposition from the zinc plating electrolyte. This comparison shows there is an important difference between the deposition characteristics of the individual metals copper and zinc, and their alloy, whereby there is especially a large positive shift in the reversible potential for copper during brass deposition from a pyrophosphate electrolyte. Konno and Nagayama [9] and

Despic et al. [10] have reported such a shift during copper deposition from pyrophosphate. Konno and Nagayama [9] suggested the shift is due to the fact that pyrophosphate cannot adsorb on the surface when copper concentration in the solution is high, and Despic and co-workers [10] surmised that it may be because zinc complexes with pyrophosphate which lowers the pyrophosphate concentration in solution. Our results show that pyrophosphate adsorption as well as hydrogen evolution are inhibited when Cu(II) and Zn(II) are present in the electrolyte, thereby enabling brass deposition.

The partial currents of copper and zinc (Fig 5.6 & 5.7) are much lower for brass deposition at the same deposition potentials when compared to a copper (or zinc) only electrolyte. The respective limiting current plateau's that are evident are also of a lower order. This can be accounted for by the fact that polarisation curves shift to lower current densities when the concentration of free $P_2O_7^{4-}$ increases. The relationship between current density and electrode potential is expressed as (1,2)

$$i = 2Fk_A\left[Cu(P_2O_7)_2^{6-}\right]\exp\left(\frac{-\alpha zFE}{RT}\right) \quad (1)$$

$$i = 2Fk_A K_1\left[Cu(P_2O_7)_2^{7-}\right]\left[P_2O_7^{4-}\right]^{-1}\exp\left(\frac{-\alpha zFE}{RT}\right) \quad (2)$$

Essentially when copper and zinc are present together in the brass electrolyte, to maintain a pyrophosphate ($P_2O_7^{4-}$) / metal ion (M^{2+}) ratio of 7.5:1, the overall $P_2O_7^{4-}$ concentration has increased from the equivalent copper (or zinc) only electrolyte (See Appendix A). This change in concentration is more pronounced for copper than zinc, as zinc is 9 to 1 more times concentrated in its own electrolyte. This suggests that current density is inversely proportional to $[P_2O_7^{4-}]$. Principally because of the adsorption of P_2O_7 on the electrode surface.

The partial currents for copper, zinc and brass deposition appear to approach a limiting current condition, they suggest themselves to be kinetic limiting

currents, possibly due to the slow electrochemical step for the reduction of copper and zinc. Ogden and Tench and several others [1,2,11] concluded the that the reduction of $Cu(P_2O_7)_2^{6-}$ is a step wise reduction process (3,4)

$$Cu(P_2O_7)_2^{6-} + e^- = Cu(P_2O_7)_2^{7-} \quad (3)$$

$$Cu(P_2O_7)_2^{7-}\ e^- = Cu + 2P_2O_7^{4-} \quad (4)$$

The rate-determining step being the reduction of Cu^{2+} species to, give an Cu^{1+} adion intermediate. At low copper concentrations (< 0.2M), the reduction of Cu^{2+} is relatively slow. Consequently the concentration of the adion next to the electrode surface remains low. Deposition of Cu from Cu^{1+} under this condition is orderly, giving rise to a sharp stripping peak as seen in Fig 5.1. The mechanism for zinc deposition from dipyrophosphate complexes which also involves a slow electrochemical step analogous to copper has also been documented [12]. This explanation of kinetic limiting currents gains further support from the variation in RCE rotation speed (Fig 5.8), which produced little change implying that copper and zinc deposition are kinetically controlled. Fig 5.9 shows that there is no further increase in current density when the rotation speed of the cathode is increased from 1000 to 1500rpm at a fixed plating potential. A separate, more detailed study of the kinetics of copper and zinc reduction is required to fully understand this complex process.

7.3 $CuZn_5$

The phenomenon of a $CuZn_5$ layer preceding brass deposition at low rotation speeds (500rpm), is most likely due to the formation of a stratified layer interphase as proposed by Cachet et al. [13]. It is clear that agitation speed has little effect on the final alloy composition of deposited brass (Fig 5.8), however the study of pH immediately at the rotating electrode surface (Fig 5.10 & 5.11) shows that when a low rotation speed and a high current density are imposed to produce a brass deposit, the pH at the electrode surface is

between the order of 11 - 12. The pyrophosphate speciation model for copper and zinc (Fig 5.12 & 5.13) shows that within this pH range, copper and zinc are only present as hydroxides, therefore, primarily $Cu(OH)_2$ and $Zn(OH)_2$ will surround the electrode surface.

The study performed into the fluctuation of current density during the first few minutes of brass deposition (Fig 5.9), shows an initial 4-5 minute period where the current density is exceptionally high before a quick descendency to a much lower steady-state current for the rest of the duration of the deposition. The concentration of zinc in the electrolyte to copper is 9:1, the richest zinc-copper alloy in existence is $CuZn_5$. It is hypothesized, that during this 4-5 minute period, a $CuZn_5$ layer begins to deposit on the cathode surface, above this depositing layer as suggested by Cachet et al. [13], there is a porous sub-layer of oxidation products. There will become a point as this sub-layer grows that the pH between its boundary with the electrolyte falls until cooper and zinc pyrophosphate complexes again become the dominant species and brass begins to deposit. This interpretation is speculative and the theory needs further study for clarification, but the interpretations are consistent with the data presented. $CuZn_5$ was identified from its X-ray diffraction pattern shown in Fig 6.6, SEM analysis shows the composition of this metallic intermediate as measured by EDAX, to have a perfect atomic composition ratio of Zn:Cu at 5:1.

When the rotation speed of the cathode is increased to 1000rpm for brass deposition, the pH at the electrode surface never approaches 11 (Fig 5.10), pyrophosphate complexes are still prominent and there is little pH change with increasing current density. Hence a $CuZn_5$ layer was never seen at 1000+ rpm speeds.

7.4 X-RAY DIFFRACTION

Electrodeposited brass foils characterised by employing X-ray diffraction, proved the copper-zinc equilibrium phase diagram to be fully applicable to all the electroplated brass samples produced (Fig 6.7). This led to the assumption that the martensitic phase transformation would occur within the same narrow composition range as for metallurgically prepared brass alloys.

The characterisation of the phase spectra was unfortunately hindered by several factors, firstly the sample holder for the Phillips X-ray diffractometer was constructed of mild steel and accounts for regularly seen peaks on most of the diffraction patterns recorded, the most notable peak occurs at a reflection angle of 44.2-44.3 (2θ). The full diffraction pattern for the sample holder was recorded and is tabulated in Appendix B. Secondly, there was an interference pattern apparent from the underlying copper on some brass foils. The copper could not be fully etched off the back of the foils because as soon as there was a tiny pin-hole contact through to the brass, a bimetallic corrosion cell would set up between copper and brass. Copper being the more noble metal of the two, its dissolution would halt and nitric acid would selectively begin to strip away the brass. Thirdly, the foils having been plated on a cylinder, peeled off and straightened for their measurement by x-ray diffraction, were presented for analysis under stress, ultimately resulting in the distortion of reflection patterns from straight line signals to broader more rounded peaks. Furthermore, the occurrence of stacking faults and dislocations would have added to this effect. To alleviate this perceived problem, the foils were heat-treated whilst straightened between two pieces of quartz glass, first to a temperature of 100 °C to 'relax' the brass, but with no recognizable difference to the diffraction patterns. Further high temperature heat treatments including quenching treatments to increase the β-phase within the deposits, only succeeded in oxidisng the metal foils either by inadequate total evacuation of oxygen in the argon furnace or by the incorporation of minute traces of oxygen already in the electrodeposit. Lastly,

the Phillips X-ray diffractometer employed was a very old machine, the signal is not filtered and the nature of the output is by a running graph plotter machine aided by felt pens, it is therefore believed that discrepancies of ± 0.3 of 2θ values possibly manifest.

Interestingly, the order of the intensities from the reflections did not always correlate to the literature reference tables [14] and some expected reflections were noticeably absent. The height of the peaks vary with texture and the best way to get rid of texture was to employ powder X-ray diffraction, allowing all the reflections to be seen. Due to the nature of the sample being a metallic foil however, a powdered foil gave broad intensities, to vast for the computer scanner to accurately quantify, so this method of analysis was abandoned.

α-phase brasses: The 15.89% zinc brass deposit (Fig 6.1) was plated with a low rotation speed of 500rpm, so there is a large influence of $CuZn_5$ here. There are two peaks from the sample holder evident too.

An increase in zinc to 22.12 wt % (Fig 6.2), still sees just α-phase present, however the α-phase peaks this time are split, they are in fact the product of two peaks, one is attributed to the α-phase, the other from what remains of the copper underlayer. The α-phase possesses a *Fm3m*, cubic lattice structure like that of pure copper. The lattice constant 'a' for pure copper is 3.6150 Å; starting from pure copper and replacing copper with zinc to produce α-phase brass, the lattice constant increases only very slightly at first, hence the X-ray spectra for copper and low zinc content brasses will almost be identical [8]. Consequently, for a 22.12 wt % zinc α-phase brass, the lattice constant 'a' has increased to 3.6367 Å, to incorporate the bigger zinc atom. The cubic structure has become larger and this is reflected in an increase in the d-spacings and consequently a decrease in 2θ values.

α & β phase brasses: The X-ray spectra for 38.75 wt % zinc brass (Fig 6.3), shows the emergence of β-phase co-existing with α-phase, now the α-phase

has become saturated with zinc. The strongest reflections (2θ = 43.0, 50.2), are for the α-phase and weaker ones for β-phase as expected, as there is little β-phase present. The reflections for β-phase brass are consistent with their literature values [9], but here they appear moderately convoluted (2θ = 39.5 - 40.1, 71.3 - 72.9), this is due to the presence of martensite (110, 020 planes respectively) within the β-phase, again in good agreement with the literature values (Appendix B). The β-phase is a body centred orthorhombic structure whose lattice constant does not change with a change in alloy composition [8], so unlike the α-phase, changes to composition will not change the angles of reflections. Further evidence of the existence of martensite is therefore compounded when considering the X-ray spectra of the 44.53 wt % zinc brass (Fig 6.4), which shows the convoluted β-phase peaks to have extended with sharper intensity peaks (2θ = 39.4, 70.7) at the lower end of these reflections. These lower end reflections can therefore only be due to martensite. These reflections show the d-spacings of the martensite planes to have increased with the relative increase of zinc to the alloy mposition.

& β phase brass: The reflections from a 55.16 wt % zinc brass (Fig 6.5), e now attributed to the emergence of a γ-phase as well as the β-phase, as edicted by the copper-zinc equilibrium phase diagram. There are some eak copper reflections evident from what remains of the copper underlayer.

$_1CuZn_5$: The phase spectra shown in Fig 6.6 represents the deposition of ass when employing a RCE with a low rotation speed (500rpm). The plating periment was terminated after 5 minutes. The spectra confirms that in this ne period, $CuZn_5$ was produced. There are also strong reflections from the derlayer of copper which was etched to a degree, but its complete removal as impossible with such a thin deposit of $CuZn_5$.

7.5 SEM, EDAX & TEM

TEM showed the electrodeposited brass foils to be composed of a matrix of α, β and martensite nano sized grains (< 40nm) co-existing with a sparse distribution of larger grains (200-400nm). EDAX performed on the large as well as the smaller grains, showed there to be no compositional differences within the grains. The content of oxygen, phosphorus and nitrogen within the brass foils were all within the background signal in an EDAX analysis. The larger grains were always martensite in nature, recognisable by their twinning planes. In-situ x-ray diffraction performed on these large grains by the EPFL, Federal Institute of Lausanne, identified and confirmed these larger grains to be martensite M9R, but their work cannot be displayed here. In a separate experiment, the microstructure of these larger grains was recorded on video, as the brass foil sample was heated up to 200°C and then cooled back to room temperature. The re-crystallisation of the alloy commenced at 180°C, martensite disappeared at this temperature and did not reappear when the foil was cooled down to room temperature. This indicates that the formation of the martensite was generated perhaps from the stresses originally generated during electrodeposition.

7.6 DSC

The two brass foils, 39.73 and 41.19 wt % zinc, are both within the martensitic transformation composition range (38.5 - 41.6 wt % zinc). X-ray diffraction and TEM analysis has shown that both have martensite within their β-phases. When subjected to four continuous thermal cycles, each time during the re-heating stage, the same amount of heat was absorbed at precisely the same point. This repetitive undiminishing reaction, shows that there must exist an equal and opposite endothermic reaction. The Cu-Zn martensite transformation is known to be a first order transformation, liberating heat when martensite is formed, hysteresis is also associated with the

transformation. The reversion to austenite starts (A_s) at -142 °C and -147 °C respectively for the two brass foil compositions, therefore hysteresis dictates the transformation to martensite would start at temperatures (M_s) below these. The limitation of the DSC equipment available would only allow examination down to temperatures of -150 °C, and therefore it is surmised that the M_s temperature is hidden from us, and must occur below -150 °C depending on the hysteresis temperature range.

REFERENCES

1. C.A Ogden and D.M.Tench, Plating Surf. Finish, 1983, Vol 7, p.70.
2. T.M.Tam and R.Taylor, J.Electrochemical Society, Vol 133, No 6, 1986, p.1101
3. F.A.Lowenheim, Modern Electroplating, Technical Reference Publications Ltd., Arrowsmith, Bristol, UK, 1955.
4. F.Passel, Plating, Vol 46, 1959, p 628
5. M.Ishikawa, H.Emonoto, New Materials. New Process., 1983, Vol 2, p.243
6. M.Ishikawa, H.Emonoto, M.Matsuoka, C.Iwakura, Electrochim. Acta., 1995, Vol 40, p.1663
7. A.C.Hamilton, Plating Surface Finishing, 1995, Vol 81, p.48
8. M.Ishikawa, H.Emonoto, M.Matsuoka, C.Iwakura, Electrochim. Acta., 1994, Vol 39, p.2153
9. H.Konno and M.Nagayama, Electrochim.Acta., 1978, Vol 23, p.1001
10. A.Despic, V.Marinovic, V.D.Jovic, J.Electroanal. Chem., 1992, Vol 339, p.473
11. H.Konno and M.Nagayama, Electrochim.Acta., 1977, Vol 22, p.353
12. C.Furlani and A.Furlani, Ricerca Scientifica, 1962, Vol II A2, p.411
13. C.Cachet, B.Saidani and R.Wiart, Electrochim.Acta., 1988, Vol 33, p.405
14. X-ray diffraction tables for expected reflections from inorganic compounds (Cornell University Press,1991).

CHAPTER 8

- CONCLUSIONS -

8.0 CONCLUSIONS

- Cu-Zn thin films (5 - 30μm) were electrodeposited from a pyrophosphate bath, which were smooth, uniform and homogeneous. They were plated on a RCE employing a rotation speed of 1000 rpm and a current density of upto 39.78 mA/cm^2 to produce 0 - 53 wt % zinc, brass foils.

- The addition of nitrate or a suitable substitute is vital for homogenous, uniform deposits. Omission of nitrate from the plating electrolyte leads to severe phase separation, resulting in very rough, powdery textured deposits.

- There is a shift in the reversible potentials for copper and zinc, during brass deposition from a pyrophosphate electrolyte. Copper and zinc reduction from a brass electrolyte, commence at -0.5 V and -1.3 V respectively. The reversible potential of copper from a copper pyrophosphate electrolyte was -0.8 V, the equivalent for zinc was -1.1 V.

- The partial currents of copper and zinc are much lower for brass deposition at the same deposition potentials when compared to a copper or zinc only pyrophosphate electrolyte. This is accounted for by the fact that polarisation curves shift to lower current densities when the concentration of free $P_2O_7^{4-}$ increases.

- There is evidence to suggest that the deposition of copper and zinc from a pyrophosphate electrolyte are kinetically controlled in low concentrations (< 0.2M). This is supported by the slow electrochemical steps at low concentrations and by hardly any change in the polarisation data when the rotation speed of the RCE is changed.

- Current efficiency values for brass deposition are low, below 25%. The current efficiency values for copper and zinc deposition from a pyrophosphate electrolyte are below 45% and 15% respectively. A dramatic increase in current efficiency is observed when nitrate is omitted from the plating bath.

- A 1.5μm $CuZn_5$ layer precedes brass deposition at low rotation speeds (500rpm). This is most likely due to the high pH at the surface of the RCE, too high to maintain copper and zinc pyrophosphate complexes. It is hypothesized that $CuZn_5$ only deposits during the first 4-5 minute period of deposition.

- The phase spectra of all electrodeposited brass foils produced with 0 - 60 wt % zinc, determined by x-ray diffraction, were in agreement with the phase equilibrium diagram for Cu-Zn.

- Martensite phase was found in the β-phase of brass compositions 38.75 - 44.53 wt % zinc. TEM showed the brass foil deposits to contain nano sized (>40nm) and larger sized (200-300nm) martensite grains. The microstructure of the martensite grains were recognisable by their twinning planes.

- DSC analysis, the most direct method of characterising transformation, has shown the two brass foils, 39.73 and 41.19 wt % zinc, to exhibit evidence of a martensitic transformation.

APPENDIX A

Table A1

"Copper-Zinc Pyrophosphate Electrolyte used for the deposition of all brass foils"

Bath Constituent	*Concentration*
$Cu_2P_2O_7$	0.01M
$Zn_2P_2O_7$	0.09M
$K_4P_2O_7$	0.23M
KNO_3	0.12M
$H_4P_2O_7$ pH 8.4	0.028M

Table A2

"Copper Pyrophosphate Electrolyte"

Bath Constituent	*Concentration*
$Cu_2P_2O_7$	0.01M
$K_4P_2O_7$	0.0224 M
KNO_3	0.12M
$H_4P_2O_7$	Adjusted to pH 8.4

Table A3

"Zinc Pyrophosphate Electrolyte"

Bath Constituent	***Concentration***
$Zn_2P_2O_7$	0.09M
$K_4P_2O_7$	0.209M
KNO_3	0.12M
$H_4P_2O_7$	Adjusted to pH 8.4

Table A4

"Pyrophosphate Electrolyte with no metal ions"

Bath Constituent	***Concentration***
$K_4P_2O_7$	0.23M
KNO_3	0.12M
$H_4P_2O_7$	Adjusted to pH 8.4

APPENDIX B

In addition to the reflections from the various brass phases there are reflections notably from the mild steel X-ray diffraction sample holder and from the copper underlayer which could never be totally etched away. X-ray diffraction was employed on the sample holder alone and then on a foil of the copper plated underlayer, their spectra was analysed and tabulated as shown in Tables B1 and B2.

Table B1

"Electroplated copper underlayer"

Strength	***Reflection (2θ)***	***d - spacing (A)***	***Orientation***	***Phase***
Very Strong	43.3	2.088	111	Cu
Strong	50.5	1.808	200	Cu
Medium	74.2	1.278	220	Cu
Medium	90.0	1.090	311	Cu
Weak	95.2	1.044	222	Cu

Table B2

"Mild Steel XRD Sample Holder"

Strength	***Reflection (2θ)***	***d - spacing (A)***
Very Strong	44.2 - 44.3	2.049 - 2.044
Medium	83.8 - 84.0	1.154 - 1.152
Weak	64.5	1.444
Weak	100.4 - 100.9	1.003 - 0.999
Weak	117.5 - 118.4	0.902 - 0.896

α-Phase: *Fm3m*, Cubic Lattice

$a = b = c$, $\alpha = \beta = \gamma = 90°$

The value of d, the perpendicular distance between adjacent planes in the set (hkl), is calculated from...

$$\frac{1}{d^2} = \left(\frac{h^2 + k^2 + l^2}{a^2}\right)$$

β-Phase: *Im3m*, Body centred orthorhombic structure

$a \neq b \neq c$, $\alpha = \beta = \gamma = 90°$

For orthorhombic d-spacings:

$$\frac{1}{d^2} = \left(\frac{h^2}{a^2}\right) + \left(\frac{k^2}{b^2}\right) + \left(\frac{l^2}{c^2}\right)$$

γ-Phase: *I43m*, Complex double cubic lattice

Martensite-Phase: *Pm3m*, Inclined monoclinic lattice

$a \neq b \neq c$, $\alpha = \gamma = 90°$, $\beta \neq 90°$

For monoclinic d-spacings:

$$\frac{1}{d^2} = \frac{1}{\sin^2\beta}\left[\frac{h^2}{a^2} + \frac{k^2 \sin^2\beta}{b^2} + \frac{l^2}{c^2} - \frac{2hl\cos\beta}{ac}\right]$$

Table B3, shows the lattice constants of 9R martensite. From these literature values, the calculated reflections from a 38.6 wt % zinc brass are almost identical (Table B4) with those seen (Fig 6.3) from the electrodeposited brass foil of composition 38.75 wt % zinc. Precise determination was impossible,

principally due to the signals being convoluted from the reflections from the β-phase.

Table B3

"Lattice constants of 9R Martensite of Cu-Zn alloys"*

Zn (At %)	a	b	c	β_0
38.6	4.439	2.638	19.21	89°
39.3	4.412	2.678	19.19	88.5°

**The Encyclopedia of Electrochemistry of the Elements. Vol II*

Table B4

"Martensite reflections observed in the electrodeposited brass foil of composition 38.75 wt % zinc"

Reflection	Literature Value (2θ)	Observed (2θ)
111	39.8	39.5 - 40.1
020	71.5	71.3 - 72.9